Recent Progress in Materials Exploration for Thermocatalytic, Photocatalytic, and Integrated Photothermocatalytic CO2-to-Fuel Conversion

Review Article

Author(s):
Zhang, Wenjun; Ma, Ding; Pérez-Ramírez, Javier; Chen, Zupeng

REVIEW

**ADVANCED
ENERGY & SUSTAINABILITY
RESEARCH**
Open Access

www.advenergysustres.com

Recent Progress in Materials Exploration for Thermocatalytic, Photocatalytic, and Integrated Photothermocatalytic CO$_2$-to-Fuel Conversion

Wenjun Zhang, Ding Ma,* Javier Pérez-Ramírez,* and Zupeng Chen*

The excess depletion of carbon-rich fossil fuels and agroforest biomass resources has aggravated the energy crisis and environmental pollution, causing increased CO$_2$ emissions. Accordingly, the goal of "peak CO$_2$ emissions and carbon neutrality" is proposed to alleviate global warming. CO$_2$-to-fuel conversion is considered as a preferable move for reducing the atmospheric CO$_2$ concentration and further upgrading to chemical feedstocks. However, the highly efficient CO$_2$ conversion remains challenging due to the thermodynamic limits and kinetic barriers, which require high energy input through conventional thermocatalysis. Inspired by "artificial photosynthesis," photocatalytic CO$_2$ transformation has received tremendous attention and makes remarkable progress over the past decades, although it is still far from practical application. Recently, the integrated photothermocatalysis has emerged as an intelligent strategy to utilize solar energy to induce local heating and energetic hot carriers, which synergistically promote CO$_2$-to-fuel conversion. The key to the success of CO$_2$ upgradation is catalysts' development with improved activity, selectivity, and stability. This review highlights the recent advancements in materials designing for practical CO$_2$ conversion through thermocatalysis, photocatalysis, and photothermocatalysis during the past five years, emphasizing the reaction pathways and mechanism on the C═O bond activation and intermediates formation. Finally, the current challenges and future opportunities are described.

1. Introduction

Since the rapid development of the national economy, energy consumption has been continuously increasing in the past decades. The excessive dependence on nonrenewable fossil fuels has released large amounts of carbon dioxide (CO$_2$), which is a notorious greenhouse gas and has certainly caused serious global warming and ocean acidification problems. In response to the challenges of climate change, the entire world has put forward the goal of "peak CO$_2$ emissions and carbon neutral." As an important part of the Paris Agreement commitment, a roadmap for China to "double carbon" target is to reach a carbon peak emission by 2030 and be carbon neutral by 2060. Particularly, carbon emission reduction has become a critical path to realize green development and achieve the "double carbon" vision. Accordingly, minimizing atmospheric CO$_2$ concentrations to alleviate environmental pollution and climate change has become an imperative mission. The imposition of the CO$_2$ tax is an effective initiative to realize the energy conservation and emission reduction as well as the optimized energy mix, which has been carried out by an increasing number of countries according to their national conditions. In addition, CO$_2$ capturing and utilization through chemical transformation has been considered as a preferable process for highly efficient CO$_2$ mitigation rather than separation and geological sequestration processes.[1] Importantly, it provides

W. Zhang, Z. Chen
Jiangsu Co-Innovation Center of Efficient Processing and Utilization of Forest Resources, International Innovation Center for Forest Chemicals and Materials, Jiangsu Province Key Laboratory of Green Biomass-based Fuels and Chemicals, College of Chemical Engineering
Nanjing Forestry University
Nanjing 210037, China
E-mail: czp@njfu.edu.cn

The ORCID identification number(s) for the author(s) of this article can be found under https://doi.org/10.1002/aesr.202100169.

D. Ma
Beijing National Laboratory for Molecular Sciences, College of Chemistry and Molecular Engineering and College of Engineering, and BIC-ESAT
Peking University
Beijing 100871, China
E-mail: dma@pku.edu.cn

J. Pérez-Ramírez
Institute for Chemical and Bioengineering, Department of Chemistry and Applied Biosciences
ETH Zürich
Zürich 8093, Switzerland
E-mail: jpr@chem.ethz.ch

ADVANCED
SCIENCE NEWS

www.advancedsciencenews.com

ADVANCED
ENERGY & SUSTAINABILITY
RESEARCH
Open Access

www.advenergysustres.com

an economical manner to convert CO_2 into high-value-added products, which can be manufactured into chemicals and fuels on an industrial scale, thus closing the carbon loop. However, the CO_2 molecule is kinetically inert and thermodynamically stable, which requires effective catalytic techniques to decrease reaction barriers in C=O activation and C—O cleavage. Thus, the CO_2 conversion requires substantial energy inputs, including heat and sunlight, which could achieve sufficient reaction rates for highly efficient and selective CO_2 transformation through thermocatalytic and photocatalytic approaches.[2a,b] Moreover, photothermocatalysis as the combination of two energy sources in one reaction process has been regarded as an advanced approach, which further enhances the catalytic performance of CO_2-to-fuel conversion.[3] The chronology of the technologies for CO_2 conversion is presented in **Figure 1**, highlighting the milestones of the developments of catalysts, products, and techniques for their characterization.

Among these technologies, thermocatalytic transformations of CO_2 either via direct or indirect approaches have already been applied at the industrial level and have relatively higher product outputs. Four main classes of products can be obtained from CO_2 thermocatalysis, that is, carbon monoxide (CO), methanol (MeOH), methane (CH_4), and other higher hydrocarbons.[4] Cheap and clean hydrogen (H_2) from an economical and sustainable route is critical to have a positive environmental impact on the aforementioned CO_2 thermocatalytic processes. First, CO generated from reverse water—gas shift (RWGS, $CO_2 + H_2 \rightarrow CO + H_2O$) has been considered as a valuable catalytic process for CO_2 hydrogenation as CO is an important feedstock for Fischer—Tropsch (FT) and MeOH synthesis

($CO_2 + 3H_2 \rightarrow CH_3OH + H_2O$). Second, a large proportion of *CO ('*' represents "the surface adsorption site on catalyst") absorbed on the catalyst surface could suppress the competing RWGS route, thus generating a higher-value-added product— methanol. Third, the methanation of CO_2, also called the Sabatier reaction ($CO_2 + 4H_2 \rightarrow CH_4 + 2H_2O$), undergoes an eight-electron process for the formation of syngas and compressed natural gas. Finally, the direct hydrogenation of CO_2 into other hydrocarbons, including light alkanes and olefins, is similar to that of the FT process through the methanol-mediated or nonmethanol-mediated pathways.

However, CO_2 utilization through thermocatalytic processes requires high energy costs accompanied by additional CO_2 emission, as the heat was mainly obtained from the combustion of fossil fuels. By comparison, photocatalysis driven by renewable solar energy is an attractive approach and serves as an effective alternative for CO_2 transformation, which has already been at a stage of rapid development.[5] Under solar light irradiation, semiconductor photocatalysts could accelerate the C=O activation process, which could be subsequently reduced to hydrocarbons by photogenerated electrons. Unfortunately, the practical application of photocatalysis has yet reached an industrial scale due to the lack of highly effective photocatalysts, limited photocatalytic performance, suboptimal reactors, and the intermittent nature of solar light. Therefore, the integration of light and heat in CO_2 chemical transformations emerges as a promising approach to further reduce the consumption of fossil fuels and increase the conversion efficiency of atmospheric CO_2. Photothermocatalysis absorbs the visible and near-infrared light
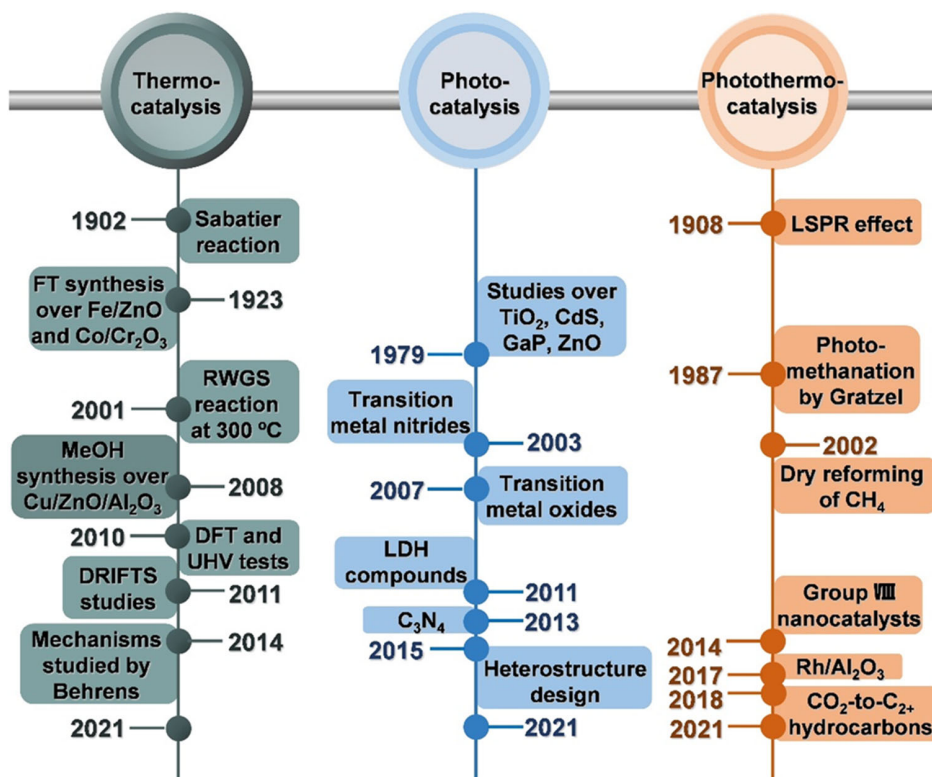

Figure 1. Chronology of the technologies for CO_2 conversion, highlighting the developments of catalysts, products, and characterization techniques.

2100169 (2 of 40)

energy, which undergoes the dissipation into heat (temperature up to 300−500 °C or even higher), thus inducing a process similar to conventional thermocatalysis.[6a,b] The photothermo effect can be ensured by the construction of efficient light-absorbing materials to capture heat from sunlight and raise the temperature of the whole reaction system. Another way is to synthesize plasmonic metals to cause surface plasmon resonance (SPR) effects, which could generate numerous hot electrons and holes. There are two categories of mechanisms and applications focused on plasmonic nanostructures: 1) photoinduced hot carriers (plasmonic photocatalysis) and 2) light-excited phonons (photothermal catalysis).[7] Accordingly, the plasmonic photothermocatalytic behavior provides a preferable understanding of electron-driven and temperature-driven catalysis over plasmonic materials, which is conducive to bridge the gap between the application of thermocatalysis and photocatalysis. Thereby, RWGS, methanation, methanol, and other hydrocarbons synthesis routes can be realized in a highly active and selective manner. Meanwhile, Ozin et al. proposed universal equations, which could describe net CO_2 emissions induced from (photo)thermocatalysis RWGS and methanation synthesis in batch and flow reactors. With archetype model systems, some factors of the final amount of effluent CO_2 can be concluded, which provided a promising guide for the rapid development of (photo)thermocatalytic CO_2 conversion using sunlight as the clean and sustainable energy source.[8] In **Figure 2**, we summarize the major properties of the technologies for thermocatalytic, photocatalytic, and photothermocatalytic CO_2 conversion, highlighting the differences in reaction routes, products, advantages, and disadvantages of each technology.

Nowadays, the published reviews on CO_2 reduction mainly concentrated on a certain technology (e.g., thermocatalysis, photocatalysis), while a few have emphasized the integration of thermo- and solar energy in catalysis. Considering the rapid

and fascinating scientific research that have been sprung up in these important and hot topics, we herein present a comprehensive and timely review of the recent advances in thermo-, photo-, and the integrated photothermocatalytic CO_2 conversion to high-value-added chemicals and fuels during the past five years, aimed at highlighting the differences and similarities between solar- and thermo-driven catalysis in depth. The motivation and fundamentals of each catalytic technology are first introduced, followed by the emphatic discussions on their recent progress toward small molecules (e.g., formate, CO, CH_4, and alcohols) and fine chemical (e.g., C_{2+} olefins and oxygenates) synthesis. It mainly provides objective assessment on the merits and demerits of catalysts, in terms of catalytic activity, selectivity, and stability. Then, distinct catalytic mechanisms for these technologies are summarized to provide a comprehensive understanding of C=O activation and intermediate adsorption, which has been realized by the advanced studies of in situ/operando characterizations and theoretical calculations. Finally, the current challenges and future perspectives for the efficient utilization and upgradation of CO_2 into value-added products are addressed in these flourishing fields. Thus, this review provides horizontal comparisons by discussing different catalysts or reaction pathways for the same product. In parallel, this review provides vertical comparisons of the recent advances in catalytic technologies for CO_2 conversion. As a result, this review is expected to be an essential work to provide important references related to the chemical transformation of CO_2 into chemical feedstocks with explicit directivity.

2. Thermocatalysis

2.1. Motivation and Principles

Considering that CO_2 is a thermodynamically stable molecule, high pressures and temperatures are always required to achieve
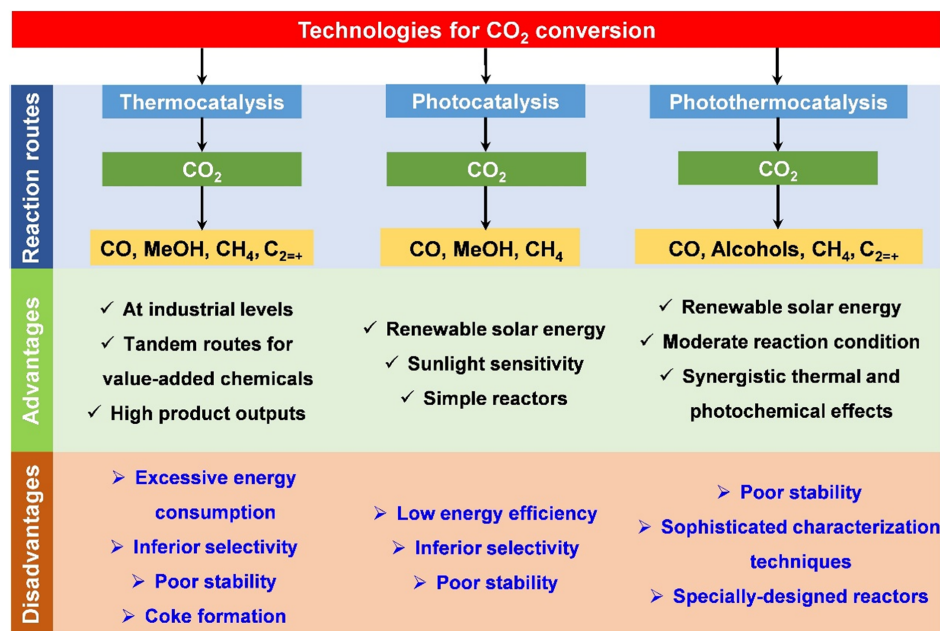

Figure 2. Properties of the technologies for thermo-, photo-, and photothermocatalytic CO_2 conversion.

C=O activation in the chemical conversion of CO_2-to-chemicals/fuels. Thermocatalysis driven by heat energy performs high efficiency and applicability for the mass-produced synthesis of fine chemicals (hydrocarbons, olefins, and NH_3, etc.) in conventional industrial manufacture. Accordingly, thermocatalytic CO_2 conversion has been an ideal candidate to generate high-value-added carbonaceous compounds, which mainly involve hydrogenation reactions with a CO_2 flow over catalysts at controllable temperatures and pressures. In the CO_2 thermocatalysis process, CO_2 molecules first adsorb on the surface of catalysts, and then essential activation energy (E_a) is required to bend C=O chemical bonds. Subsequently, another activation energy barrier should be overcome for the formation process of intermediates, where H_2 is directly used as the reductive reagent and *H donor. Finally, the interactions between intermediates and the catalyst surface influence the desorption ability of product molecules, which would exhibit different selectivities for C_1 chemicals or more valuable C_{2+} chemicals by regulating C—H bonding or C—C coupling. As shown in **Figure 3**a, the reaction process of CO_2 hydrogenation should overcome excessive energy barriers without the presence of catalysts (solid line), which need enough thermal energy to match to overcome the activation energy E_{a1} of the elemental step.[9] Thus, the development and employment of highly efficient catalysts is the key to accelerate the CO_2 conversion rate by lowering the E_{a2} and E_{a3} values (dashed line). In this regard, four main reaction pathways on thermocatalytic CO_2 conversion have sprung up in the recent 5 years, especially in the field of heterogeneous catalysis.

2.2. Plausible Routes for CO_2 Hydrogenation

Hydrogen is a high-energy carrier, which can be used to hydrogenate CO_2 into the products of CO, MeOH, CH_4, and other hydrocarbons (Figure 3b). The related reaction pathways are described as follows.

2.2.1. CO_2 to CO: Redox versus Associative Pathway

CO_2-to-CO conversion via RWGS reaction has been regarded as a promising route for CO_2 hydrogenation, which is an endothermic reaction driven by certain temperatures and pressures.[10]

$$CO_2 + H_2 \leftrightarrow CO + H_2O, \quad \Delta H_{298K} = 41.2\,kJ\,mol^{-1} \quad (1)$$
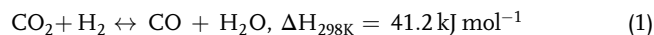
The reaction mechanisms have been generally classified into redox and associative mechanisms. 1) In a redox reaction, H_2 acts as a reductive reagent instead of a participant for the generation of intermediates. For example, Cu species supported on transition metal oxides/carbides (TMCs) has always been the popular alternatives for highly active and selective RWGS reactions. Cu^0 is first oxidized by CO_2 molecules to form Cu^+ and CO, and then Cu^+ can be reduced by H_2 to generate H_2O. The redox mechanism can be modeled as follows.

$$CO_2 + 2Cu^0 \rightarrow Cu_2O + CO \quad (2)$$

$$H_2 + Cu_2O \rightarrow 2Cu^0 + H_2O \quad (3)$$

Inspired by the abovementioned redox process, Konsolakis et al. employed Cu/CeO_2 as the catalyst and conducted thermodynamic analysis, realizing high CO_2 conversion (52%) and CO selectivity (95%) at 380 °C and ambient pressure.[11] Other Cu-based materials, such as Cu/ZnO[12] and Ru-decorated $Cu/ZnO/Al_2O_3$[13] catalysts, were also ideal alternatives for the activation and dissociation of CO_2 in the RWGS reaction. Compared with traditional metal oxide-supported Cu-based catalysts, Ma and co-workers synthesized highly dispersed Cu over β-Mo_2C (1.3 wt% Cu/β-Mo_2C) catalyst, which performed superior CO_2 conversion rate ($47.7 \times 10^{-5}\,mol_{CO2}\,g_{cat}^{-1}\,s^{-1}$) and extraordinary CO selectivity (99.2%) during a 40 h test (**Figure 4**).[14] The optimized activity and stability are attributed to the synergistic effect between Cu and β-Mo_2C, which contributed to the high dispersion of active Cu sites. During a redox reaction, the CO products were generated from CO_2 dissociation, while the oxygen atoms extracted from the CO_2 molecules were finally reduced by H_2 to produce H_2O. Consistent with the experimental results, the proposed reaction mechanism obtained via transient analysis[15] suggests that the CO_2 adsorption/activation
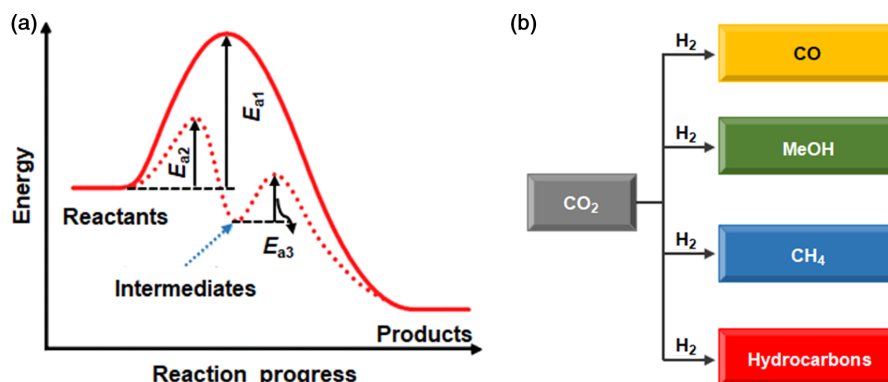

Figure 3. a) Energy diagram of the thermocatalytic reaction process. E_{a1}, E_{a2}, and E_{a3} indicate the activation energy for reactants and intermediates during the different reaction progresses of CO_2 hydrogenation. The solid and dashed lines illustrate the progress of the chemical reaction without and with the presence of a catalyst, respectively. Reproduced with permission.[9] Copyright 2019, Wiley-VCH GmbH. b) Four main products from thermocatalytic CO_2 hydrogenation reactions.
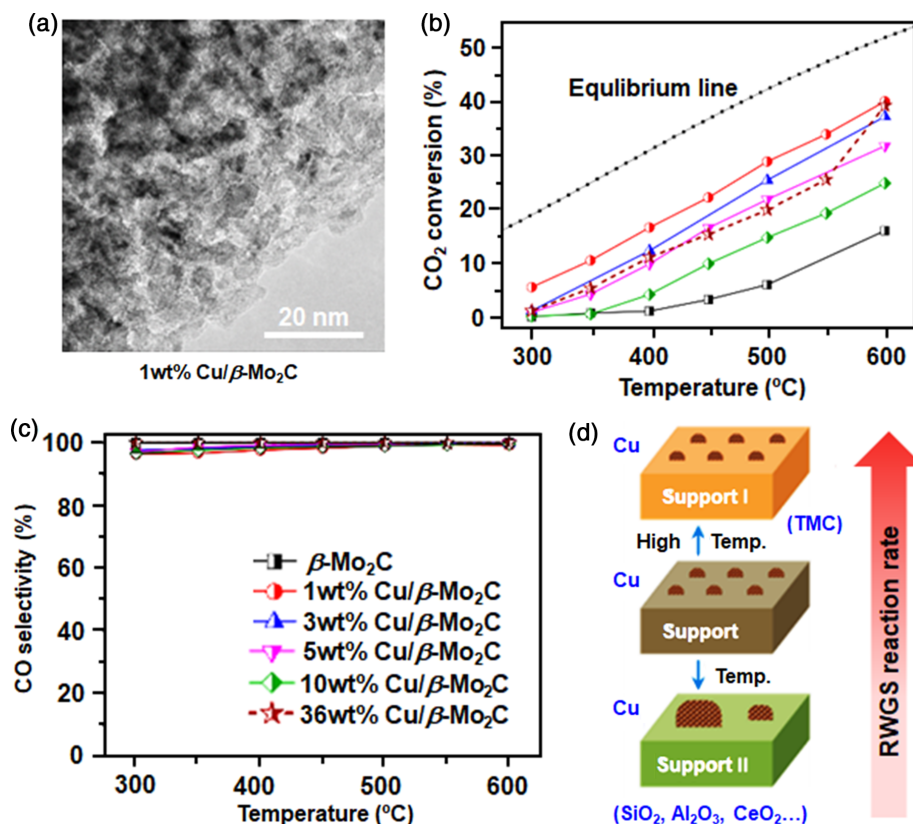
www.advancedsciencenews.com

ADVANCED
ENERGY & SUSTAINABILITY
RESEARCH
Open Access

www.advenergysustres.com

Figure 4. a) transmission electron microscope (TEM) image (scale bar, 10 nm) of 1 wt% Cu/β-Mo$_2$C sample. b) CO$_2$ conversion and c) CO selectivity of β-Mo$_2$C and Cu-modified β-Mo$_2$C catalysts in RWGS reaction. d) The illustration of RWGS reaction rates using different Cu-modified support catalysts under high temperature (TMC). Reproduced with permission.[14] Copyright 2016, American Chemical Society.

on the Cu sites is a rate-determining step, while the subsequent reduction of the adsorbed oxygen atoms of *CO$_2$ or hydroxyls of *COOH finally produces CO or H$_2$O molecules. Therefore, the introduction of metallic Cu is a promising way to lower the E_a of the rate-limiting step, which is conducive to the redox process.[16] The catalytic performance of the RWGS reaction via the redox mechanism can be further improved by some other strategies, such as alloying and constructing high-surface-area or nanostructuring catalysts. Reina's group reported that saponite-supported NiCu catalysts exhibited preferable selectivity for the formation of CO (≈80%) when compared with the saponite-supported NiCo and Ni catalysts.[17] As evidenced by X-ray photoelectron spectroscopy (XPS) results, an electronically rich Ni—Cu interface contributed to the effective CO$_2$ activation process. Furthermore, inverse nanoporous Cr$_2$O$_3$/Cu,[18] nanotube-structured TiO$_2$/Cu,[19] and double-shell nanofiber-structured CuSiO/CuO$_x$[20] presented strong metal—support interactions and offered abundant surface active sites for CO$_2$ activation and H$_2$ dissociation in CO$_2$-to-CO conversion. 2) In an associative pathway, metal oxides-supported metal catalysts are extensively employed as the active materials for CO$_2$ hydrogenation into formate intermediate and the subsequent C=O bond cleavage, thus selectively producing CO. The associative mechanism can be modeled as follows.

$$CO_2 + H_2 \rightarrow HCOO* + H* \tag{4}$$

$$HCOO* + H* \text{Decomposition} \rightarrow CO + H^2O \tag{5}$$
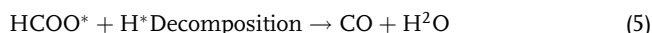
For example, Au supported on γ-Al$_2$O$_3$ catalyst achieves high selectivity for CO formation (>99%).[21] The hydrogenation of CO$_2$ to formate intermediates on Au sites and subsequent C=O bond breakage to CO product on γ-Al$_2$O$_3$ support were confirmed by diffusive reflectance infrared Fourier transform spectroscopy (DRIFT) measurement. Other metals (Pd or Ni) decorated on Al$_2$O$_3$ support catalyst[22] also display high activity as the formate intermediates can easily adsorb on these metal sites determined by the preferable H$_2$ dissociation and H adsorption capabilities. However, Ag exhibits inferior activity in RWGS reaction when compared with other metals. Hence, Kim et al. adopted in situ surface analysis and density functional theory (DFT) calculations to investigate the role of Ag sites. The results demonstrated that the absorbed carbonate species on the Ag surface hinders H$_2$ dissociation and H adsorption for CO production and thus hardly reach the thermodynamic conversion limit.

2.2.2. CO$_2$ to MeOH: CAMERE versus Formate Pathway

CO$_2$ to MeOH is an ideal application for large-scale MeOH production, which is extensively used as transportation fuel or as a building block for other high-value-added liquid fuels. It is an exothermic reaction that can proceed at a relatively low

**ADVANCED
SCIENCE NEWS**
www.advancedsciencenews.com

**ADVANCED
ENERGY & SUSTAINABILITY
RESEARCH**
Open Access
www.advenergysustres.com

temperature and a high pressure with the assistance of effective catalysts.

$$CO_2 + 3H_2 \leftrightarrow CH_3OH + H_2O, \Delta H_{298K} = -49.5\,kJ\,mol^{-1} \quad (6)$$
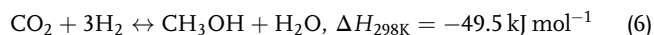
Two different mechanisms were proposed in the published literature,[23a,b] as illustrated in **Figure 5**a. One pathway that undergoes the RWGS reaction with CO acts as the reaction intermediate (CAMERE pathway) and then hydrogenates to MeOH via the conventional syngas-to-MeOH process

$(CO + 2H_2 \rightarrow CH_3OH)$. A recent study over nanointermetallic $InNi_3C_{0.5}$ first converted CO_2 into CO*,[24] which was then selectively hydrogenated into CH_3OH below 300 °C through CAMERE pathway, evidenced by DRIFT analysis (Figure 5b). Meanwhile, investigated by DFT analysis, the adsorbed CO_2^* easily converted into CO* with a low E_a (0.32 eV) through an exothermal process ($E_{reaction} = -0.38$ eV), which is preferable for the formate or carboxylate pathway. In addition, DFT calculations over Pd/TiO_2 catalyst also demonstrated that the CAMERE pathway is the primary route for MeOH production, and CO*-to-
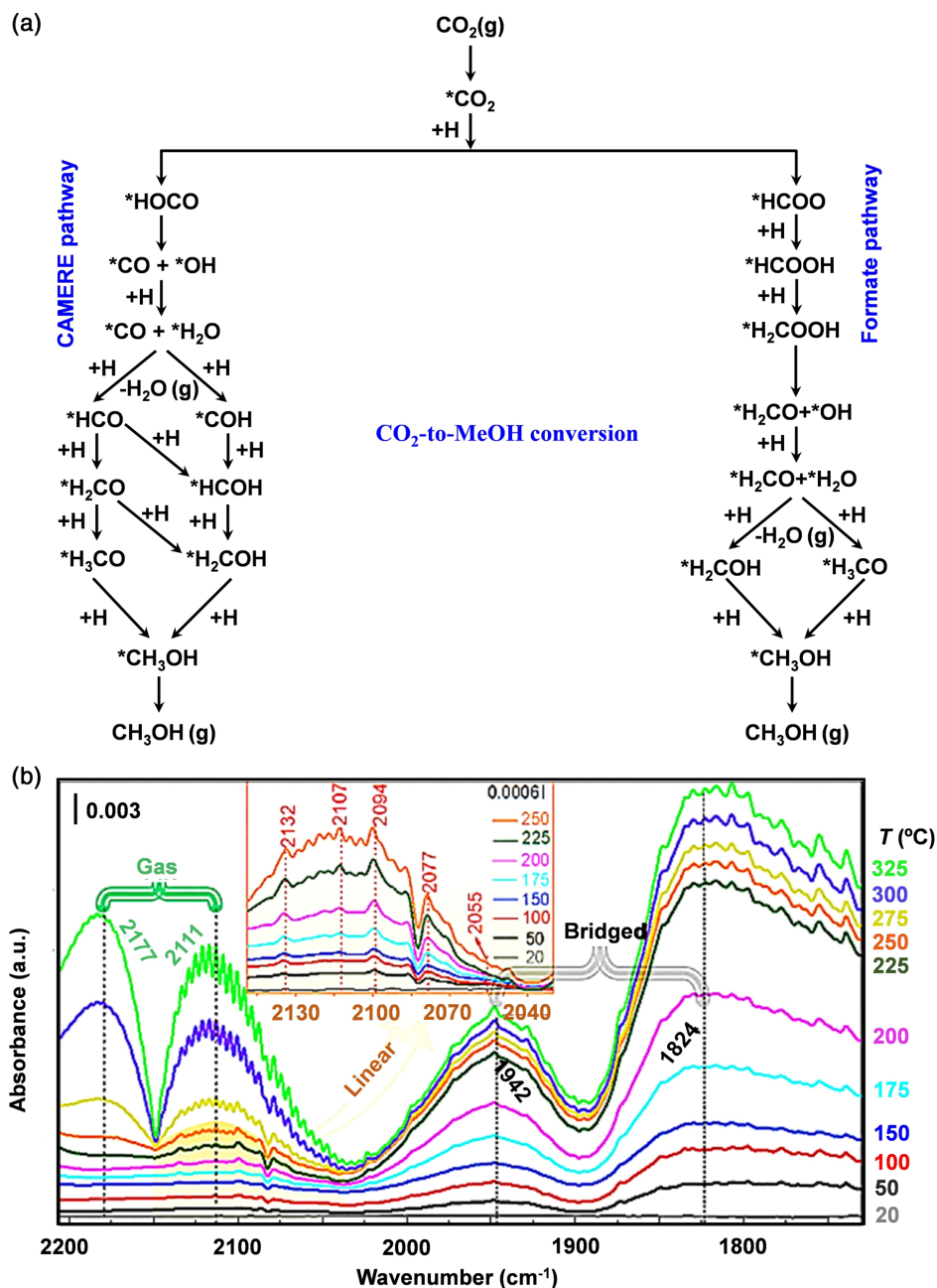

Figure 5. a) Reaction scheme for CO_2-to-MeOH conversion via CAMERE (left, RWGS + CO−hydro) and formate (right) pathways. Reproduced with permission.[23] Copyright 2014, Elsevier Ltd. In situ DRIFT measurements of CO_2 hydrogenation reaction against temperature on b) $InNi_3C_{0.5}$ via CAMERE pathway. Reproduced with permission.[24] Copyright 2019, Cell Press.

HCO* conversion is the rate-determining step.[25] The other pathway proposes that the first step of MeOH synthesis is the direct CO_2 hydrogenation through formate (HCOO*) or carboxylate (COOH*) intermediate, and the subsequent formate/carboxylate hydrogenation is regarded as the rate-determining step (formate pathway).[26] In situ DRIFT measurement confirmed that CO_2 was first activated and converted into HCOO* intermediate at a relatively low temperature in the presence of Co_4N nanosheets and then generated CH_2O* species with a further increase of reaction temperature.[27] Atomic Pt embedded in MIL-101 shows high turnover frequency (TOF) ($117\,h^{-1}$) and optimal selectivity for MeOH production (90.3%) at $150\,°C$ and 32 bar during CO_2 hydrogenation.[28] The Pt single atom and coordinated O atom synergistically contributed to H_2 dissociation and O−H formation. Afterward, the H atom in the O−H group combined with CO_2 to generate HCOO* intermediate. For neighboring Pt monomers,[29] CO_2 was first hydrogenated into formic acid (HCOOH) via the transformation of COOH* intermediate. The successive steps involve the HCOOH hydrogenation into $CH(OH)_2*$, CHOH*, and CH_2OH* intermediates and finally MeOH. The above reaction pathways effectively lower the activation energy and enhance the catalytic activity, which result in the preferable selectivity for MeOH production.

When referred to catalysts, Cu-based materials and metal oxide supports have been commonly applied in MeOH synthesis. In these catalysts, Cu serves as the main active component, whose performance can be enhanced by the incorporation of other elements (Zn, Al, Mg, Ca, Sr, Ba, Zr, Ti, F, etc.). The commercial $Cu/ZnO/Al_2O_3$ catalyst presented high selectivity and activity toward MeOH production by CO_2 hydrogenation, with the intermediates of HCOO, H_2COO, H_2COOH, CH_2O, and CH_3O.[30] However, the severe reaction conditions ($200−400\,°C$ or 20−100 bar) largely impede the economic feasibility of this technology. Delightedly, a low-temperature ($120−170\,°C$) CO_2-to-CH_3OH conversion with nearly 100% yield was realized using tertiary amine and alcohol through the condensed-phase hydrogenation of alkylcarbonate, accompanied by the generation of ammonium formate and alkylformate intermediates.[31] The incorporation of alkaline metal oxides (e.g., MgO, CaO, SrO, and BaO) into Cu/Al_2O_3 catalysts contributes to a higher Cu^+/Cu^0 ratio and surface area, which show a higher MeOH production rate and suppress the competing RWGS reaction.[32] Evidenced by DFT, DRIFT, and kinetic Monte Carlo (KMC) simulations, the reduced Zr^{3+} sites at the interface of $Cu/ZrO2$ catalysts preferably absorb the $*CO_2$, *CO, *HCO, and $*H_2CO$ intermediates, which moderately promote methanol synthesis on Cu.[33] In this work, TiO_2 can also enhance MeOH production on Cu via the RWGS pathway with carboxyl intermediates. Meanwhile, the formation rate of $*H_3CO$ is independent of the formation rate of *HCOO, suggesting that the CO_2-to-MeOH conversion does not follow the formate pathway for both catalysts. As the synergetic effect of Cu and ZnO is non-negligible in CO_2 hydrogenation, the ternary $Cu/ZnO/ZrO_2$ catalyst system is a potential candidate for this reaction and can be further enhanced by oxidative F_2–fluorination procedures.[34] With a mild difluorine treatment, the ZnO_x defect sites and the E_a for the RWGS reaction increase, while the E_a for MeOH production from CO_2 hydrogenation is nearly unchanged, thus

achieving optimized MeOH yield and selectivity. When compared with traditional Cu catalysts, many researchers have also engineered the d-band centers and the active center densities of Pd/Pt/Rh-based catalysts by incorporating non-noble metals to form an alloy and thus tuning their structures. Accordingly, an optimal Pd@Zn core−shell-structured catalyst was synthesized to further increase the kinetic barrier for CO formation, thus facilitating MeOH formation with the selectivity of 70% at relatively low pressure and temperature (2 MPa and $270\,°C$).[35] Similarly, Díez-Ramírez et al. reported a Pd−Cu−Zn/SiC composite catalyst, and PdZn served as the active site for highly efficient MeOH production from CO_2 hydrogenation (**Figure 6**a,b).[36] Zeng's group fabricated Pt_3Co octopods[37] and $Rh_{75}W_{25}$ nanosheets[38] to catalyze CO_2 hydrogenation with enhanced MeOH yields (Figure 6c–f). The alloying and specific morphology synergistically bring about the electronic effects of heterogeneous catalysts, which contribute to higher negative charge density and abundant active sites for enhanced CO_2 activation and intermediate adsorption.

2.2.3. CO_2 to CH_4: CAMERE versus Formate Pathway

CO_2 to CH_4 (Sabatier reaction) is thermodynamically favorable, whereas the conversion undergoes an eight-electron process with high kinetic barriers. Therefore, the development of highly efficient catalysts is demanded to achieve satisfactory rates and selectivities.

$$CO_2 + 4H_2 \rightarrow CH_4 + 2H_2O, \Delta H_{298K} = -252.9\,kJ\,mol^{-1} \quad (7)$$

Many studies have sprung up for the Sabatier reaction based on the supported transition metal (e.g., Ni, Co, Fe, Ru, Pd, and Rh) catalytic systems. Meanwhile, metal oxides (e.g., SiO_2, TiO_2, Al_2O_3, ZrO_2, CeO_2) and carbon-based materials are the most commonly used supports, which provide high surface areas and heat-resistant properties. Notably, CO_2 methanation involves two categories of mechanisms. 1) One involves CO_2-to-CO conversion followed by CO methanation, which proceeds via a Langmuir−Hinshelwood mechanism. In detail, the dissociation of CO_2 into CO* first happens through an RWGS reaction. Subsequently, methane can be generated by direct hydrogenation of CO* intermediate or through a two-step pathway of dissociation of CO* to the C* intermediate and further hydrogenation to methane. 2) The other one involves the direct hydrogenation of CO_2 to CH_4, and the formate species are suggested as the main reaction intermediates.[39] Based on the proposed mechanisms, commercialized Ni-based materials were widely studied for Sabatier reaction at relatively high temperatures to overcome kinetic limitations. Mutschler et al. reported that Al_2O_3-supported Ni catalyst showed the maximum CH_4 yield of 78% and selectivity of 98% at 623 K, accompanied with a small amount of gaseous CO (the highest CO yield of 18.2%).[40] To further increase the CO_2 conversion, Vita et al. synthesized Ni catalyst on gadolinium-doped ceria (Ni/GDC), which increased the amount of catalytic layer and thus achieved the highest CH_4 productivity ($10.7\,L_{CH4}\,g^{-1}\,h^{-1}$) at $400\,°C$ during a 200 h continuous test.[41] However, Ni-based catalysts show inactivation at a relatively high temperature as the interaction of Ni sites with CO intermediates could generate Ni carbonyl ($Ni(CO)_4$).
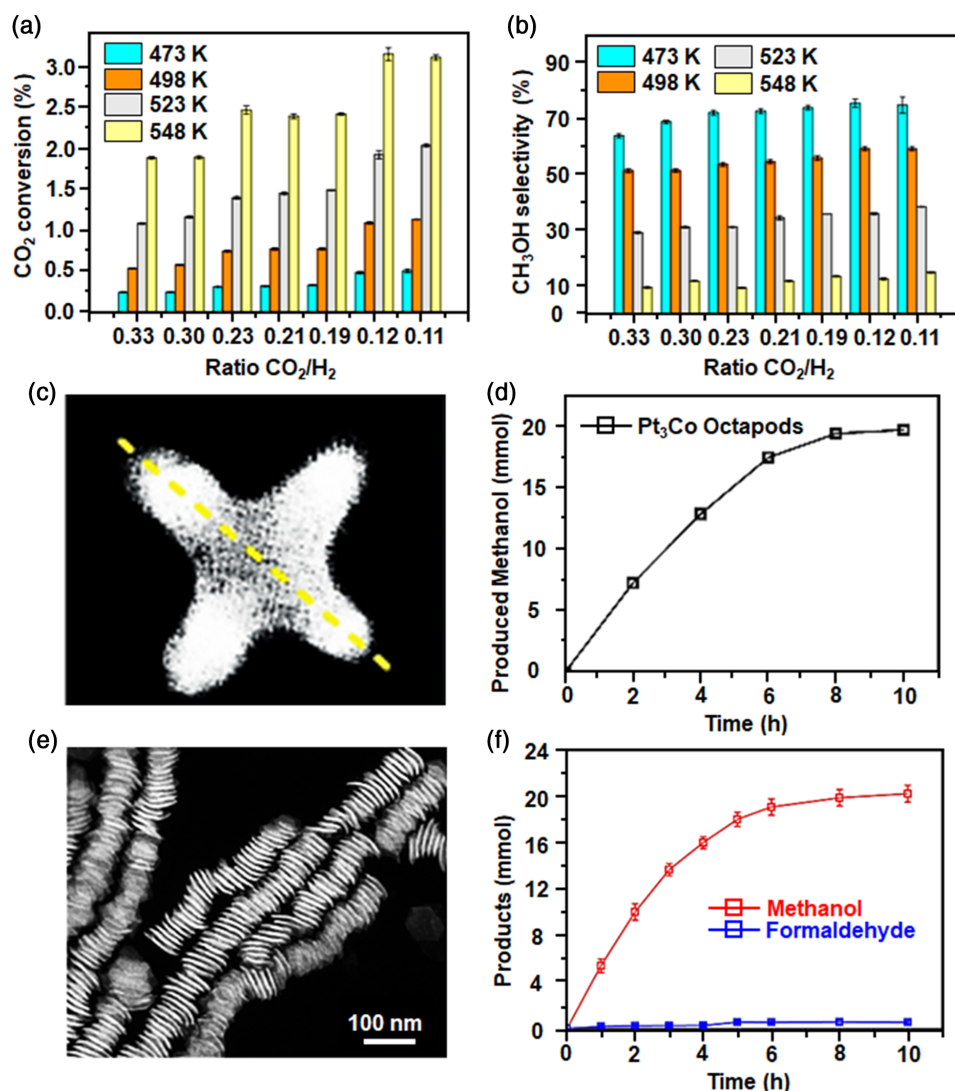
Figure 6. a) CO_2 conversion and b) CH_3OH selectivity of Pd−Cu−Zn/SiC composite during CO_2-to-MeOH conversion with only CO_2 and H_2 in the feed. Reproduced with permission.[36] Copyright 2018, Elsevier B.V. c) scanning transmission electron microscopy (STEM) image of a Pt_3Co octopod. d) Time course of the CO_2 hydrogenation into MeOH catalyzed by Pt_3Co octopods at 150 °C with CO_2 (8 bar) and H_2 (24 bar). Reproduced with permission.[37] Copyright 2016, Wiley-VCH GmbH. e) STEM image of $Rh_{75}W_{25}$ nanosheets. f) Time course of CO_2 hydrogenation into MeOH catalyzed by $Rh_{75}W_{25}$ nanosheets at 150 °C under 32 bar of H_2/CO_2 mixed gas ($H_2/CO_2 = 3:1$). Reproduced with permission.[38] Copyright 2017, American Chemical Society.

Therefore, the key is to develop efficient Ni-based catalysts and optimize reaction conditions, which ensure effective activation of the reaction system below 300 °C and finally achieve a high CH_4 yield. For example, the automethanation phenomenon that happened on Ni/metal oxide (CeO_2, ZrO_2, Y_2O_3, or Al_2O_3) at room temperature and atmospheric pressure was reported to enhance the CO_2-to-CH_4 performance by purging a raw material gas containing oxygen into the reactor.[42] The enhancement is mainly ascribed to the high thermal energy generated from H—O bond combustion under cofeeding with oxygen. Moreover, bulk $LaNi_5$ alloy is well known for its hydrogen storage capability, which was also selected to realize improved activity for the Sabatier reaction.[43] $LaNi_5$ supported on γ-Al_2O_3 showed a high CO_2 conversion (75%) and a superior CH_4 selectivity

(98%) at 1 atm and 300 °C (**Figure 7**a). From the DRIFT analysis (Figure 7b), the reaction went through an RWGS mechanism, which is described in detail as follows: H_2 was first dissociated into *H on the surface of Ni sites and subsequently, CO_2 was activated and dissociated on Ni sites. Then, the generated *CO rapidly adsorbed on LaO_x decorations, and part of *CO was successively decomposed into *C and *O. Finally, the hydrogenation of *CO or *C was conducted to generate CH_4. When compared to Ni, some noble metals (e.g., Ru, Pd, Rh.) are ideal alternatives for CO_2 methanation at low temperatures (≤300 °C). For instance, to reach the same CO_2 conversion (85%), the commercial Ru/Al_2O_3 catalyst could proceed with the methanation reaction at 200 °C, while Ni-based catalyst activates the reaction above 300 °C.[44] The reaction is suggested to be dominated by
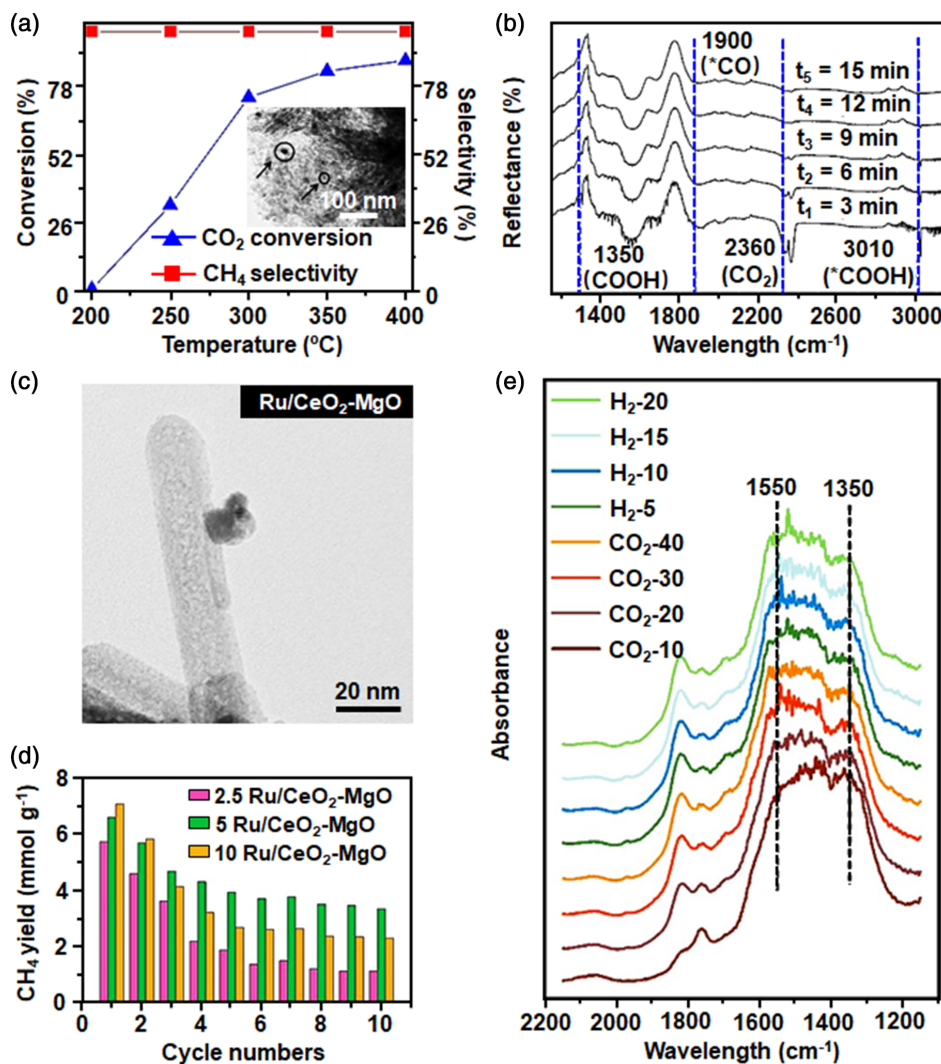
www.advancedsciencenews.com

**ADVANCED
ENERGY & SUSTAINABILITY
RESEARCH**
Open Access
www.advenergysustres.com

Figure 7. a) CO_2 conversion and CH_4 selectivity of La−Ni/γ-Al_2O_3 in the Sabatier reaction. The inset in (a) shows the TEM image of the La−Ni/γ-Al_2O_3 catalyst reduced in H_2 at 700 °C. b) The evolution of surface species as a function of time was analyzed by in situ DRIFT spectra of the La−Ni/γ-Al_2O_3 catalyst after H_2 injection over preadsorbed CO_2 at 400 °C and 1 bar. Reproduced with permission under the terms of the CC-BY license.[43] Copyright 2016, The Authors. Published by MDPI. c) TEM image and d) CH_4 yield after 10-cycle CCU process of 5 wt% Ru/CeO_2−MgO. e) In situ DRIFTS spectra during the CCU process of CeO_2−MgO. Reproduced with permission.[45] Copyright 2020, Elsevier Ltd.

the thermodynamic equilibrium, and thus the rapid reaction rate could be realized on Ru sites at a relatively low temperature without the requirement for an intermediate condensation step. Meanwhile, the metal loading of Ni is two orders of magnitude higher than that of Ru, indicating that Ru/Al_2O_3 is the preferable catalyst for small-scale CO_2 methanation application. Sun et al. demonstrated that 5 wt% Ru/CeO_2−MgO exhibited an efficient carbon capture and utilization (CCU) performance with a stable CO_2 conversion (79%) and CH_4 yield (3.36 mmol g^{-1}) after 10-cycle CCU processes (Figure 7c,d).[45] Meanwhile, the introduction of oxygen vacancies into the Ru-oxide support interface is beneficial to improve the stability of the whole reaction system. The in situ DRIFT (Figure 7e) was further employed to explore the mechanism of the CO_2 methanation process under the synergistic effects of active Ru sites and oxygen vacancies. The

proposed mechanism includes the following steps. 1) Adsorbed CO_2 molecules are activated by oxygen vacancies while CeO_2 support is oxidized, and H species are chemisorbed onto the active Ru sites. This step generates bidentate formate intermediate at the interface of metal−support, which was then dissociated into metal−carbonyl (Ru−CO) and O−H groups. 2) Ru−CO was hydrogenated by chemically adsorbed H species, which was finally converted into the CH_4 product and determined as the rate-determining step. In addition, strategies such as tailoring nanoparticle sizes,[46] optimizing structure and compositions,[47] altering reaction conditions (feed gas compositions, space velocity, temperature, and pressure),[48] and constructing intermetallics in alloys[49] have been adopted to develop efficient catalysts. By tailoring the suitable particle size of the Ru nanoparticles, the adsorption capacity of H species and the following

formation of CH_xO species by the consecutive hydrogenation of CO^* intermediate were certainly enhanced. The above-mentioned steps could promote the cleavage of the C—O bond, which was regarded as the rate-determining step of the CO_2 methanation process.[46]

Cored et al.[47] synthesized a core−shell-structured $Ru^0@RuC$ catalyst by a facile hydrothermal method, which showed superior activity for CO_2-to-CH_4 conversion below 200 °C with 100% selectivity (**Figure 8**a,b). Analyzed by isotopic $^{13}CO/^{12}CO_2/H_2$ experiments, the shell of RuC acted as the active site, which efficiently activates CO_2 and H_2, and finally CH_4 generation occurs via a direct CO_2 hydrogenation mechanism. Although noble metals (e.g., Ru, Rh, and Pd) have exhibited remarkable catalytic performance in the Sabatier reaction, the high cost and low storage have hindered their large-scale applications. Therefore, alloying noble metals with cheap metals (e.g., Fe, Co, Ni, Mn, Cu) can reduce the system cost and moreover, bring about the electronic effect and geometric effect for the enhanced catalytic activity. Herein, Zeng's group demonstrated that face-centered tetragonal (fct)-PdFe intermetallic nanocrystals (NCs) presented high mass activity (5.3 mmol $g^{-1}h^{-1}$) and stability for CO_2 methanation at 180 °C under 1 bar, which was 1.6, 3.3, and 5.3 times as high as that of Ru, Ni, and Pd (Figure 8c,d).[49] Evidenced by DRIFT measurements and DFT calculations, the metallic Fe sites were demonstrated to play a vital role in fct-PdFe intermetallic NCs, which facilitated the direct conversion of CO_2 into CO^* intermediates, thus resulting in the enhanced hydrogenation of $*CO$ into CH_4.

2.2.4. CO_2 to C_{2+} Hydrocarbons: FT Synthesis versus Methanol-Mediated Pathway

CO_2 to hydrocarbons involves two different pathways, namely, the modified FT synthesis (FTS) and the methanol-mediated synthesis. The two pathways of thermocatalytic CO_2 hydrogenation can generate different products, which can be used as important industrial intermediates and high-value-added chemicals, etc. They are mainly alkanes (liquefied petroleum gas [$C_3−C_4^0$] and gasoline [$C_5−C_{11}$]), alkenes (lower olefins [$C_2−C_4$=]), and aromatics.

1) The FTS pathway first generates CO from CO_2 hydrogenation via RWGS reaction and then obtains hydrocarbons through FTS ($CO_2 + H_2 \leftrightarrow CO + H_2O$; $n\ CO + 2m\ H_2 \leftrightarrow C_nH_{2m} + m\ H_2O$). The first RWGS step in modified FTS is an endothermic reaction, which requires high temperatures to activate CO_2 molecules and accelerate reaction rates. However, FTS is an exothermic reaction, which indicates that lower temperatures could lead to fast hydrogenation of CO to multicarbon products.[50] Meanwhile, FTS goes through multiple steps, which involve reactants adsorption, chain initiation, growth, and termination, as well as product desorption for CO hydrogenation into carbonaceous compounds.[51] Therefore, different catalysts and reaction conditions (temperatures, pressures, and CO_2/H_2 ratios) could significantly influence the CO_2 conversion rate and product yield as well as selectivity. As the traditional RWGS catalysts, Fe-based materials have been applied in the modified FTS process owing to their low cost and flexibility. In general, modification of these Fe-based catalysts is a prerequisite to realize enhanced CO_2
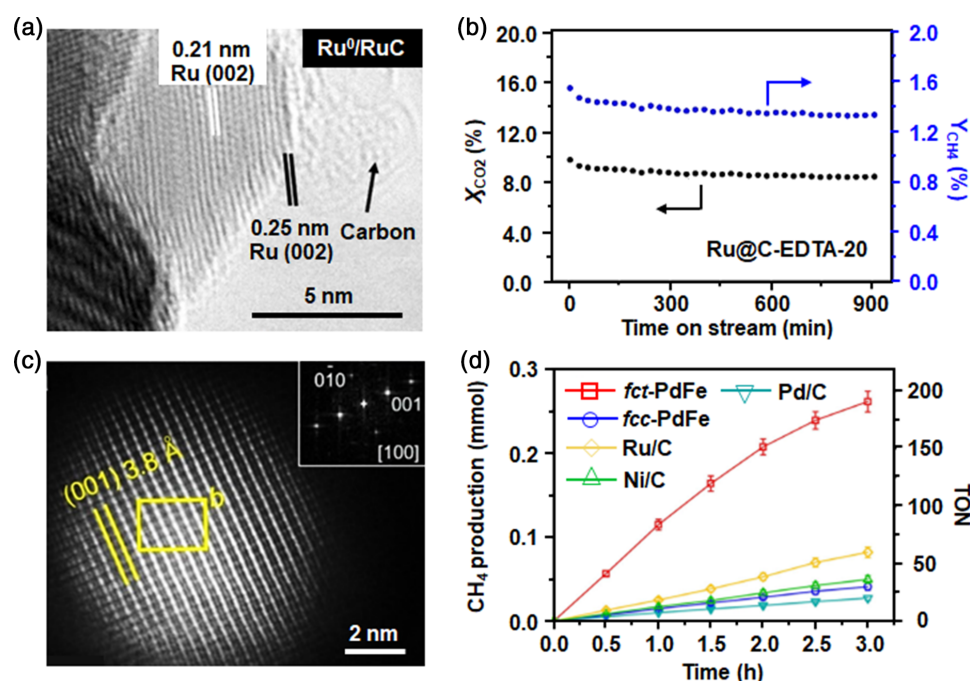
Figure 8. a) High-resolution transmission electron microscopy (HRTEM) image and b) CO_2 conversion (left axis, black) and CH_4 STY (right axis, blue) of $Ru^0@RuC$ catalyst. Reproduced with permission.[44] Copyright 2019, American Chemical Society. c) high angle ring dark field (HAADF)−STEM image, d) time versus CH_4 yield (left axis)/TON numbers (right axis) for fct-PdFe, face-centered cubic (fcc)-PdFe, Ru/C, Ni/C, and Pd/C. Reproduced with permission.[46] Copyright 2020, Wiley-VCH GmbH.

hydrogenation performance. The modification strategies can be categorized into the following four groups:

a) In situ structural transformation. Fe_2O_3 was reported to prefer the formation of light olefins (C_{2+}) rather than paraffin and suppresses the selectivity toward CH_4 and CO production at 623 K under a total pressure of 15 bar in CO_2 hydrogenation.[52] Analyzed by the X-ray diffraction (XRD) pattern and Mössbauer spectrum, the characteristic peak of iron carbides (Fe_5C_2) could be detected during CO_2 hydrogenation condition, which was obtained from the in situ transformation of Fe_2O_3. Importantly, Fe_5C_2 plays a vital role in the high selectivity of light olefin production and suppresses the high yield of CH_4 as Fe_5C_2 is an active phase to promote the FTS process and chain growth reaction. Accordingly, either the direct CO_2 methanation or CO-based FTS into CH_4 could be suppressed over the Fe_2O_3-based catalyst, and thus the selectivity of C_2-C_4 hydrocarbons increases to a value of 37% with the olefin to paraffin ratio of 2.7 at CO_2 conversion of 40%. Meanwhile, the selectivity of C_{5+} hydrocarbons reaches 36%, while the values of CH_4 and CO were only 12% and 15%. This work provides in-depth sight into the fabrication of Fe-based catalysts toward CO_2 hydrogenation in terms of facilitating short-chain olefin formation and suppressing undesired C_1 products.

b) Alkali metals promotion. Alkali metals (e.g., Na and K) can act as promoters when introduced into Fe-based catalysts, which enhances the yield and selectivity for olefin production by

accelerating CO dissociation and suppressing H_2 adsorption. In addition, the promoters significantly facilitate the formation of Fe carbides, which are well known as the active species for FTS reaction. Huang's group synthesized a series of Fe-based catalysts with different amounts of Na dopants for CO_2 hydrogenation.[53] When Na content increases, CO_2 conversion rate and alkenes selectivity are optimized, and the highest values can be up to 36.8% and 64.3%, respectively, with the Na content of 1% (**Figure 9**a). With the assistance of the comprehensive investigations on the physical and chemical properties of xNa/Fe (x indicates the weight percent of Na in wt%) catalysts, the promotion effects of Na dopant were determined to be the following key points. First, the interaction between catalysts and CO_2 molecules can be further enhanced in the presence of Na, which makes easier CO_2 activation. Second, Na facilitates the carbonization of Fe_3O_4 species in the presence of CO that is in situ generated from CO_2 hydrogenation, thus improving the formation and stability of Fe_5C_2 active species. The increasing amount of Fe_5C_2 species favors subsequent C—C coupling and carbon chain growth for heavier olefins (C_2-C_4 olefins and C_{5+} hydrocarbons) production. Third, Na as a promoter could increase the CO dissociation and adsorption rate, considering that CO is an important reaction intermediate in the catalytic process of CO_2 hydrogenation into alkenes over Fe-based catalysts, which was also reported in a previous study.[54] Meanwhile, the Na promoter could inhibit the secondary hydrogenation of alkenes into alkanes as it can break the symmetry of
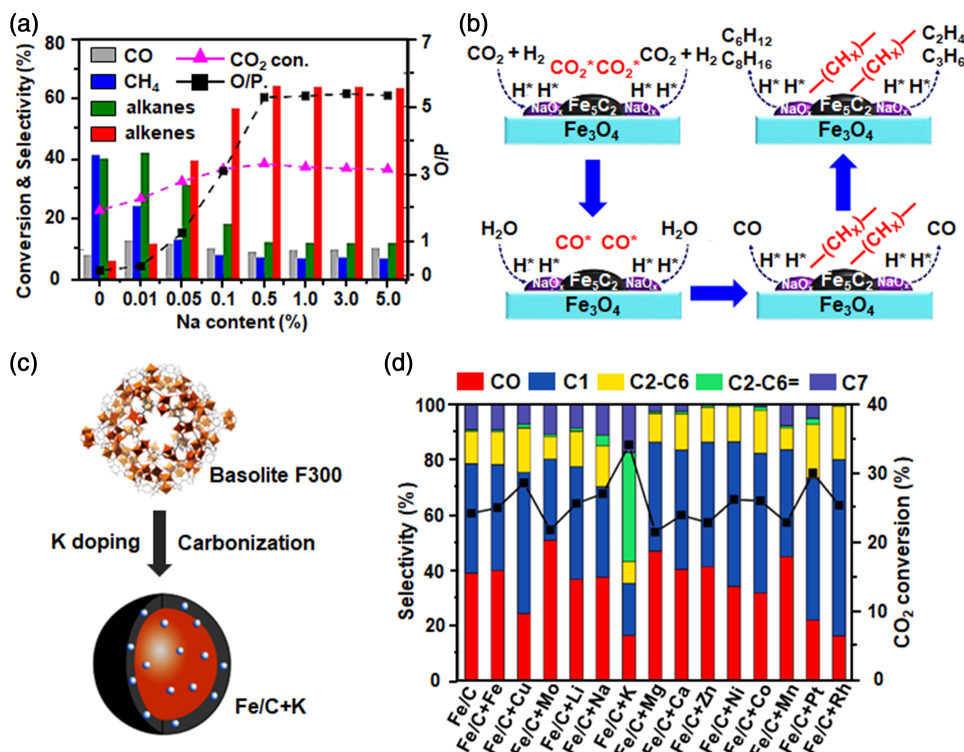
Figure 9. a) Catalytic performance of xNa/Fe (x indicates the weight percent of Na in wt%) catalysts toward CO_2-to-hydrocarbons conversion. b) The possible pathway of Na/Fe catalyst for CO_2 hydrogenation to olefins reaction. Reproduced with permission.[53] Copyright 2018, American Chemical Society. c) Synthetic scheme of Fe/C + K catalyst. d) CO_2 conversion and product distribution of promoted and unpromoted Fe catalysts in CO_2-to-hydrocarbons. Reproduced with permission.[55] Copyright 2018, American Chemical Society.

**ADVANCED
SCIENCE NEWS**

www.advancedsciencenews.com

**ADVANCED
ENERGY & SUSTAINABILITY
RESEARCH**
Open Access

www.advenergysustres.com

olefins and thus accelerate the desorption of olefins from the surface of the catalysts. Therefore, 1Na/Fe catalysts exhibited preferable heavy alkenes generation, while the selectivity toward methane production decreased to 7.2%. The possible reaction pathway is described as follows (Figure 9b): following a modified FTS process, CO_2 and H_2 molecules are first adsorbed and activated on the surface of the 1Na/Fe catalyst, and subsequently, the CO* species and H_2O are generated via RWGS reaction. Then, the CO* species are dissociated and further hydrogenated into CH_x species and finally transformed into alkenes through a C−C coupling reaction. Potassium is also a popular promoter for Fe catalysts in CO_2 hydrogenation, which facilitates CO_2 capture via a well-known "potassium carbonate mechanism." Moreover, K as an electron donor can accelerate the electron transfer from Fe-based catalysts to *CO intermediate, thus leading to higher selectivity toward olefins production via the FTS process. An active and stable Fe-based catalyst derived from the metal−organic framework (MOF) was reported by Ramirez et al. Potassium was found to be a great promoter, improving the space−time yields (STYs) toward C_2−C_4 olefin (33.6 mmol g_{cat}^{-1} h^{-1}), which was significantly higher than other dopants (e.g., Cu, Mo, Li, Na, K, Mg, Ca, Zn, Ni, Co, Mn, Fe, Pt, and Rh) (Figure 9c,d).[55] The possible reasons for the optimized promotion effects of the K lie in the fact that element K maintains the stability of Fe_3O_4 and Fe_5C_2, which act as essential active species in CO_2 hydrogenation. Followed by the proposed reaction pathway, CO_2 was first adsorbed on Fe_3O_4 active sites and converted into CO via the RWGS reaction and then underwent the hydrogenation process of CO via FTS on Fe_5C_2 sites to produce light olefins (C_2−C_4). In addition, the K promoter can enhance the adsorption capability of CO_2 and CO molecules while weakening H_2 affinity, which causes a higher CO coverage and a lower H_2 coverage on Fe-based reaction centers for a higher selectivity to olefins. Olefin selectivity on Fe_5C_2 sites is closely associated with the secondary hydrogenation of olefins, which results in further chain growth and an overhydrogenation reaction. Therefore, during the FTS process, the K promoter strengthens the Fe─C bonds rather than the Fe─H bonds, contributing to a higher CO coverage on the surface of Fe-based active species. The increase of the CO/H_2 ratio protects the catalyst surface from olefin readsorption and suppresses the formation of undesirable paraffin. Recently published studies demonstrate similar promoting effects of K element doping into Fe−Al−O spinel catalyst toward CO_2 hydrogenation reaction.[56a,b] To conclude, the K promoter imposes critical impacts on the catalyst phases (i.e., Fe oxides or carbides), chemical compositions, electronic states, and stability of the resulting Fe-based catalysts. Other K phases have also been introduced into Fe-based catalysts to activate CO_2 and subsequently convert it into olefins through a tandem mechanism (RWGS + FTS pathways). For example, $Fe_2O_3@KO_2$ and $Fe_2O_3@K_2CO_3$ reported by Gascon's group yield similar productivities of olefins when compared with the commercial FTS catalysts.[57a,b]

c) Other metals promotion. Some non-noble metals, such as Cu, Zn, Mn, Co, and Ti, have also been introduced into Fe-based catalysts for CO_2 hydrogenation. Cu promoter acted as a structural modifier that can increase Fe dispersion in the catalyst. Meanwhile, the incorporation of Cu into the Fe bulk lattice brought about optimized electronic effects, which facilitated

CO_2 activation and hydrogenation. Moreover, the olefin product distributions can be affected by alloying Fe with Cu. Noted that the addition of alkali metal further improves the RWGS and FTS tandem reactions as either a metallic or metal carbide active species can be maintained due to the interactions between Cu and K promoters. Hwang et al. reported that Fe−Cu−K catalyst showed high activity for liquid hydrocarbons production toward CO_2 hydrogenation,[58] which exhibited a C_{5+} yield of 18.1%, much higher than that of Fe−K (12.8%) and Fe−Cu (2.3%) catalysts. The experimental results reveal that K is mainly responsible for CO formation; Cu–Fe species facilitates C−C coupling; Fe–Cu–K catalyst promotes the chain growth reactions. Higher alcohol synthesis (HAS) has been regarded as a popular pathway to obtain high-value C_{2+} chemicals from CO_2 hydrogenation. The catalysts applied in HAS process should keep a balance between alcohol formation (via dissociative CO activation) and olefin generation (via nondissociative CO activation) to achieve an optimal selectivity for C_{2+} alcohols. Noble palladium has been used to achieve high selectivity for ethanol production, but the high cost impedes its large-scale application.[59] Xu et al. recently synthesized a CuFeZn catalyst with the addition of Cs promoter,[60] which exhibited a satisfactory CO_2 conversion efficiency (36.6%), $C_{2+}OH$ selectivity (19.8%), $C_{2+}OH$ STY (1.47 mmol g_{cat}^{-1} h^{-1}), and $C_{2+}OH/ROH$ fraction (93.8%) (**Figure 10**a,b). The DRIFT and temperature-programmed surface reaction (TPSR) results indicated that the synergistic effects of Cu−ZnO and Cu−Fe_7C_3 active sites promoted a tandem reaction for the C_{2+} alcohol synthesis. In detail, RWGS reaction first proceeded on Cu−ZnO sites to form CO* intermediates, which were hydrogenated into $C_{2+}OH$ via surface alkyl intermediates over Cu−Fe_7C_3 sites, therefore simultaneously suppressing the direct CO_2 hydrogenation into methanol via formate intermediates (Figure 10c). Meanwhile, higher CO_2-to-alcohol conversion was achieved with the addition of 3 wt% Cs promoter as Cs addition weakens hydrogenation ability, similar to the role of K promoter played in CO_2 hydrogenation. Other transition metals like Mn and Co were also incorporated into Fe-based catalysts to obtain high CO_2 conversion and optimal selectivity for light olefins production.[61a,b] These studies prove that the Mn and Co can be preferable alternatives for enhanced CO_2 adsorption and activation while hindering the secondary hydrogenation to reach high olefin/paraffin (O/P) ratios. Compared with the bulk morphology of Fe, element Ti was introduced as a structural promoter into the Fe-based catalyst to form a Fe−Ti−O-layered oxide material, which results in higher dispersion of Fe active sites and more stable phrase structure for highly selective CO_2-to-olefins conversion.[62]

d) Supports optimization. Different supports have been applied to optimize the metal dispersity, size, and metal−support interactions that resulted from their unique physicochemical properties. Metal oxides are supposed to be ideal candidates used in metallic catalysts with alkali promoters to synthesis high-value chemicals via CO_2 hydrogenation. For example, Shi et al. synthesized a series of TiO_2-supported Co−Cu catalysts with a suitable amount of K promoter,[63] which could reach a maximum C_{5+} yield with a moderate CO_2 conversion (13%), C_{5+} selectivity (35.1 C mol%), and high stability under steam (200 h). Zeolites as another traditional support possess a unique structure, and acidity, which is in favor of oligomerization/aromatization/
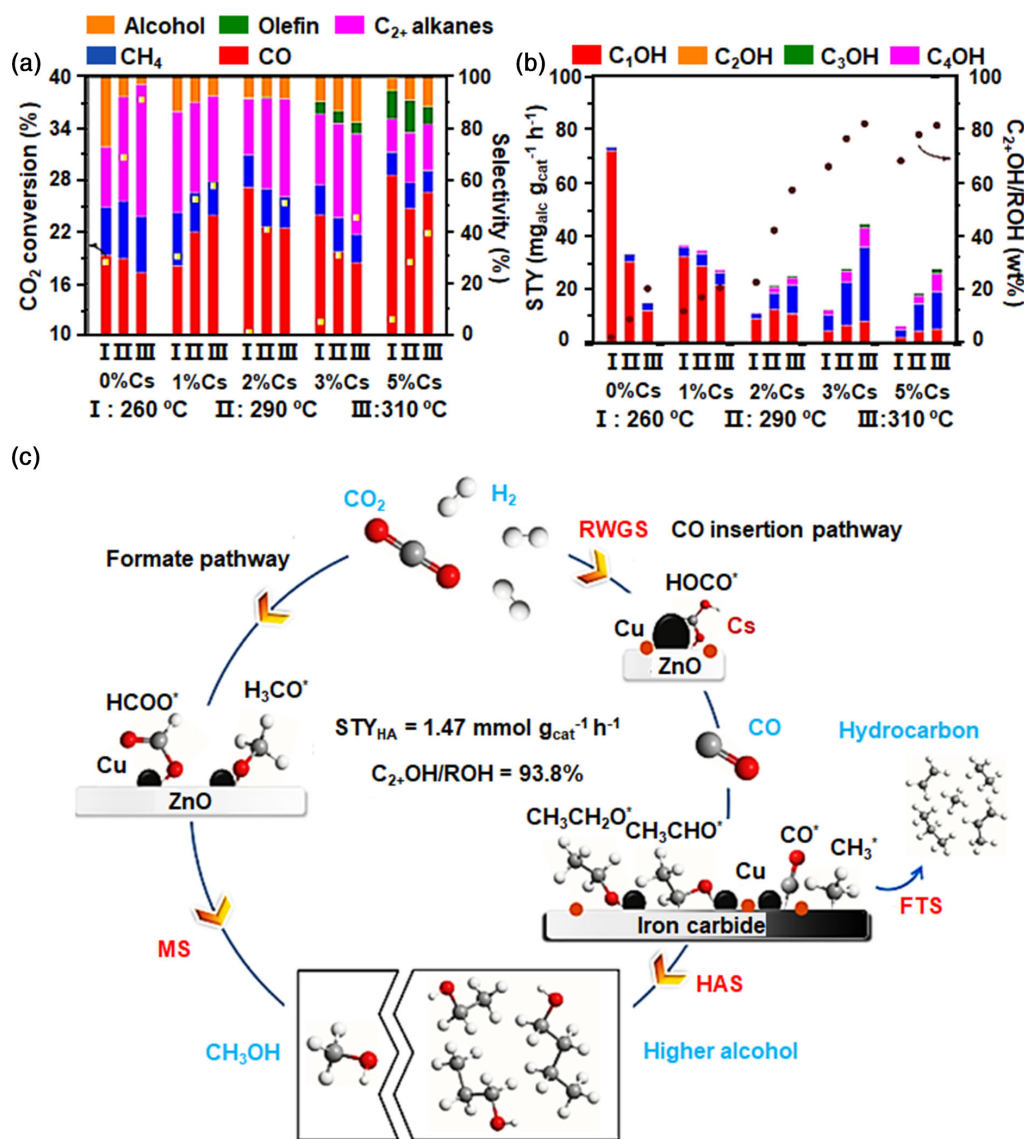
ADVANCED
SCIENCE NEWS

www.advancedsciencenews.com

ADVANCED
ENERGY & SUSTAINABILITY
RESEARCH
Open Access

www.advenergysustres.com

Figure 10. a) CO_2 conversion (yellow open squares) and selectivities of alcohol, olefin, C_{2+} alkane, CH_4, and CO in all carbon products. b) Distribution of alcohols in STY and weight fraction of $C_{2+}OH/ROH$ (brown solid circles) over $x\%Cs$−CuFeZn catalysts. c) The possible pathway of Cs−CuFeZn in CO_2 hydrogenation. Reproduced with permission.[60] Copyright 2020, American Chemical Society.

isomerization of hydrocarbons. Accordingly, Wei et al. combined Na−Fe₃O₄ catalyst with an HZSM−5 zeolite into a multifunctional catalyst,[64] which hydrogenated CO_2 into heavy hydrocarbons (C_5–C_{11}) with a selectivity of 78% among all hydrocarbon products, whereas efficiently decreases methane yield. Meanwhile, the as-synthesized catalyst showed superior stability during a 1000 h test, which could be comparable with the industrially applied catalysts for CO_2 conversion into liquid fuels. The proposed pathways of Na−Fe₃O₄/zeolite-multifunctional catalyst for CO_2-to-liquid fuels conversion are described as follows: CO_2 molecules are first activated and reduced to CO after hydrogenation via RWGS process on Fe₃O₄ active species and then the hydrogenation of CO to olefins on in situ-formed Fe₅C₂ sites via FTS reaction. Subsequently, the olefin intermediates

could diffuse to zeolite acid sites and process a series of oligo-merization/isomerization/aromatization reaction steps, and thus the heavy hydrocarbons, especially gasoline-range isoparaffins and aromatics, are formed after desorption from zeolite pores. In addition, a variety of carbon-based materials such as carbon nanotubes, porous carbons, and carbon nanofibers have also been selected as promising supports due to their thermal conductivity, high surface area, electron enriched surface, and high stability. Herein, single-walled carbon nanotubes[65] and mesoporous carbon[66a,b] are synthesized as supports for Fe-based materials, which realize enhanced CO_2 conversion efficiency, optimized selectivity of light olefins (C_2–C_4), and O/P ratio at catalytically active Fe carbide sites through a tandem reaction combining RWGS with FTS processes.

**ADVANCED
SCIENCE NEWS**

www.advancedsciencenews.com

**ADVANCED
ENERGY & SUSTAINABILITY
RESEARCH**
Open Access

www.advenergysustres.com

2) The methanol-mediated synthesis pathway for CO_2-to-hydrocarbons conversion also involves two steps, namely, CO_2 is first hydrogenated into MeOH and then reduced into multicarbon compounds. In recent five years, many studies focus on the MeOH-to-olefin conversion, which was thermodynamically initiated at high temperatures (>300 °C). However, CO_2-to-MeOH conversion is an exothermic step that is not favored at such high temperatures, and CO is produced as a byproduct through an endothermic RWGS process. Therefore, zeolite as a solid acid catalyst has been applied for C−C coupling (≥350 °C) and converts MeOH into olefins, which effectively suppresses CO production. Especially, the SAPO-34 and ZSM-5 zeolites are commonly used as active components for methanol conversion to olefin processes at a level of industrialization. Combining $ZnO−ZrO_2$, $CuO−ZnO−ZrO_2$, $In_2O_3−ZrO_2$, $ZnGa_2O_4$, or $ZnO−Y_2O_3$ with SAPO-34 zeolite as composite catalysts have been applied to CO_2 hydrogenation. When referred to SAPO-34, the generated MeOH intermediate is first converted into active hydrocarbon pool species $((CH_2)_n)$ inside the channels. Then, MeOH reacts with $(CH_2)_n$ species to produce light olefins $(C_2−C_4)$ and is further converted into higher olefins, alkanes, and aromatic through condensation, alkylation, and cyclization processes.[67] Li's group reported a $ZnO−ZrO_2$/SAPO tandem catalyst that successfully converted CO_2 into light olefins $(C_2−C_4)$ with high selectivity of 80−90% among hydrocarbon products (**Figure 11**a,b).[68] CO_2 hydrogenation proceeded on the surface of $ZnO−ZrO_2$ to generate CH_xO intermediates (precursors of MeOH), and subsequently lower olefins were produced on the SAPO zeolite (Figure 11c). To improve the catalytic activity of CO_2-to-MeOH conversion of Zn−Zr composites, Cu−ZnZr catalyst with core−shell structure was synthesized by Chen et al.[69] Under a low concentration of MeOH intermediate, the reduced contact interface and hydrogenation ability on the reaction centers successfully suppress CH_4 production and achieve a high olefin selectivity of 72% at 400 °C and 2 MPa total pressure. The hybrid catalyst of $In_2O_3−ZrO_2$/SAPO-34 was also found to exhibit high selectivity of $C_2−C_4$ olefins with an ideal CO_2 conversion efficiency at 400 °C via a direct tandem catalysis process,[70] by combining a CO_2–to–MeOH catalyst $(In_2O_3−ZrO_2)$ with a methanol-to-olefins catalyst (SAPO-34). In other words, methanol could be generated at the active sites (oxygen vacancies) of $In_2O_3−ZrO_2$ in the first step, which subsequently went through the SAPO-34 channels and was converted into light olefins automatically.[71] The vital roles of the oxygen vacancies were also confirmed on $ZnGa_2O_4$ catalyst toward the direct conversion of CO_2 to $C_2−C_4$ olefins.[72] Analyzed from in situ infrared spectroscopic tests, the oxygen vacancies effectively activated CO_2 molecules, and simultaneously −Ga−O− and −Zn−O− pairs dissociated H_2 into H species. Then methoxide species (CH_3O*) were formed upon prolonging the time, which were further hydrogenated into MeOH intermediates. Finally, MeOH diffused into the channels of SAPO-34 and thus selectively generated light olefins. As a bifunctional oxide−zeolite catalyst could initiate CO_2-to-MeOH and C−C coupling on two different active sites, $ZnO−Y_2O_3$-incorporated SAPO-34 zeolite was reported as another alternative to realize a high selectivity of light olefins production (83.9%) with low CH_4 selectivity (1.8%) toward CO_2-to-hydrocarbons.[73] ZSM-5 zeolites have been applied together with other metal

oxides to enhance the selectivity of valuable C_{5-11} fuels in CO_2 hydrogenation. The involved mechanism was the concept of the dual cycles: olefins-based cycle and aromatics-based cycle.[74] Methanol intermediates were first converted into olefinic species, and then propene and higher alkenes were obtained from alkenes methylation and cracking in the olefins-based cycle. Meanwhile, higher alkenes could be converted into toluene by oligomerization and cyclization. Furthermore, in the aromatics-based cycle, ethene was generated from methylation of toluene and side-chain elimination. Moreover, aromatics were simultaneously generated by successive oligomerization, cyclization, and dehydrogenation processes. Accordingly, an active catalyst composed of $ZnO−ZrO_2$ aerogel and H-ZSM-5 zeolite $(ZnO−ZrO_2$/H-ZSM-5) realized CO_2 conversion of 16% with the aromatics selectivity of 76%,[75] while the selectivity of CH_4 was less than 1% at 340 °C and 40 bars (Figure 11d,e). The MeOH intermediate was first generated over the oxygen vacancies on the surface of $ZnO–ZrO_2$, and then the aromatic hydrocarbons were generated from MeOH species in H-ZSM-5 via the above mechanisms (Figure 11f). Similarly, the $ZnCrO_x–ZnZSM-5$ compound was used in CO_2-to-hydrocarbons conversion, which resulted in the highest aromatics selectivity of 81.1% in C_{5+} hydrocarbons with 19.9% CO_2 conversion at 320 °C.[76]

3. Photocatalysis

3.1. Motivation and Principles

Photocatalytic CO_2 reduction (PCR), the so-called artificial photosynthesis, takes advantage of solar energy to activate CO_2 molecules and subsequently convert them into different products such as HCOOH, CO, CH_4, HCHO, or CH_3OH over semiconductors (**Figure 12**a). PCR is a promising technology that can convert CO_2 waste into solar fuels, thus realizing the recycling of renewable carbon fuels and retaining carbon neutrality without secondary pollution. Though much efforts have been made to optimize CO_2 photoreduction to fuels under solar light, the overall photoconversion efficiencies are very limited for practical application and there is a lack of a standard for solar-driven CO_2 conversion efficiency that needs to be achieved for practicality. Therefore, if a CO_2-to-fuel photoconversion technology is ever to become a reality, a significant advance is required. Recently, a rationally designed Cu−Pt/TiO_2 photocatalyst reported by Sorcar et al. could achieve a satisfying photoconversion efficiency of 1.0% with an apparent quantum yield (AQY) of 86% over 6 h under artificial sunlight (AM1.5), which successfully converted CO_2 and H_2O to a fuel compatible with our current energy infrastructure.[77] Nevertheless, the reaction mechanisms are required to be thoroughly explored, which can contribute to the optimization of the photocatalysts and photocatalytic processes.

In general, the PCR process involves four steps: 1) the formation of excitons within semiconductors upon the illumination with efficient energy larger than the bandgaps of the semiconductor photocatalysts; 2) excitons' dissociation into hot electrons to the conduction band (CB) and leaving holes in the valance band (VB) driven by the built-in electric field; 3) charge carriers
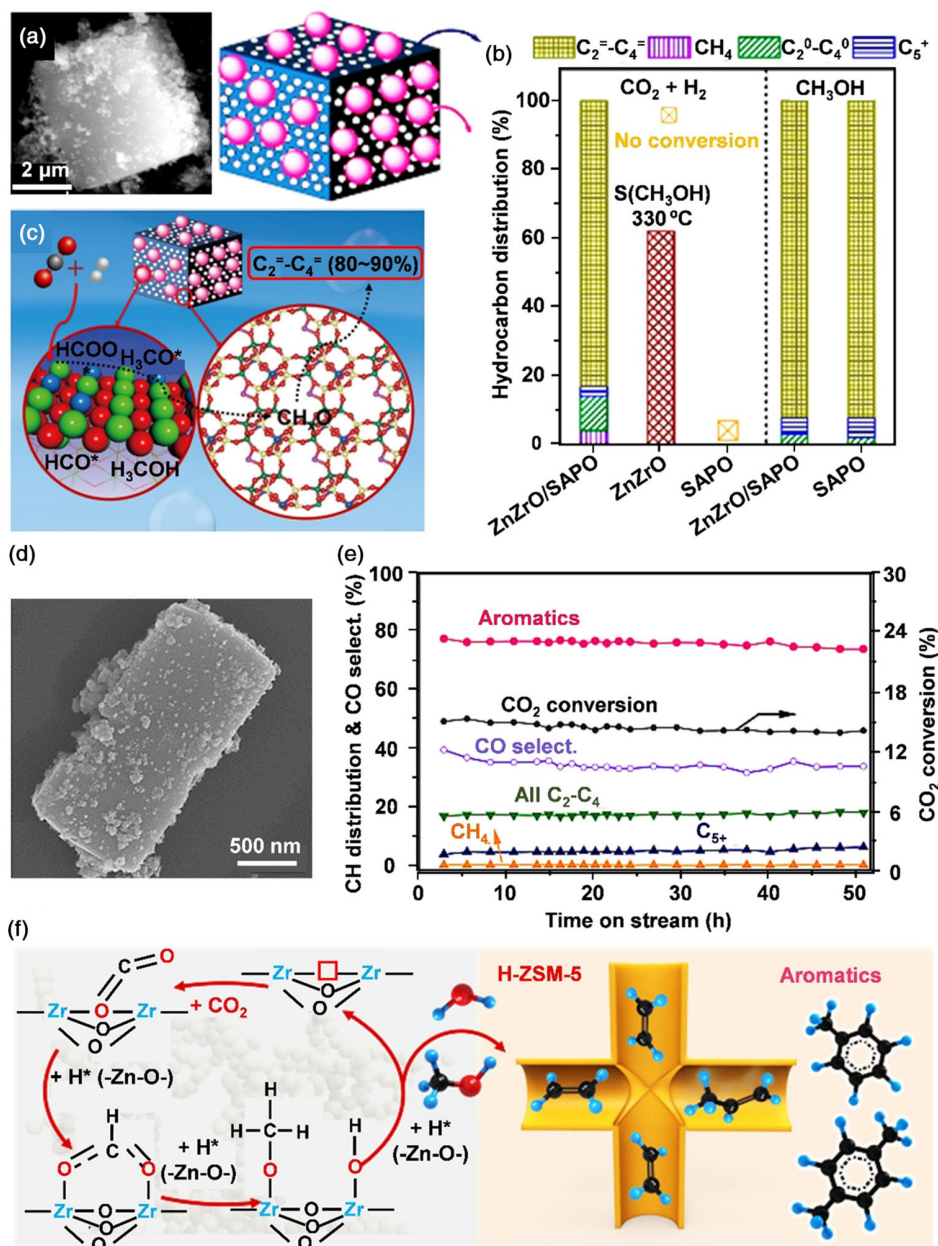
Figure 11. a) SEM image and schematic structure of ZnO–ZrO$_2$/SAPO catalyst. b) CO$_2$ hydrogenation on ZnZrO/SAPO, ZnZrO, and SAPO and MeOH conversion on ZnZrO/SAPO and SAPO. c) Illustration of the possible pathway for ZnO–ZrO$_2$/SAPO catalyst toward CO$_2$-to-olefins conversion. Reproduced with permission.[68] Copyright 2017, American Chemical Society. d) SEM images of ZnO–ZrO$_2$/H-ZSM–5 catalyst. e) Product distribution and CO$_2$ conversion of ZnO–ZrO$_2$/H-ZSM-5 catalyst in direct CO$_2$ hydrogenation. f) The possible pathway of CO$_2$ hydrogenation into aromatics over bifunctional ZnO–ZrO$_2$/H-ZSM-5 catalyst. Reproduced with permission.[75] Copyright 2019, American Chemical Society.

migration to the surface active sites; and 4) transformation of CO$_2$ into carbonaceous compounds by the photogenerated electrons when the location of CB is more negative than the redox potentials of CO$_2$ reduction half reactions. Meanwhile, the holes in the VB of semiconductors should contribute to the oxidation of H$_2$O to O$_2$ when the VB edge is more positive than the redox potential of H$_2$O/O$_2$. The H$_2$O oxidation process can be replaced by organic upgradation to value-added chemicals with a matching oxidation potential so that the CO$_2$ reduction process can be

integrated with the organic oxidations. Notably, the photocatalysts are the keys to the successful transformations and should be carefully designed as their bandgaps should be suitable to not only satisfy the large overpotentials of the abovementioned redox reactions but also broaden the utilization of solar energy. Moreover, the electronic and geometric structure of the photocatalyst should be optimized to suppress the recombination of e$^-$/h$^+$ pairs, aiming at improving the lifetimes of photogenerated carriers and quantum efficiency. Furthermore, the
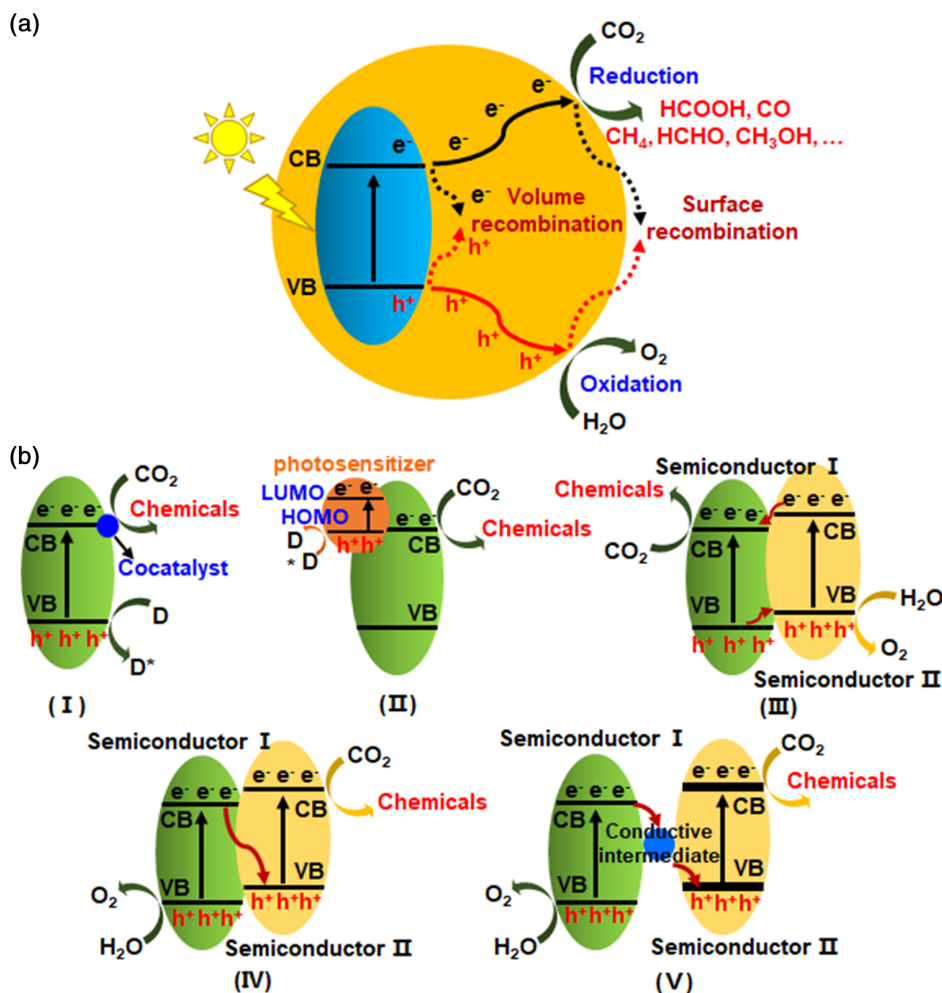
Figure 12. a) Schematic illustration of the possible mechanism and the main steps involved in the PCR system using a semiconductor photocatalyst upon illumination with efficient energy larger than the bandgaps of the semiconductor photocatalysts. b) Schematic illustration of five different systems in PCR: (1) one-step excitation semiconductor system, (2) one-step excitation photosensitized semiconductor system, (3) two-step excitation heterojunction system, (4) two-step excitation direct Z-scheme system, and (5) two-step excitation indirect Z-scheme system. Reproduced with permission.[122] Copyright 2016, American Chemical Society.

modification and reconstruction of the surface structure of the employed photocatalysts to increase the number of active sites are vital to the adsorption and activation of CO_2 molecules, which can facilitate the electrons transfer from photocatalysts to CO_2. In addition, the introduction of proper cocatalysts onto photocatalysts can provide an optimized interface to accelerate the photo-induced electron transfer rate and accumulate a large number of electrons for CO_2 reduction reaction (CO_2RR), which can effectively prolong the lifetime of e^-/h^+ pairs and improve the overall quantum efficiency. Finally, the binding energies of reaction intermediates should be optimized to facilitate the desorption of intermediate species, thus avoiding the "poison" phenomenon of photocatalysts and effectively terminating the PCR reaction for the formation of high-value-added carbonaceous products. The extensively studied PCR systems can be divided into the following five categories (Figure 12b): one-step excitation semiconductor system, one-step excitation photosensitized semiconductor system, two-step excitation heterojunction system, two-step

excitation direct Z-scheme system, and two-step excitation indirect Z-scheme system.

3.2. Plausible Systems for CO₂ Conversion

Up to now, numerous works associated with photocatalysts have been reported for CO_2 reduction, such as metal oxides (e.g., TiO_2,[78] Ga_2O_3,[79] Co_3O_4[80]), metal chalcogenides (Cu_3SnS_4),[81] metal halides ($Bi_{12}O_{17}Cl_2$),[82] bimetallic oxides (e.g., $NiCo_2O_4$,[83] $CoTiO_3$[84]), bimetallic layered double hydroxides (LDHs) (e.g., Mg, Co, Ni, Cu, Cu, and Zn-based LDH),[85a−c] and metal-free carbon-based materials (e.g., graphene oxide, g-C_3N_4).[86a,b] The catalytic activities of these photocatalysts can be optimized by the modulation of their electronic and/or geometric structures, including the design of morphology, defect, and oxygen vacancies. The CB of photocatalyst should satisfy the redox potential of CO_2 half reaction and thus thermodynamically drive CO_2 conversion into carbonaceous compounds.

**ADVANCED
SCIENCE NEWS**

www.advancedsciencenews.com

**ADVANCED
ENERGY & SUSTAINABILITY
RESEARCH**
Open Access

www.advenergysustres.com

However, their wide bandgaps and rapid recombination of photoinduced electron/hole pairs restrict their utilization of solar light and minimize the lifetime of charge carriers, as well as the photoactivity, stability, and AQY of PCR.

3.2.1. One-Step Excitation Semiconductor

One-step excitation semiconductor system is a commonly employed candidate to drive PCR with the assistance of a cocatalyst (e.g., Pd, Pt, Ag, Au, Cu, and Ni). Once the semiconductor photocatalyst absorbs solar light, the photoinduced electrons could thermodynamically flux to the cocatalyst as the Femi level of the cocatalysts situates below the CB of semiconductor, which acts as dual roles of electron "accumulation pool" and active sites for CO_2 reduction. The loading and structural optimization of cocatalysts could enrich the number and intrinsic performance of active sites, thus facilitating the activity and selectivity of PCR. For instance, Bai and co-workers hybridized TiO_2 nanosheets with Pd cocatalyst to investigate the performance of the hybrid structures toward CO_2-to-fuel conversion.[87] Note that the Pd cocatalyst with a small nanosheet structure provides abundant

edge sites for the enhancement of charge kinetics, CO, and CH_4 formation rates toward CO_2RR (**Figure 13**a–c), which adequately interpreted the edge-dependent photocatalytic performance. Meanwhile, Pd nanosheets could attract photoinduced electrons from TiO_2 to prolong the lifetime of electron−hole pairs, which effectively enhanced the stability of the overall catalytic system. Furthermore, the plasmonic effect of the Pd metal induced by visible light could generate "hot" electrons, which were then injected into the CB of TiO_2 to improve the light absorption ability of TiO_2, and thus realized the efficient CO_2 conversion under visible light irradiation. Yu's group deposited Pd cocatalyst onto the surface of graphitic carbon nitride (g-C_3N_4) and explored the facet effect of Pd toward PCR performance.[88] The Pd nanoparticles broaden the light absorption range of bare g-C_3N_4, which is mainly attributed to a localized photothermal effect of Pd. Meanwhile, the interface between Pd with g-C_3N_4 could form Schottky barriers, which effectively separated photogenerated carriers to facilitate the separation of electrons and holes. The electrons generated from the g-C_3N_4 surface could flow and accumulate on the surface of Pd nanoparticles, which were responsible for the long-term
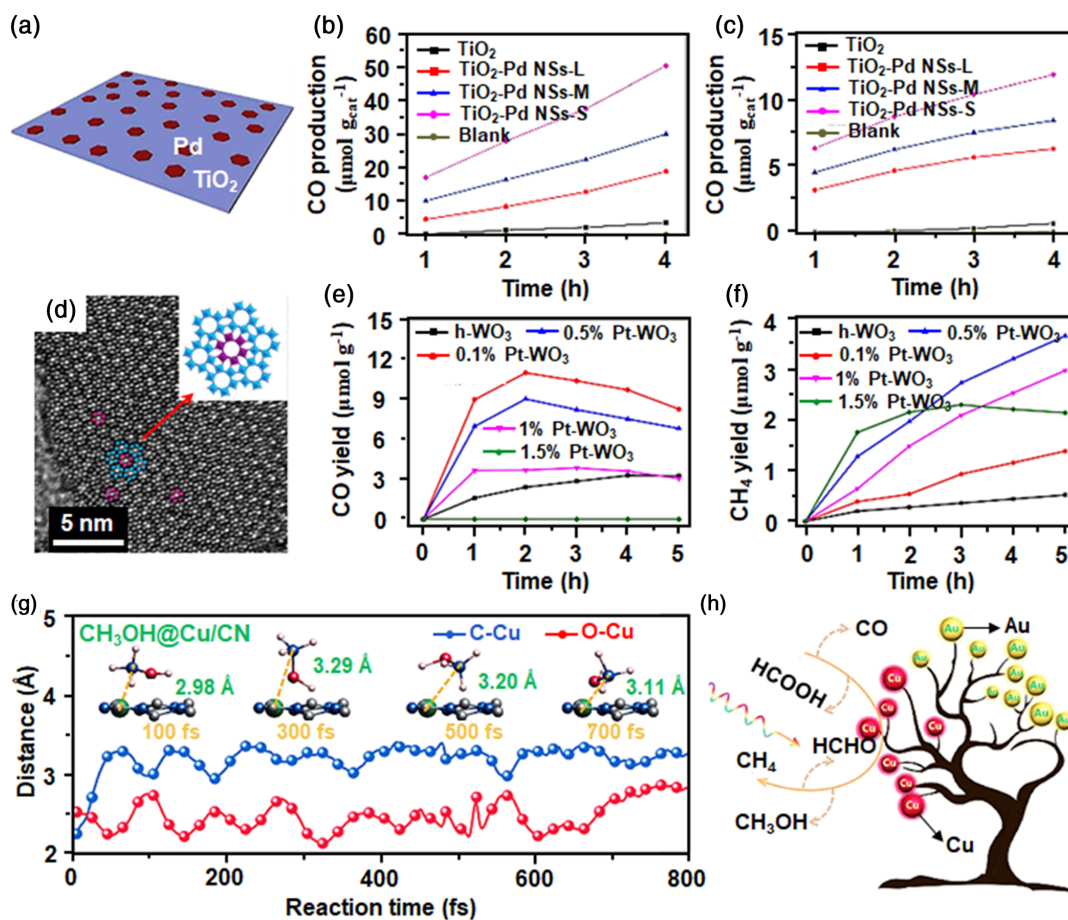

Figure 13. a) Schematic illustration of TiO_2−Pd nanosheet (NSs)−S. Time-dependent b) CO and c) CH_4 formations on TiO_2−Pd NSs−S in PCR. Reproduced with permission.[87] Copyright 2017, The Royal Society of Chemistry. d) HRTEM image of 0.5%Pt−WO_3. The e) CO and f) CH_4 production versus reaction time over 0.5%Pt−WO_3 photocatalyst. Reproduced with permission.[90] Copyright 2019, Elsevier B.V. g) The adsorption and desorption thermodynamics of $CH_3OH@Cu/CN$. h) The schematic illustration of $CH_3OH@Cu/CN$ toward CO_2-to-CH_4 conversion in PCR. Reproduced with permission.[93] Copyright 2019, The Royal Society of Chemistry.

**ADVANCED
SCIENCE NEWS**

www.advancedsciencenews.com

**ADVANCED
ENERGY & SUSTAINABILITY
RESEARCH**
Open Access

www.advenergysustres.com

CO_2 hydrogenation and the formation of CH_3OH. Moreover, the experimental results and DFT calculations verified that the optimized ratio of (111)/(100) facets of Pd could facilitate the interfacial charge carrier mobility, CO_2 adsorption ability, and CH_3OH desorption.

Metallic Pt has also been employed as a cocatalyst to improve the photoactivity of semiconductors in CO_2RR. For example, Wang and co-workers decorated Pt nanoparticles onto the surface of SiC nanosheets to study the synergistic effects for the enhancement of activity and selectivity in CO_2-to-CH_4 conversion.[89] The Pt nanoparticles as the cocatalysts could attract the photogenerated electrons from SiC, which increased the local electron densities around the active sites for the 8-electron CH_4 formation process. It should be mentioned that the generated CO intermediates could be well stabilized on Pt and were further reduced to CH_4 by the accumulated electrons on Pt "island." Similarly, Liu's group introduced different amounts of Pt on hexagonal WO_3 to enhance the mobility and lifetime of the photogenerated carriers.[90] Moreover, Pt adjusted CO adsorption ability and electronic localization, thus realizing highly selective CO and CH_4 formation in the PCR process (Figure 13d–f).

TiO_2 is the most studied material in PCR during the past decades, and the incorporation of metals such as Ag and Au has been demonstrated to be an effective approach to improve the catalytic performance of TiO_2. The particle sizes of the cocatalysts significantly influence the selectivity for CO_2 conversion. Hammad et al. reported Ag-loaded TiO_2 catalysts with different sizes of Ag nanoparticles via a photodeposition method in different atmospheres.[91] The study found that smaller Ag nanoparticles could be prepared on the surface of TiO_2 in the absence of O_2,\ and showed higher selectivity in CO_2-to-CO conversion. The main reason for the enhanced PCR lies in the fact that smaller Ag nanoparticles could efficiently collect abundant photoexcited electrons from the CB of TiO_2, which could accelerate CO_2 activation and CO desorption. Meanwhile, localized surface plasmon resonance (LSPR) of Ag nanoparticles broadened the photoabsorption range, which enhanced the utilization of solar light and photoactivity of the overall catalytic system. Au is also an ideal cocatalyst,[92] which imposes LSPR effects to broaden the sunlight absorption range to visible light regions. Moreover, the hot electrons generated from Au nanoparticles activated the adjacent electrons through energy transfer and increased local temperature, which could improve the catalytic kinetics and efficiency of PCR. Furthermore, the Schottky junction between Au and semiconductors promoted the migration of electrons from semiconductors to Au nanoparticles, which facilitated the separation of the photo-induced carriers, thus achieving long-term catalytic stability.

Except for noble metals, some non-noble metals such as Cu and Ni have also demonstrated their effectiveness as cocatalysts for the selective CO_2RR in photocatalytic systems. Li et al. deposited Cu nanoparticles on CN,[93] which realized high selectivity for CH_4 formation. Demonstrated by the kinetics and thermodynamics results, the precisely tailored Cu/CN interfaces could establish binary electron transfer channels, which contributed to $*CH_3OH$ intermediate activation and further hydrogenation reaction for the final CH_4 product formation (Figure 13g,h). Xu and co-workers prepared Ni@graphitic carbon (GC) catalyst composed of Ni nanoparticles on the surface of a few-layered

GC.[94] The presence of Ni cocatalyst could bind to GC via Ni—C bonds, which efficiently accelerated the mobility and separation of photoinduced carriers, and CO_2 adsorption, which resulted in high efficiency in PCR.

In addition, other materials like alloys,[95] metal oxides,[96] metal phosphates,[97] Mxenes,[98] graphdiyne,[99] and organics[100] have been considered as cocatalysts to improve the activity and selectivity of PCR. In general, the cocatalysts can not only accumulate electrons around them to increase local electron densities but also retard the recombination of photoexcited electron/hole pairs, thus facilitating multiple electron transfer processes for multicarbon compounds' formation and long-term stability in PCR. Meanwhile, the plasmonic effects of some metals could enhance the sunlight absorption ability, which effectively improves the AQE and solar-to-fuel efficiencies in CO_2RR.

3.2.2. One-Step Excitation Photosensitized Semiconductor

One-step excitation photosensitized semiconductor system is another alternative for PCR. Currently, the photosensitizers that served as light-harvesting roles can be classified into the following categories, such as metal complexes, organic compounds, inorganic quantum dots (QDs)/nanosheets, etc. Metal complexes for PCR were mainly based on bipyridine, and porphyrin units, among which the Ru—bipyridine complex has been the most popular choice to be used as the photosensitizer due to its good stability and suitable energy level. For example, TiO_2,[101] Co_3O_4,[102] α-Fe_2O_3,[103] NiAl-LDH (NiAl-LDH),[104] and Co_2P[105] have been used as the catalysts with the combination of $Ru(bpy)_3Cl_2 \cdot 6H_2O$ as a photosensitizer to form a hybrid photocatalyst system. The photosensitizers first adsorb incident light to generate electrons, which transfer from the highest occupied molecular orbital (HOMO) to the lowest unoccupied molecular orbital (LUMO) of photosensitizers. Subsequently, the electrons flow to the CB of semiconductors and perform a highly selective CO_2-to-fuel conversion (e.g., formic acid, CO, and CH_4). Ir(pyr) is another commonly used photosensitizer that has a strong visible light absorption band, which participates in the PCR catalyzed by a Ru-based complex to realize CO_2-to-formate conversion.[106] Non-noble metal-based photosensitizers have also attracted some attention for PCR. For example, Kang and co-workers prepared a series of Zn–porphyrins anchored on the TiO_2 surface to achieve a lower energy sensitization and increased catalytic stability.[107] The hybrid catalyst exhibited a high turnover number (TON) of $\approx$800 and a long lifetime of 90 h under red light irradiation (>550 nm) for CO_2-to-CO conversion (**Figure 14**a,b). The introduction of functional groups (e.g., acetylene, –COOH) to Zn—porphyrins could improve the energy-harvesting ability, photoinduced electron mobility, and binding capability at TiO_2. Recently, heteroleptic diamine—diphosphine Cu (Cu(dppb)) complexes were regarded as popular choices to explore their photosensitizing abilities in the PCR system. Tsubomura and co-workers found that the optimized performance would be achieved when the length of the carbon chains between the two phosphorous atoms in the diphosphine ligands is extended.[108] Using Re(bpy) as a catalyst and Cu(dppb) as a photosensitizer, a robust hybrid system was designed to realize visible light-driven CO_2 reduction to CO. The Co—quaterpyridine
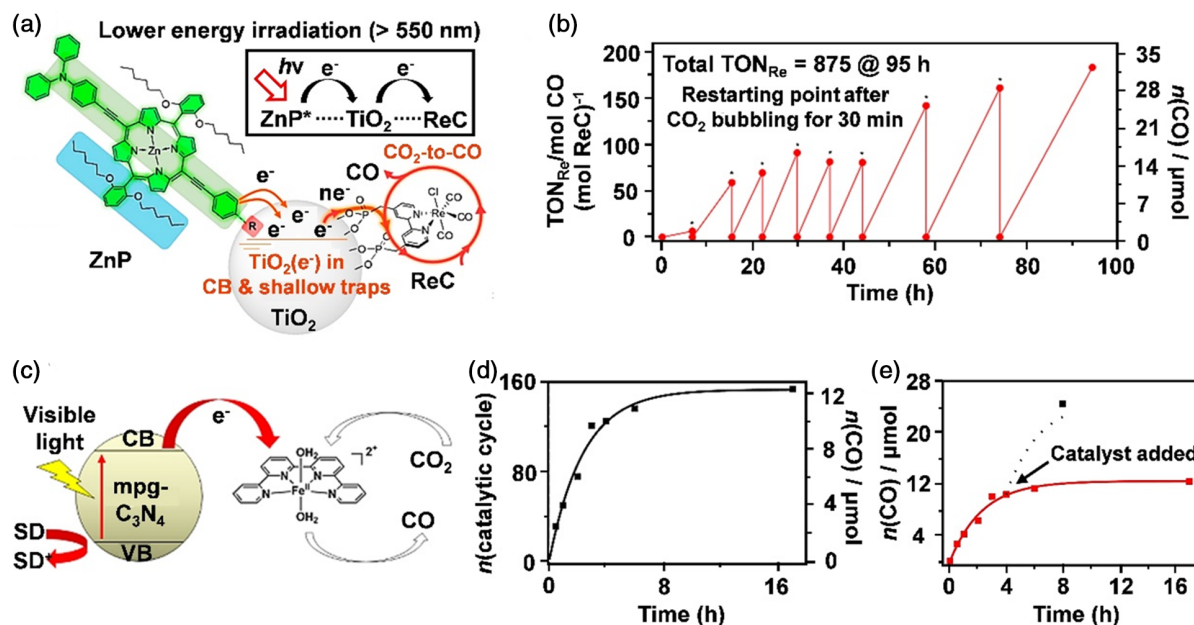
**ADVANCED
SCIENCE NEWS**
www.advancedsciencenews.com

**ADVANCED
ENERGY & SUSTAINABILITY
RESEARCH**
Open Access
www.advenergysustres.com

Figure 14. a) Schematic illustration of the possible mechanism for Zn−porphyrins−TiO₂−ReC hybrid system in PCR. b) Long-term photocatalytic CO₂-to-CO conversion of Zn−porphyrins−TiO₂−ReC hybrid system under light emitting diode (LED) lamp irradiation (>500 nm, 60 W). Reproduced with permission.[107] Copyright 2018, American Chemical Society. c) Illustration of the probable mechanism for mpg−C₃N₄/Fe−complex hybrid system toward CO₂ reduction under visible light illumination. d) CO formation versus time of mpg−C₃N₄/Fe−complex hybrids under visible light irradiation in CO₂-saturated CH₃CN/TEOA mixture. e) Stability test of C₃N₄/Fe−complex hybrids used in PCR. Reproduced with permission.[117] Copyright 2018, American Chemical Society.

molecule complex has also been regarded as a highly efficient and selective homogeneous sensitizer. Accordingly, Robert's group designed a novel molecule−material hybrid by covalently immobilizing Coqpy-Ph-COOH onto mpg-C₃N₄ through an amide linkage,[109] which exhibited high selectivity for CO production (98%) and long-term stability (no degradation after 4 days) upon a solar simulator. Finally, the same group reported a Co−quaterpyridne complex, which has been covalently attached to graphene surface by carboxylic acid groups.[110] The as-prepared catalyst was proved to be a highly active material toward visible light-driven CO₂ conversion in acetonitrile, which showed extraordinary stability (>200 h irradiation) and high selectivity of carbonaceous products (>97%). Importantly, the product selectivity could be completely controlled by varying experimental conditions: CO as the only product was achieved in phenol or trifluoroethanol (a weak acid), while formate was obtained in a mixed solution of acetonitrile and triethanolamine.

Organic dyes are another class of widely employed photosensitizers. Robert and co-workers reported that purpurin served as a simple organic photosensitizer to be used in PCR together with a molecular Fe(II) catalyst,[111] which realized highly selective CO₂-to-CO conversion (FE_CO = 95%,) under visible light illumination ($\lambda > 420$ nm) in 1/9 (v/v) CH₃CN/H₂O aqueous solution. The main absorption peak of purpurin locates at 510 nm, which is conducive to broadening the light absorption range of the PCR system. Meanwhile, the readding of purpurin to the reaction solution mixture could restore the catalytic activity and selectivity, which exhibited a TON of 120 and 95% selectivity for CO production over 4 days. Except for the organic dyes, other organic

compounds can be chosen for the application of PCR due to their visible absorption ability, good photophysical properties, and tunable redox potentials. Chao and co-workers reported an organic photosensitizer, the typical thermally activated delayed fluorescence (TADF) compound 4CzIPN,[112] for CO₂ reduction with a simple terpyridinne−Fe(III) complex catalyst under visible light irradiation. The photocatalytic system could realize an excellent selectivity for CO production of 99.3% with an enhanced TON and TOF of 2250 and 60 min⁻¹, respectively. Particularly, the TON of the PCR system containing 4CzIPN photosensitizer was around 100 times higher than ones containing [Ru(bpy)₃]²⁺. TiO₂ as an extensively used photocatalyst has been incorporated with an organic photosensitizer to realize enhanced CO₂ capture and conversion for visible light-driven PCR. For example, Liu and co-workers designed a novel four-site ionic liquid (IL)-photosensitized anatase TiO₂ catalyst to improve CO₂ conversion efficiency under visible light irradiation,[113] which exhibited the highest CO₂ absorption ability up to 3.26 mol mol_IL⁻¹ and a high rate of 3.52 μmol g⁻¹ h⁻¹ for CH₄ formation with a high FE_CH4 value above 96%. The IL could absorb CO₂ molecules and form a stable structural complex to enhance electron delocalization. Moreover, the IL has strong interaction with TiO₂ nanoparticles, which is attributed to a redshift of the light absorption edge and a synergistically broadened light absorption range to visible light regions. In this work, the IL played dual roles toward CO₂ absorption and activation. In brief, the IL-nCO₂ complex would form once the ILs bond with the CO₂ molecules and then absorb visible light, which could generate abundant photoinduced electrons. Subsequently, the electrons

could transfer from the CB of IL–nCO$_2$ to the CB of TiO$_2$ and finally launch the visible light-driven CO$_2$-to-CH$_4$ conversion over the TiO$_2$ surface.

Employing inorganic materials as photosensitizers is beneficial to experimental studies and mechanism exploration. As low-cost, stable, and nontoxic light harvesters, carbon dots can be coupled with other photocatalysts, thus exhibiting a wide spectral response in PCR. Li's group proposed carbon dots-hybridized MOF photocatalyst,[114] which exhibited enhanced activity than the pristine MOFs in CO$_2$ reduction. Carbon dots serve as excellent photosensitizers for a highly efficient PCR system under long-wavelength light irradiation, which can be ascribed to the polyaromatic units and functional groups with strong $\pi-\pi^*$ and n$-\pi^*$ transitions of carbon dots. Mn-doped semiconductor QDs reported by Son et al. showed higher photostability and broadened the absorption range of photosensitization,[115] thus activating the Ni(cyclam)-based molecular catalyst for enhanced activity and highly selective CO$_2$-to-CO conversion. This can be explained by the reason that the energetic hot electrons induced by Mn-doped QDs enable the long-range interfacial electron transfer in "nonlinked" QDs/molecular catalyst hybrids, which contributed to six times higher production amounts in CO$_2$-to-CO conversion than the pristine Ni(cyclam)$^{2+}$ system. In addition, mesoporous graphitic CN (mpg-C$_3$N$_4$) is also an ideal redox photosensitizer used in PCR due to its strong visible light response and high stability under sunlight illumination in various solvents, especially H$_2$O. For example, Cao and co-workers fabricated a polymeric CN catalyst on the surface of carbon paper via a chemical vapor deposition method.[116] The addition of phosphate realized a high selectivity of 93.8% toward CO$_2$ photoreduction to carbonaceous chemicals with an AQY of 0.4%. This study opened a new era for designing efficient photocatalysts of CO$_2$ reduction in aqueous solution, which also found that phosphate plays a key role in the CO$_2$ conversion process. Robert et al. reported a hybrid photocatalytic system containing Fe–complex catalyst and mpg-C$_3$N$_4$ photosensitizer for the first time,[117] which exhibited a high FE$_{CO}$ value of 97% and a TON of 155 with an AQY of $\approx$4.2% (Figure 14c–e). The mpg-C$_3$N$_4$ possessed enough negative CB minimum (-1.35 V vs calomel electrode (SCE)), which could reduce the Fe^I(qpy)(CO$_2$) adduct to achieve an enhanced CO formation under visible light irradiation. Halide perovskite colloidal NCs are also promising alternatives to replace the organic photosensitizers, which possess many advantages such as low nonradiative recombination rates, as well as tunable chemical composition and structures. Accordingly, Chen et al. prepared inorganic ligand-capped CsPbBr$_3$ NCs as visible light-harvesting photosensitizers, which exhibited low-cost, rich active sites, and a high molar extinction coefficient.[118] Furthermore, the [Ni(terpy)$_2$]$^{2+}$ was immobilized on the surface CsPbBr$_3$ NCs forming a hybrid catalyst, which showed a high yield of 1724 μmol g^{-1} for CO/CH$_4$ production in CO$_2$ photoreduction. The CsPbBr$_3$ NC photosensitizer offered abundant surface sites to tightly immobilize Ni-based complexes. Meanwhile, CsPbBr$_3$ NCs can broaden the light absorption range and provide a large number of photoinduced electrons to Ni-based catalytic sites for the PCR system. Some other metal-based compounds have also been applied as photosensitizers due to their strong light responses. For example, Bian and co-workers reported the use of Bi$_2$WO$_6$ particles as photosensitizers and Mn

complexes as the catalyst for the highly selective CO production toward PCR.[119] He's group proposed a promising strategy to achieve an efficient, selective, and stable PCR system,[120] in which Zn$_x$Cd$_{1-x}$S was used as the photosensitizer to couple with Fe-based molecular catalyst. The results showed that Zn$_x$Cd$_{1-x}$S facilitated charge separation and mobility, as well as visible light response. This group further combined Bi$_2$S$_3$ with CdS as a hybrid photosensitizer in another work,[121] which not only exhibited enhanced visible light absorption due to its narrow bandgap but also improved the photoinduced electron transport efficiency between the Z-scheme CdS/Bi$_2$S$_3$ photosensitizer and the Fe-based catalytic center. Thereby, the system achieved improved CO yield in CO$_2$ photoreduction. In summary, the one-step excitation (photosensitized) semiconductor system has commonly been conducted in organic solutions, which hardly exhibits satisfying photocatalytic performance, as H$_2$O is essential for the significant promotion of catalytic activity and stability. Moreover, the use of organic solvents and sacrificial reagents hinders its practical application due to its deficient environmental protection, and thus exploring the hybrid systems with the absence of organic solvent conditions and sacrificial reagents will be more promising in the PCR field.

3.2.3. Two-Step Excitation Heterojunction

Two-step excitation heterojunction system has been regarded as a coupled system of two semiconductors used in photocatalytic reactions, where semiconductors are photoexcited to generate electrons and holes on their VB and CB, respectively, and then, the photoinduced carriers would flow within the hybrid materials depending on the relative energy potentials of CBs and VBs. In terms of the band structures of the coupled semiconductors, the heterojunction system has commonly been divided into three categories: straddling gap (type I), staggered gap (type II), and broken gap (type III) (**Figure 15**).[122] In comparison, type II heterojunctions are considered the most popular choice to facilitate the separation of electron/hole pairs: the electrons would transfer to the semiconductors with a more positive CB position, while the holes flowed to the semiconductors with a more negative VB position. Accordingly, the flow directions of electrons and holes are opposite, which can significantly suppress the recombination of the photogenerated charge carriers and enhance the efficiency of the PCR system. Meanwhile, the different semiconducting components employed in heterojunctions can broaden the light absorption range due to their appropriate band structures. TiO$_2$, carbon, g-C$_3$N$_4$, and other oxides/chalcogenides/carbides/oxysalts-based materials are the most commonly applied components in type II heterostructures for highly efficient PCR. Wang and co-workers designed a paragenetic anatase/rutile TiO$_2$ heterostructure by a facile phase transformation method.[123] The two-phase TiO$_2$ heterojunction facilitated CO$_2$ absorption capacity and photoinduced carrier mobility and then activated the redox reaction of CO$_2$/CO$_2^-$, thus realizing a better selectivity for CO production when compared with P25. In addition, some low-cost materials like metal oxides or sulfides with visible light response have been applied to realize efficient charge transfer and enhanced solar energy utilization of TiO$_2$. For example, a well-connected TiO$_2$/ZnO heterojunction achieved

**ADVANCED
SCIENCE NEWS**

www.advancedsciencenews.com

**ADVANCED
ENERGY & SUSTAINABILITY
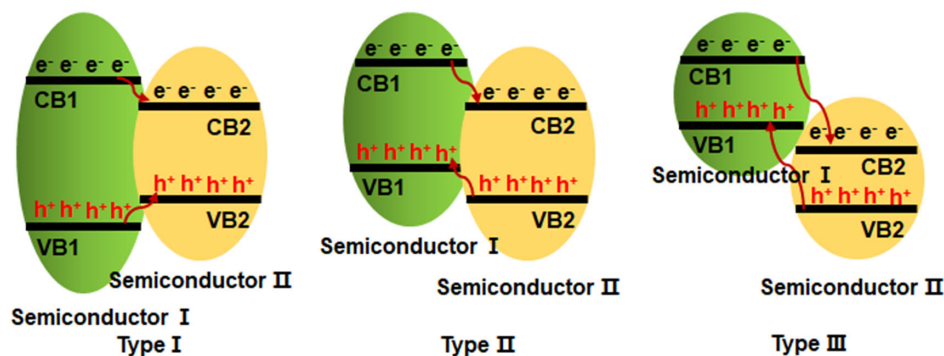RESEARCH**
Open Access

www.advenergysustres.com

Figure 15. Different types of two-step excitation heterojunction systems.

an improved photocatalytic yield of CO_2 reduction to CH_4 (2.56 $\mu mol\,g^{-1}\,h^{-1}$) than pure TiO_2 (0.55 $\mu mol\,g^{-1}\,h^{-1}$).[124] The optimal performance could be attributed to the rapid photoexcited carrier mobility and slow recombination of electron/hole pairs. Although the as-prepared heterojunctions could convert CO_2 into solar fuels, the light absorption regions still required to be broadened. Accordingly, WO_{3-x} nanowires were prepared onto the surface of mesoporous TiO_2 by Li's group, leading to a strong SPR which extended the light response range of the whole catalytic system to visible and near-infrared light.[125] Hence, the TiO_2/WO_{3-x} heterojunctions exhibited a high production rate of CH_4 (16.3 $\mu mol\,g^{-1}\,h^{-1}$) during PCR than the pristine TiO_2 (3.5 $\mu mol\,g^{-1}\,h^{-1}$) and WO_{3-x} (8.0 $\mu mol\,g^{-1}\,h^{-1}$) (**Figure 16**a,b). Within the heterojunction, TiO_2 provides continuous photoelectron injection, which plays an important role in the stable SPR of WO_{3-x}. Subsequently, the plasmonic hot electrons induced from WO_{3-x} nanowires could efficiently suppress hydrogen evolution reaction (HER) under UV−vis light irradiation, thus resulting in CH_4 formation with impressive efficiency and high selectivity (Figure 16c). Meanwhile, TiO_2 was also combined with $CaTiO_3$[126] or Cu_2ZnSnS_4[127] to fabricate heterostructure composite, which possessed an intimate contact at the interface due to their appropriate band structures and matching crystal structures. The hybrids not only enhanced the surface basicity to provide abundant active sites for improved CO_2 absorption and activation but also improved the lifetime of photogenerated carriers to achieve an efficient and selective CO_2 conversion to gaseous hydrocarbons (e.g., CO, CH_4) than pristine TiO_2. In addition, Lee and co-workers prepared a reduced form of black TiO_2 to widen the absorption region via H_2-mediated reduction step.[128] A disordered structure of TiO_2 was developed with a blueshift of the XPS peak of Ti−O, which was caused by the occupation of the oxygen vacancies by electrons. Moreover, g-C_3N_4 was introduced and wrapped with black TiO_2 to form a meta-free heterostructure. Engineering 2D/2D heterojunction photocatalysts provided a high interfacial contact area and high density of active sites, which contributed optimized physicochemical properties (e.g., charge carrier dynamics) and thus facilitated the employment of solar energy as a sustainable energy source.[129] Accordingly, the resulting g-C_3N_4/black TiO_2 showed increased light absorption at 470 nm. Moreover, the CBs and VBs of the heterojunction processed proper positions for the redox reactions of CO_2/CH_4 and $H_2O/$

O_2, respectively, thus reaching improved yields and stability for both CO and CH_4 productions than the pure black TiO_2.

C_3N_4-based heterojunctions are another class of popular alternatives used in highly efficient PCR, which facilitates photocatalytic efficiency by enhancing light absorption, charge separation, and mass transport. Li and co-workers designed 2D g-C_3N_4 nanosheets which acted as a soft template to immobilize Co_3O_4 platelets through a facile method.[130] The hybrids achieved an enhanced photocatalytic performance which was 13.5- and 2.6-fold higher than that of pure 2D g-C_3N_4 and Co_3O_4. The synergistic effects of 2D g-C_3N_4 and Co_3O_4 not only facilitate the photoinduced carrier transportation due to the large specific surface area of 2D g-C_3N_4, but also contribute to the accumulation of electrons onto the surface of g-C_3N_4 from the CB of Co_3O_4 for the absorption and reduction of CO_2- intermediate, thus improving photocatalytic properties (activity, selectivity, and stability) of the whole system under UV−vis light irradiation. As a visible light transducer, CdS shows a wide light response range and has been frequently selected as a photoharvester in photoredox reactions. For example, Wang and-coworkers improved the PCR activity of boron-doped bulk CN (BCN) semiconductors by surface engineering with CdS,[131] which exhibited 10 times higher CO_2 reduction activity than that of BCN under visible light illumination (Figure 16d,e). Due to the inner electric field of CdS/BCN heterojunctions, CdS as sensitization material could first adsorb visible light and then transferred the photoinduced electrons to the CB of BCN and finally activated and reduced CO_2 molecules to CO. The improved activity is mainly due to the improved visible light absorption and facilitated transport/separation of electron/hole pairs (Figure 16f). Interestingly, the ternary metal sulfides have also been used with g-C_3N_4 to fabricate type-II heterojunction for CO_2 photoreduction. For example, $CdIn_2S_4$,[132] or $Zn_{0.2}Cd_{0.8}S$[133] was prepared and combined with g-C_3N_4, which enhanced the CO_2 adsorption ability, charge mobility, and electron/hole pair separation efficiency and thus achieved higher photocatalytic activity and stability for the CO_2-to-CH_3OH
conversion under visible light than pristine g-C_3N_4. In addition, with the appropriate band structures, C_3N_4 could connect with Bi_4Nb_8OCl,[134] $LaPO_4$,[135] $BiFeWO_x$,[136] NiAl-LDH,[137] Mexene (e.g., Ti_3AlC_2),[138] or MOFs (e.g., Zr-based MOF, NH_2-MIL-101(Fe)).[139a−c] The charge transfer and separation phenomenon can be observed in these type-II heterostructures

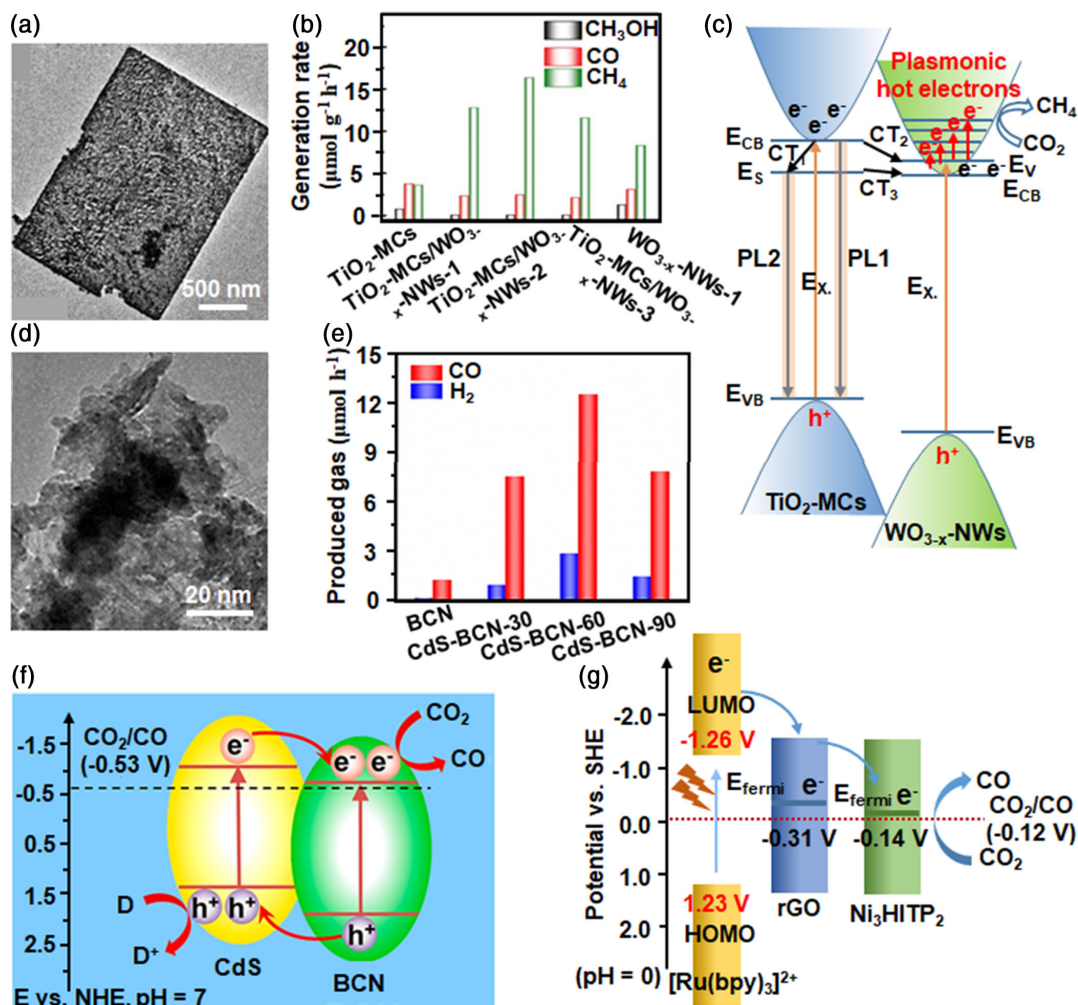**Figure 16.** a) TEM image of TiO_2/WO_{3-x} heterojunctions. b) The generation rates of CH_3OH, CO, and CH_4 of different TiO_2-based photocatalysts toward PCR. c) Possible mechanism of TiO_2/WO_{3-x} heterojunctions used in photocatalytic CO_2-to-chemicals conversion. Reproduced with permission.[125] Copyright 2019, Wiley-VCH GmbH. d) TEM image of CdS/BCN heterojunctions. e) PCR performance of different samples, including BCN, CdS/BCN-30, CdS/BCN–60, and CdS/BCN-90. f) Possible mechanism of CdS/BCN heterojunctions in PCR. Reproduced with permission.[131] Copyright 2018, American Chemical Society. g) Energy diagrams and schematic illustration of the photocatalytic mechanism of 2D/2D rGO/MOF heterojunctions for CO_2 reduction. Reproduced with permission.[143] Copyright 2019, Elsevier B.V.

through a two-step excitation process. In detail, the photogenerated electrons could escape from the CB of C_3N_4 under visible light illumination and then be transferred to the CBs of these semiconductors, while the holes induced from the VBs of these semiconductors could flow to the VB of C_3N_4, thereby launching the CO_2 reduction and water oxidation/sacrificial reagents on the CB of the additional semiconductor and VB of C_3N_4, respectively. Thanks to the synergistic effects between C_3N_4 and these semiconductors, the separation efficiency of electron/hole pairs, electron transportability and lifetime, and the light response would be improved, thus realizing the enhanced activity, selectivity, and stability of the whole PCR systems. In addition, to further advance the photocatalytic activities of C_3N_4-based heterojunctions, the defect engineering of g-C_3N_4 would play a significant role in the pristine counterpart for artificial photosynthesis,[140] which paves a new pathway of solar energy

conversion, hence turning dreams into reality to facilitate CO_2-to-fuel conversion toward a breakthrough in practical applications.

Carbon-based materials such as graphene, heteroatom-doped graphene, rGO, and carbon fibers are also employed as one of the components to construct heterojunctions for the enhanced PCR performance. As a 2D nanosheet-like material, graphene could act as an electron acceptor or transporter with a large specific surface area, which efficiently separated photogenerated charge pairs in a binary system. Ali et al. prepared a nanowire-like WSe_2/graphene composite through an ultrasonication process,[141] which could reduce CO_2 into CH_3OH when illuminated with UV−vis light. The proposed mechanism suggests that the charge carriers are first generated on the surface of WSe_2, and the photogenerated electrons transfer to the graphene nanosheets due to the high electron conductivity of the latter, thus

suppressing the recombination of the electron/hole pairs. Finally, the photoinduced electrons could reduce the adsorbed CO_2 into CH_3OH, while the holes stored on the WSe_2 were responsible for H_2O oxidization, respectively. When compared with 2D graphene, 3D-hierarchical nanostructured graphene with interconnected networks could provide larger surface areas and more active sites for photoredox reactions. Moreover, heteroatoms (e.g., N, S) were doped into graphene, which has been regarded as a promising way to modify its electronic structure and the interactions between graphene and another semiconductor. Accordingly, Liu and co-workers fabricated a 2D/3D $ZnIn_2S_4$/N-doped graphene photocatalyst by hydrothermal synthesis,[142] which showed higher CO_2 photoreduction ability. The enhanced PCR performance mainly results from the broadened light absorption range from UV to near-infrared (NIR) region, rapid charge carrier separation, and selective CO_2 uptake capacity compared with the pristine $ZnIn_2S_4$. Importantly, the photogenerated electrons could transfer from the CB of $ZnIn_2S_4$ and then accumulate onto the surface of N-doped graphene, owing to the strong electron affinity of the polar sites of N dopants, which thereby efficiently absorb CO_2 molecules and enable their reduction into products of CO, CH_4, and CH_3OH. Recently, Peng and co-workers designed a 2D/2D rGO/MOF heterojunction by cofiltering rGO nanosheets with conductive MOF nanosheets,[143] which exhibited a high CO yield rate of $3.45 \times 10^4 \, \mu mol \, g^{-1} \, h^{-1}$ and high selectivity of 91.74% for CO formation after absorbing visible light. The built-in electric field at the interface of heterojunctions improves the charge harvesting and transport, as well as CO_2 activation (Figure 16g). The abundant charges were generated on the rGO scaffold and then transferred to the conductive and intimate interface of heterojunctions. Finally, a high density of electrons was accumulated at the $Ni-N_4$ active sites in MOF, thereby achieving highly active and selective PCR. Electrospun carbon nanofiber with 1D nanostructure shows the high specific surface area, strong conductivity, and ample reaction sites and therefore is also a promising component for a heterojunction photocatalyst. For example, Dai and co-workers reported core−shell-nanostructured carbon nanofibers@TiO_2 nanoparticles composites,[144] which exhibited good intimate contact at the interface of hybrids, thus facilitating the charge transfer capacity and separation of the photoinduced electron/hole pairs. Moreover, the 1D morphology of the photocatalyst could provide more active sites for CO_2 reduction. Furthermore, the black carbon nanofibers with high conductivity could not only promote light absorption to generate heat energy for rapid diffusion of reactants and intermediates but also facilitate the separation rate of electron/hole pairs. Therefore, the system exhibited 2.3 times higher PCR activity than the pristine TiO_2, which convincingly revealed the important role of carbon nanofibers.

Other metal oxides, chalcogenides, carbides, and oxysalts-based materials such as CuO/ZnO, ZnTe/ZnO, ZnS/CdS, $BiFeWOx/In_2S_3$, MoS_2/BN, and Ti_3C_2 QDs/Mexene QDs have also been designed to form heterojunctions for efficient charge separation and transportation in PCR system. For instance, CuO and ZnO nanospheres were combined to form a hierarchical p−n heterojunction via a simple hydrothermal method.[145] The as-obtained photocatalyst facilitated the separation efficiency of photoinduced electron/hole pairs and prolonged the lifetime of electrons to realize a robust CO_2-to-CH_3OH conversion under visible light illumination. The plausible mechanism is that CuO is activated upon visible light irradiation, and electrons and holes would generate in the CB and VB of CuO, respectively. Then, the photoexcited electrons easily transferred to the CB of ZnO, which was responsible for the reduction of carbonate species into CH_3OH product. ZnTe as a typical p-type semiconductor could also connect with n-type ZnO semiconductor, forming a p−n junction due to their appropriate band structures through a facile electrochemical deposition method.[146] The resulting ZnO/ZnTe heterostructure could realize an efficient and stable CO_2 photoreduction, which maintained a $0.04 \, \mu mol \, cm^{-2}$ CH_4 yield during a consecutive 8 h test. The formation of Mott−Schottky junctions at the interface of ZnO/ZnTe facilitated the charge kinetics processes (generation and transferability). Metal chalcogenides have also been chosen as promising alternatives to be used in photocatalytic reactions due to their outstanding activity and low-cost properties. For instance, Wang and co-workers reported branch-like ZnS/CdS hierarchical heterostructures as highly efficient photocatalysts that could absorb visible light and provide high specific surface area,[147] abundant disclosed active sites for strong CO_2 absorption/capture, and accelerate the charge carrier transfer and separation ability, thus exhibiting the optimal CO formation rate of $33.3 \, \mu mol \, h^{-1}$, accompanied with high durability and reusability toward the PCR reaction. In detail, CdS first absorbed the energy of visible light and generated photoexcited electrons on its CB position, and then the electrons migrated to the CB of ZnS due to their large energy difference of the CB positions between CdS and ZnS. Finally, the electrons accumulated onto the surface of ZnS and activated CO_2RR. Hierarchical In_2S_3 with a narrow bandgap of 2.0−2.3 eV and appropriate band edges has been extensively studied as an intriguing photocatalyst. In recent work, Zhong and co-workers prepared a core@shell-structured $BiFeWO_x@In_2S_3$ by a facile hydrothermal approach.[148] The heterojunctions showed enhanced CO_2 photoconversion to CH_4 and CO than that of pure $BiFeWO_x$ and In_2S_3 under visible light illumination as the hierarchical structure improved light harvest and enriched active sites. Meanwhile, the heterojunctions could accelerate the separation efficiency and transferability of photogenerated charge carriers. 2D nanostructural MoS_2 was synthesized and incorporated with h-BN nanoplatelets to design an h-BN-MoS_2 heterostructure,[149] which presented as an effective photocatalyst for CO_2 reduction into CH_3OH under visible light irradiation. The maximum yield of CH_3OH could reach up to $5994 \, \mu mol \, g_{cat}^{-1}$, which is 3.8 times higher than that of the pure MoS_2. The increased PCR performance was caused by the effective separation of the photoinduced charge carriers at the interfaces between h-BN and MoS_2 2D/2D heterojunctions, which not only facilitated the carrier mobility for the highly active and selective CO_2 photoreduction but also improved the practicability of electrons for the enhanced reduction of CO_2 in the whole PCR system. MXenes as a new class of 2D metal carbides, nitrides, and carbonitrides have attained increasing attention in the catalytic fields due to their optimized electronic structures, rich active sites, and good chemical stability. Accordingly, Chen and co-workers fabricated hierarchical Ti_3C_2 QDs/Cu_2O nanowire heterostructures via a progressive electrostatic method to realize a highly efficient PCR.[150] The experimental results and

ADVANCED
SCIENCE NEWS
www.advancedsciencenews.com

ADVANCED
ENERGY & SUSTAINABILITY
RESEARCH
Open Access
www.advenergysustres.com

theoretical calculations demonstrated that Ti$_3$C$_2$ QDs not only improved the stability of Cu$_2$O nanowires, but also enhanced the photocatalytic activity of the heterostructures by facilitating photoexcited charge transfer/separation and light absorption ability and thus showing 8.25- and 2.15-fold higher CH$_3$OH yield than that of Cu$_2$O nanowires and Ti$_3$C$_2$ nanosheets/Cu$_2$O nanowires, respectively.

3.2.4. Two-Step Excitation Direct Z-Scheme

Two-step excitation Z-scheme systems involve two-step excitation and charge separation processes, in which the stronger reductive electrons of one photocatalyst and the stronger oxidative holes of the other one synergistically initiate the photoredox reactions. It should be noted that the main difference between Z-scheme and type-II heterostructures is the transfer directions of the photoinduced charges of the components with different CBs and VBs (Figure 12b). The Z-scheme systems can be divided into two categories, that is, direct and indirect Z-scheme systems, and the latter employs a conductive intermediate.

In a direct Z-scheme system, the electrons generated from the CB of semiconductor I can directly combine with the holes generated from the VB of semiconductor II, and then the electrons occupied on the CB of semiconductor II with stronger reducibility can react with CO$_2$ to form carbonaceous compounds, while the holes on the VB of semiconductor I with a stronger oxidizability can promote H$_2$O/O$_2$ half reaction or sacrificial reagents.

For example, α-Fe$_2$O$_3$/g-C$_3$N$_4$ hybrid acted as a hierarchical direct Z-scheme system to exhibit improved photocatalytic performance toward CO$_2$ reduction,[151] which achieved a high CO production rate of 27.2 μmol g^{-1} h^{-1} without cocatalyst and sacrificial reagent (**Figure 17**a,b). The direct Z-scheme mechanism of α-Fe$_2$O$_3$/g-C$_3$N$_4$ played in PCR is shown in Figure 17c. When these two semiconductors are in direct contact, the electrons will flow from the semiconductor with a higher Fermi level to the other one through the interface until their Fermi levels are approximately similar, thus forming a built-in electric field at the interface between α-Fe$_2$O$_3$ and g-C$_3$N$_4$. The constructed electric field could cause the depletion or accumulation of free charge carriers near the semiconductor surface. Finally, the energy band edges in the semiconductor with higher Fermi levels are bent upward toward the interface, and the energy band edges in the semiconductor with lower Fermi levels are bent downward.[152] Therefore the CBs and VBs of both components could be bent after an intimate contact between α-Fe$_2$O$_3$ and g-C$_3$N$_4$. The constructed internal static electric fields of α-Fe$_2$O$_3$ promoted the photoexcited electrons transferring onto the interface and combining with the holes in the VB of g-C$_3$N$_4$, and thus the reducibility of electrons in the CB of g-C$_3$N$_4$ and the oxidizability of holes in the VB of α-Fe$_2$O$_3$ increased. The electron spin resonance (EPR) was further conducted to validate the direct Z-scheme mechanism of α-Fe$_2$O$_3$/g-C$_3$N$_4$ played in PCR (Figure 17d,e). The spin reactive ·OH and ·O$_2^-$ species could absorb onto the surface of the photocatalyst and the
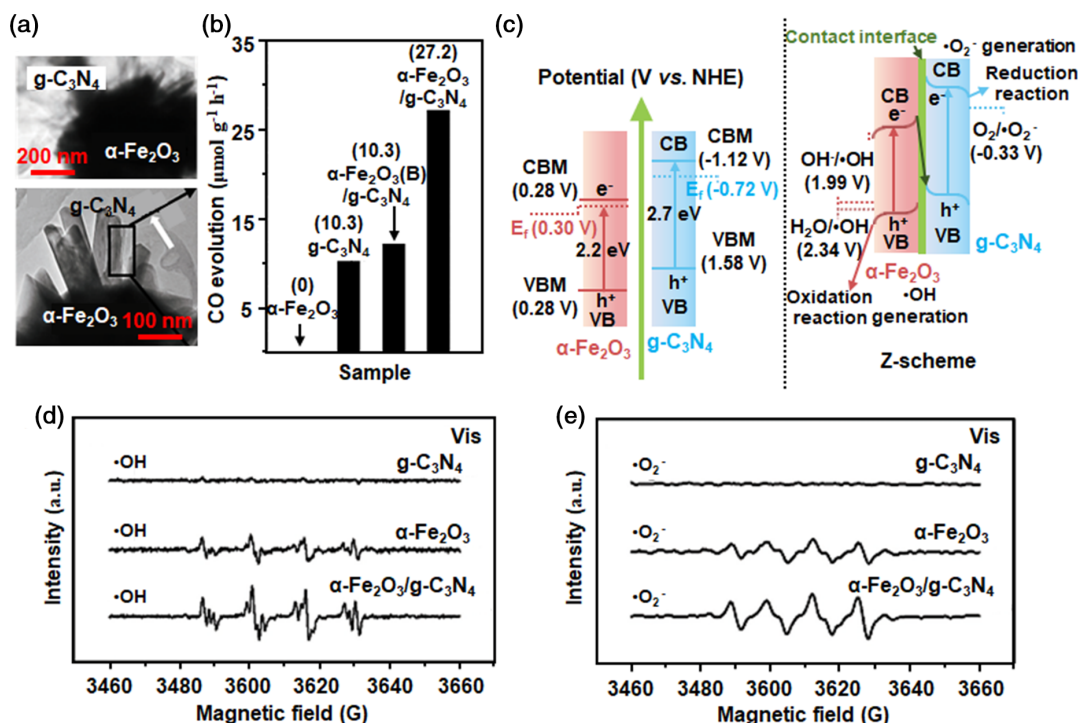
Figure 17. a) TEM images of α-Fe$_2$O$_3$/g-C$_3$N$_4$ Z-scheme system. b) The CO generation rates of different photocatalysts toward PCR. c) The band energy alignment of the direct Z-scheme photocatalytic system of α-Fe$_2$O$_3$/g-C$_3$N$_4$ hybrids before and after intimate contact between the two components. DMPO spin-trapping ESR spectra tested for d) ·OH and e) ·O$_2^-$ (e) under visible light of different photocatalysts. Reproduced with permission.[151] Copyright 2018, Wiley-VCH GmbH.

**ADVANCED
SCIENCE NEWS**

www.advancedsciencenews.com

**ADVANCED
ENERGY & SUSTAINABILITY
RESEARCH**
Open Access

www.advenergysustres.com

corresponding characteristic peaks of DMPO−OH and DMPO−O_2^- signals were detected. Meanwhile, the signals of the α-Fe_2O_3/g-C_3N_4 sample were much stronger than that of either α-Fe_2O_3 or g-C_3N_4. The results sufficiently demonstrated that α-Fe_2O_3/g-C_3N_4 hybrid followed the Z-scheme system rather than the conventional heterojunction type, which was demonstrated to exhibit an enhanced separation efficiency of electron−hole pairs than that of α-Fe_2O_3 or g-C_3N_4. Therefore, the hierarchical photocatalyst with Z-scheme construction broadens light absorption, improves the binding energy of CO_2 molecules, facilitates the separation of electron−hole pairs, and increases the reduction ability of photoinduced electrons, which synergistically enhance its performance toward PCR. Similarly, other photocatalysts like Co_3O_4,[153] WO_3,[154] MoS_2,[155] Bi_2S_3,[156] SnS_2,[157] $SnFe_2O_4$,[158] $NiMoO_4$,[159] $FeWO_4$,[160] $BiVO_4$,[161] and $Cu_2V_2O_7$[162] have also been employed to match the energy bandgap of g-C_3N_4 nanosheets, forming efficient visible light-driven Z-scheme systems for PCR. As aforementioned, g-C_3N_4-based Z-scheme photocatalysts construct a close interfacial contact between g-C_3N_4 and another semiconductor, which contributes to the improved CO_2 photoreduction into high-value-added carbonaceous compounds including CO, CH_4, CH_3OH, and HCOOH, etc. Moreover, Fei et al. provided a theoretical study for a rational-designed catalyst via element doping and Z-scheme heterojunction construction.[163] The heterojunction was composed of BiOBr and g-C_3N_4 with or without S doping, which was used for investigating the electronic effect on CO_2 reduction activity. Work function and charge density difference indicated the formation of a built-in electric field in BiOBr/g-C_3N_4 Z-scheme heterojunction, which could effectively facilitate the separation of photoinduced electron/hole pairs. Moreover, the enhanced strength of the built-in electric field was accurately analyzed by Bader charge and electric field intensity. In addition, the effect of S doping could modulate the electronic structures and thus enhance the photocatalytic performance, which was evidenced by the change in absorption coefficient. Furthermore, analyzed by the in-depth investigation of rate-determining energy, the heterojunction with S doping preferred to generate CH_3OH than CH_4, which properly explained the selectivity of CO_2-to-fuel conversion in this system. Similar to CNs, flavin has been also regarded as a metal-free and photoactive material. Savateev and co-workers reported a biomimetic core−shell structure composed of micrometer-sized flavins with potassium poly(heptazine imide),[164] which successfully converted CO_2 molecule into CO, CH_4, MeOH, and EtOH in the water vapor atmosphere. The Z-scheme heterojunction possessed an overall wide bandgap, which significantly extended its excited states lifetimes, thus facilitating the photoredox processes and suppressing the interface charge recombination.

In addition, other direct Z-scheme systems such as $ZnIn_2S_4$/TiO_2,[165,166] BiOBr/NiO,[167] Cu_2O/TiO_2,[168] rGO/TiO_2,[169] NiFe LDH/Cu_2O,[170] $BiVO_4$/Cu_2O,[171] WO_3/Cu_2O,[172] and Cu_2ZnSnS_4/ZnO[173] have been proposed to realize the enhanced activity for PCR. For example, Yu's group reported a step-scheme core−shell TiO_2@$ZnIn_2S_4$ heterojunction,[166] which exhibited much higher catalytic performance than that of pure TiO_2 or $ZnIn_2S_4$ in CO_2 photoreduction. Due to the large specific surface areas, abundant active sites, and Z-scheme structure, the catalyst showed highly efficient conversion of solar fuels

due to the improved separation of photogenerated charge carriers, which was evidenced by in situ XPS, work function calculation, and EPR measurements. The group also reported a novel Z-scheme BiOBr/NiO catalyst composed of two kinds of p-type semiconductors,[167] which could achieve enhanced CO_2 photoreduction activity than that of BiOBr or NiO. Analyzed by the in situ XPS and work function calculation, the photoinduced electrons transferred from BiOBr to NiO via a Z-scheme mechanism, which contributed to a strong redox ability and enhanced charge separation. Meanwhile, in situ DRIFT spectra revealed the formation of complex intermediates during the CO_2 photoreduction process. These results provided a new insight for the CO_2 photoreduction mechanism in Z-scheme heterojunctions constructed by p-type semiconductors. These newly developed Z-scheme photocatalytic systems realize efficient and stable CO_2 conversion into CH_4 or CO with a high yield and formation rate.

3.2.5. Two-Step Excitation Indirect Z-Scheme

Different from the direct Z-scheme system, a third component such as noble metal or graphene oxide has been incorporated as an indispensable conductive intermediate to facilitate the charge transfer and separation of electron/hole pairs in an indirect Z-scheme system. To this end, systems such as ZnO/Au/g-C_3N_4,[174] ZnCdS/Au/g−C_3N_4,[175] SnS/Au/g-C_3N_4,[176] $ZnFe_2O_4$/Ag/TiO_2,[177] Cu_2O/Ag/ZnO,[178] $AgPO_4$/Ag/CeO_2,[179] α-Fe_2O_3/amine-rGO/$CsPbBr_3$,[180] $ZnFe_2O_4$/rGO/In_2O_3, and[181] Bi_2WO_6/rGO/g−C_3N_4[182] have been constructed and investigated in PCR, where photoexcited electrons transfer from semiconductor I to conductive intermediate and then to semiconductor II, resulting in enhanced charge separation and improved redox reactions. Recently, Li et al. reported a Z-scheme ZnO/Au/g-C_3N_4 film photocatalyst with an LSPR effect for CO_2-to-CO conversion under UV−vis light illumination.[174] Verified by DFT calculations and finite-difference time domain (FDTD) method, it can be concluded that the g-C_3N_4/ZnO interface builds the electric field to facilitate carrier mobility. Meanwhile, the Au nanoparticles not only acted as a suitable conductive intermediate for the vectorial electron transfer but also as the LSPR source to promote the separation efficiency of electron−hole pairs and optical response range. Accordingly, the ZnO/Au/g-C_3N_4 photocatalyst maintained a high CO formation rate of $689.7\,\mu mol\,m^{-2}$ during a consecutive 8 h reaction time, which was significantly higher than that of pure ZnO film ($155.5\,\mu mol\,m^{-2}$). Kuang's group designed an all-solid-state Z-scheme α-Fe_2O_3/amine-rGO/$CsPbBr_3$ hybrid for highly efficient PCR (**Figure 18**a,b).[180] The photocatalyst showed a stable product (CH_4 + CO) yield of $469.16\,\mu mol\,g^{-1}$, which was 8.3 times higher than that of pristine $CsPbBr_3$ (Figure 18c). The amine-rGO could effectively regulate the interfacial interaction between $CsPbBr_3$ and α-Fe_2O_3 and then facilitate the transfer of photogenerated carriers from α-Fe_2O_3 to $CsPbBr_3$ through amine-rGO, therefore contributing to the enhanced separation of electron−hole pairs. Moreover, $CsPbBr_3$ and α-Fe_2O_3 played the roles of photocatalyst I and photocatalyst II, respectively, which showed a wide light-absorption capability and suitable reduction and oxidation potential, leading
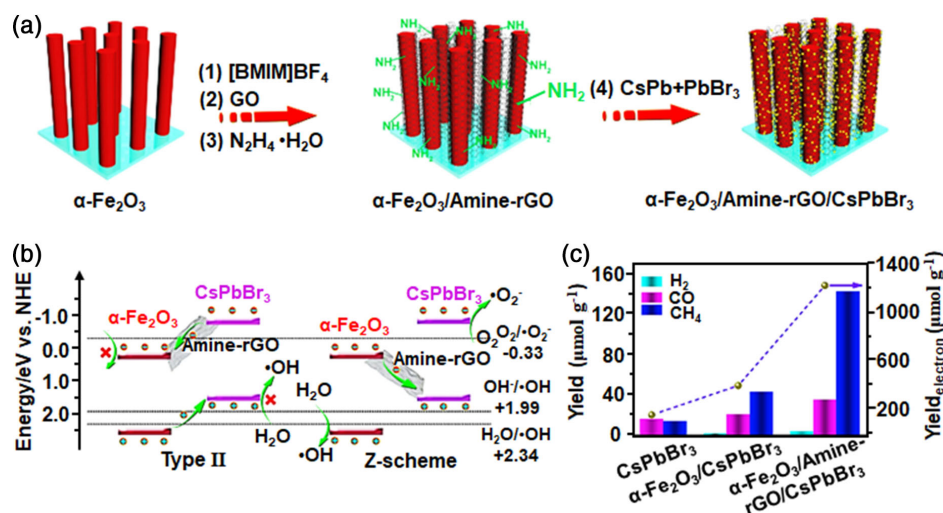
ADVANCED
SCIENCE NEWS
www.advancedsciencenews.com

ADVANCED
ENERGY & SUSTAINABILITY
RESEARCH
Open Access
www.advenergysustres.com

Figure 18. a) Schematic illustration of synthetic process of all-solid-state Z-scheme α-Fe_2O_3/amine-rGO/$CsPbBr_3$ hybrid. b) The comparison of the transfer pathways of the type II two-step excitation heterojunction (left) and the indirect Z-scheme photocatalytic system (right) of α-Fe_2O_3/amine-rGO/$CsPbBr_3$ hybrid. c) The yields toward H_2, CO, and CH_4 of $CsPbBr_3$, α-Fe_2O_3/$CsPbBr_3$, and α-Fe_2O_3/amine–rGO/$CsPbBr_3$ hybrids in the PCR. Reproduced with permission.[180] Copyright 2020, Elsevier Inc.

to an improved catalytic activity toward CO_2-to-CH_4/CO conversion with an approximately stoichiometric amount of O_2 formation. The above research work demonstrated that the indirect Z-scheme composed of ternary materials could not only facilitate the transferability of charge carriers but also widen the light response and therefore promote the development of efficient PCR into high added-value carbonaceous chemicals and fuels.

4. Photothermocatalysis

4.1. Motivation and Principles

The conventional thermocatalytic CO_2 hydrogenations require high energy consumption and system pressure, while the PCR rarely provides high-energy photons to sufficiently activate CO_2 conversion toward multicarbon chemicals and fuels production. Accordingly, the integration of these two techniques in a hybrid system is regarded as a promising route for highly efficient CO_2 reduction, which simultaneously utilizes solar energy and heat energy to initiate the reaction. When an effective catalyst (especially the sample with black color) is irradiated upon light illumination, the light energy (e.g., visible and near-infrared light) can dissipate into heat energy, which can operate the conventional thermocatalytic reactions under mild conditions. Note that the surface temperature of the catalyst can reach up to 500 °C or even higher, which offers efficient energy to conduct the thermodynamically unfavorable CO_2 reduction. The catalysts used in photothermocatalysis have been generally classified into two categories: plasmonic metals and other systems. The plasmonic metal system plays the LSPR effect, which contributes to elevated electric fields on the catalyst surface, and thereby resulted in a high density of energetic charge carriers, mainly hot electrons and holes after nonradiative decay through intraband or intraband excitations (**Figure 19**a). The photoexcited hot electrons could promote bond activation and intermediate

conversion in CO_2 reduction. In detail, the hot electrons transform the reactant molecules along an exciting potential energy surface, which contributes to extra vibration energy to the reactant, thereby activating the molecular bonds (Figure 19b). When referred to the intermediate evolution, both direct and indirect routes play critical roles in optimizing the reaction selectivity and activity (Figure 19c,d).[9] Other systems without LSPR effects could also perform efficient activities in photothermocatalysis, mainly depending on the structural optimization of the catalysts. However, the mechanism of photothermocatalysis is complex due to unknown thermodynamics and kinetics, and the synergy between the photocatalytic and thermal effects remains unexplored. In general, the newly developed photothermocatalysis could overcome the difficulties of inferior activity in photocatalysis and excess reaction barriers in thermocatalysis, with abundant solar energy under lower temperatures and pressures.

4.2. Plausible Routes for CO_2 Hydrogenation

The primary reactions evolved in photothermocatalysis can be broadly classified into five groups: 1) RWGS reaction, 2) methanol and ethanol synthesis, 3) methanation reaction, and 4) CO_2 hydrogenation. Some aspects are similar to thermocatalysis, which have been reviewed in **Section 2.1**.

4.2.1. CO_2 to CO

1. In the thermocatalytic RWGS reaction, some transition metals and metal oxides have been studied to produce CO via CO_2 hydrogenation under certain temperatures and pressures. It should be noted that the photothermocatalytic RWGS reaction concentrates on nanostructured materials, which exhibited distinguished catalytic performance. For example, Ozin and coworkers designed a black indium oxide catalyst via hydrogenating In_2O_3 NC,[183] thus forming amorphous domains of In_2O_{3-x} on
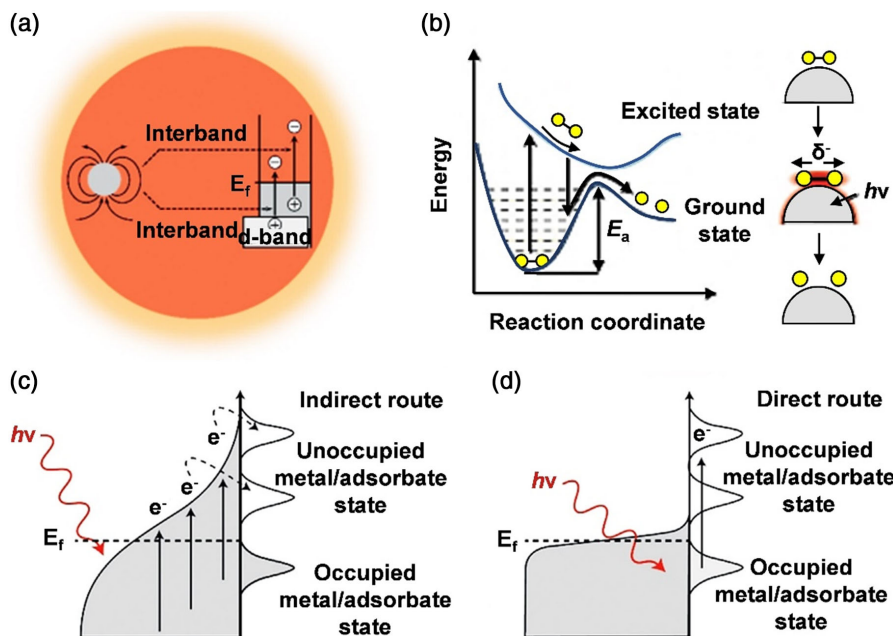
Figure 19. a) The illustration of hot carriers generated through nonradiative decay that resulted from the LSPR effects. b) Bond activation over plasmonic metals. Immediate conversion after absorbing the plasmon energy from the metal in an c) indirect and d) direct route, respectively. Reproduced with permission.[9] Copyright 2019, Wiley-VCH GmbH.
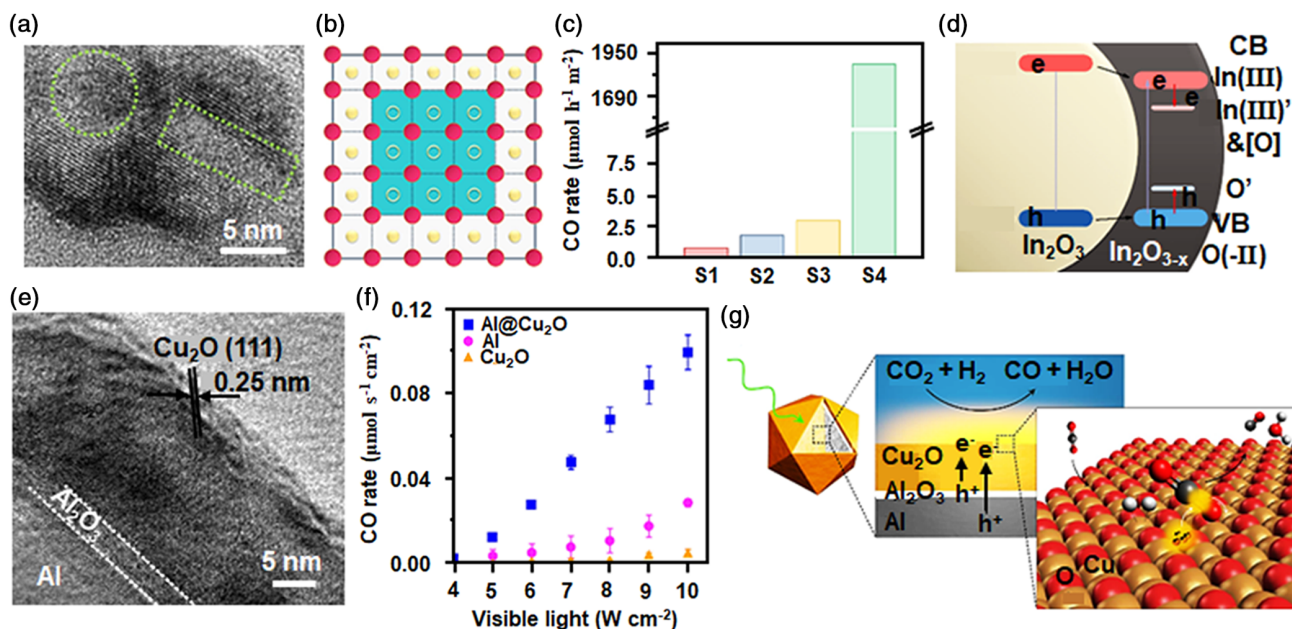

Figure 20. a) HRTEM image of the nonstoichiometric In_2O_{3-x} after annealing stoichiometric In_2O_3 NC at 400 °C under N_2 and H_2 atmosphere for 20 min. b) Illustration of the treated In_2O_3. Pink dots, yellow dots, yellow circles, and blue regions represent In atoms, O atoms, oxygen vacancies, and amorphous phase, respectively. c) The performance of In_2O_{3-x}/In_2O_3 prepared by different treated times in photothermocatalytic CO_2 hydrogenation in a batch reactor. S1 indicates the as-prepared In_2O_3 NC. S2, S3, and S4 are obtained by annealing pristine S1 under H_2 atmosphere at different temperatures (i.e., 200, 300, and 400 °C) for 1 h to form In_2O_{3-x}/In_2O_3 with different x values. d) Schematic illustration of the electronic band structure of In_2O_{3-x}/In_2O_3 heterojunction under light illumination. Reproduced with permission.[183] Copyright 2020, Springer Nature. e) HRTEM image of $Al/Al_2O_3/Cu_2O$ heterostructure. f) The CO production rates of $Al/Al_2O_3/Cu_2O$ versus visible light intensity in photothermocatalytic RWGS reaction. g) Schematic mechanism of plasmon-driven RWGS reaction using $Al/Al_2O_3/Cu_2O$ heterostructures. Reproduced with permission.[185] Copyright 2017, Springer Nature.

**ADVANCED
SCIENCE NEWS**

www.advancedsciencenews.com

**ADVANCED
ENERGY & SUSTAINABILITY
RESEARCH**
Open Access

www.advenergysustres.com

crystalline In_2O_3 (**Figure 20**a,b). The constructed nonstoichiometric/stoichiometric In_2O_{3-x}/In_2O_3 heterojunction enabled high activity for RWGS reaction with 100% selectivity toward CO formation, which achieved an extremely high CO production rate of 1874.62 $\mu mol\,h^{-1}\,m^{-2}$ (23882.75 $\mu mol\,g^{-1}\,h^{-1}$) (Figure 20c), three orders of magnitude higher than pale yellow In_2O_3 (19.64 $\mu mol\,g^{-1}\,h^{-1}$) under 100 W LED white lamp. The significantly enhanced performance could be ascribed to the synergistic roles of stronger sunlight absorption ability and photothermal effects. The oxygen vacancies in In_2O_{3-x} promoted the insertion of protons to weaken the C—O bonds of the CO_2 reactant, which facilitated the CO formation (Figure 20d). Meanwhile, the In_2O_{3-x}/In_2O_3 heterostructure enhanced the light absorption across the solar spectrum, which gave rise to local heating on the surface of the catalyst and then contributed to the thermocatalytic conversion of the RWGS reaction. Moreover, the heterostructure could effectively separate photoinduced electron—hole pairs, which also contributed to the enhanced PCR performance. Therefore, the surface black In_2O_{3-x} layer acted as promising material to perform an improved activity in photothermal RWGS reactions. Recently, Ozin and Zhang and co-workers reported a supraphotothermal Ni@p-SiO₂ catalyst, which exhibited a satisfying catalytic activity and stability toward RWGS and methanation reactions due to the spatial confinement effects, heat insulation, and infrared shielding effects of catalysts.[184] Halas and co-workers reported the synthesis of $Al/Al_2O_3/Cu_2O$ heterostructures (Figure 20e),[185] which exhibited highly efficient and selective RWGS activity under light irradiation at room temperature than that in thermal conditions (Figure 20f). To investigate the spatial temperature, light absorption ability, and integrated electric field of the heterostructural catalyst, the work demonstrated that the LSPR effect of $Al@Cu_2O$ antenna reactors could provide abundant hot carriers and broaden the light absorption range of Cu_2O under visible light illumination, thereby achieving highly selective CO production in CO_2 conversion. $Al@Cu_2O$ acted as the active component exhibiting plasmon-enhanced CO_2 conversion, which was accompanied by heat generation from the thermalization of the hot carriers, thus resulting in an enhanced photothermocatalytic process (Figure 20g). The local temperature of $Al/Al_2O_3/Cu_2O$ surface could reach up to 175 °C under visible light irradiation due to the photothermal heating from electron—electron scattering during the hot-carrier decay. The photoinduced hot carriers fluxed from Al core to Cu_2O shell, which played the main role in C—O bond dissociation and prolonged the lifetime of excited states. Accordingly, the $Al@Cu_2O$ antenna reactor mechanism was proposed, which achieved higher activity and selectivity in the RWGS reaction than the traditional thermocatalysis, and thus showed an optimal CO formation rate of ≈360 $\mu mol_{CO}\,cm^{-2}\,s^{-1}$ during the light-excited process (10 W cm⁻²). Other catalysts have also been reported for efficient CO_2 photothermocatalysis, such as $TiN@TiO_2@In_2O_{3-x}(OH)_y$,[186,187] 2D In_2O_{3-x},[188] Cu hydroxyapatite,[189] W-doped TiO_2,[190] Pd/TiO_2,[191] $FeO—CeO_2$,[192] MoO_{3-x},[193] $Bi_4TaO_8Cl/W_{18}O_{49}$,[194] Bi_2S_3/UiO-66,[195] Co@CoN&C,[196] $Ni_{12}P_5$,[197] and Pd nanoparticle (NPs)/barium titanate,[198] which reached satisfying CO formation rates upon solar light illumination.

4.2.2. CO_2 to Alcohols

In comparison with photothermocatalytic RWGS reaction, studies on methanol and ethanol synthesis are quite limited. Hong and co-workers designed a Pd/ZnO catalyst through a facial impregnation approach to realize industrial MeOH formation at relatively low pressure (12 bar) under light irradiation.[199] The enhanced MeOH yield was due to the synergy effect between photocatalysis and thermocatalysis, as well as a wide visible light absorption range induced by the LSPR effect of Pd nanoparticles (**Figure 21**a–c). The latter was confirmed to be the main contributor (>90%) to the enhanced photothermocatalytic MeOH formation. The interface of Pd—ZnO would accept the abundant hot electrons and acted as the active site to promote CO_2 absorption and activation via electron injection to the antibonding orbital of CO_2 molecules, thus resulting in MeOH synthesis in a similar way to thermocatalytic CO_2 hydrogenation. Therefore, Pd/ZnO achieved a promotion of CO_2 conversion efficiency more than two times and enhanced yield of MeOH (1.5–3.0 times) under light irradiation in a flow fixed-bed plasmon-assisted photothermal reactor under relatively lower pressure. Some other catalysts including Cu^0/Cu_2O,[200] CoO/Co/TiO_2,[201] and $LaCo_xFe_{1-x}O_3$[202] have been reported to achieve efficient MeOH synthesis through plasmon-assisted photothermocatalysis or photo—thermo coupling conditions (**Table 1**). For example, Cui's group fabricated a complex composed of AuCu alloy nanoparticles and ultrathin porous g-C₃N₄ nanosheets (Figure 21d),[203] and the integrated photocatalysis and thermocatalysis synergistically realized an enhanced yield (0.89 mmol g⁻¹ h⁻¹) and selectivity (93.1%) of ethanol formation at 120 °C under visible light irradiation using 1.0 wt% AuCu/g-C₃N₄ composites (Figure 21e). The positive charges on Au surface facilitated CO_2 adsorption, while Cu with enriched negative charges improved the *CO_2^- and *CO intermediate generation. Meanwhile, the strong interaction between AuCu alloy and g-C₃N₄ promoted photoinduced carrier transportation. Moreover, the increased temperature on the surface of the catalyst accelerated the dynamics and thermodynamics of reactant molecules, which resulted in the enhanced *CO dimerization and C—C coupling reactions (Figure 21f). Accordingly, the AuCu/g-C₃N₄ catalyst exhibited 4.2- and 7.6-fold higher yield toward photothermocatalytic ethanol synthesis than that in photocatalytic and thermocatalytic processes, respectively.

4.2.3. CO_2 to CH_4

Methanation reaction is known as the Sabatier reaction, which can produce CH_4 via CO_2 hydrogenation. Ru- and Ni-based materials have been the most frequently used catalysts for CO_2 methanation to realize the satisfying CH_4 yield and selectivity. Ye's group constructed a hybrid catalyst with small Ru nanoparticles supported on ultrathin Mg—Al few-layer LDHs (Mg—Al FL-LDH) supports (**Figure 22**a,b),[204] which could reach a peak rate of CH_4 formation (277 mmol g⁻¹ h⁻¹) in a flow-type reactor (Figure 22c, d). The Ru nanoparticles played vital roles in H_2 activation and the subsequent CO_2 hydrogenation as metallic Ru could enhance the local temperature of the Ru@FL-LDHs surface after absorbing solar light. Meanwhile, ultrathin Mg—Al LDH possessed
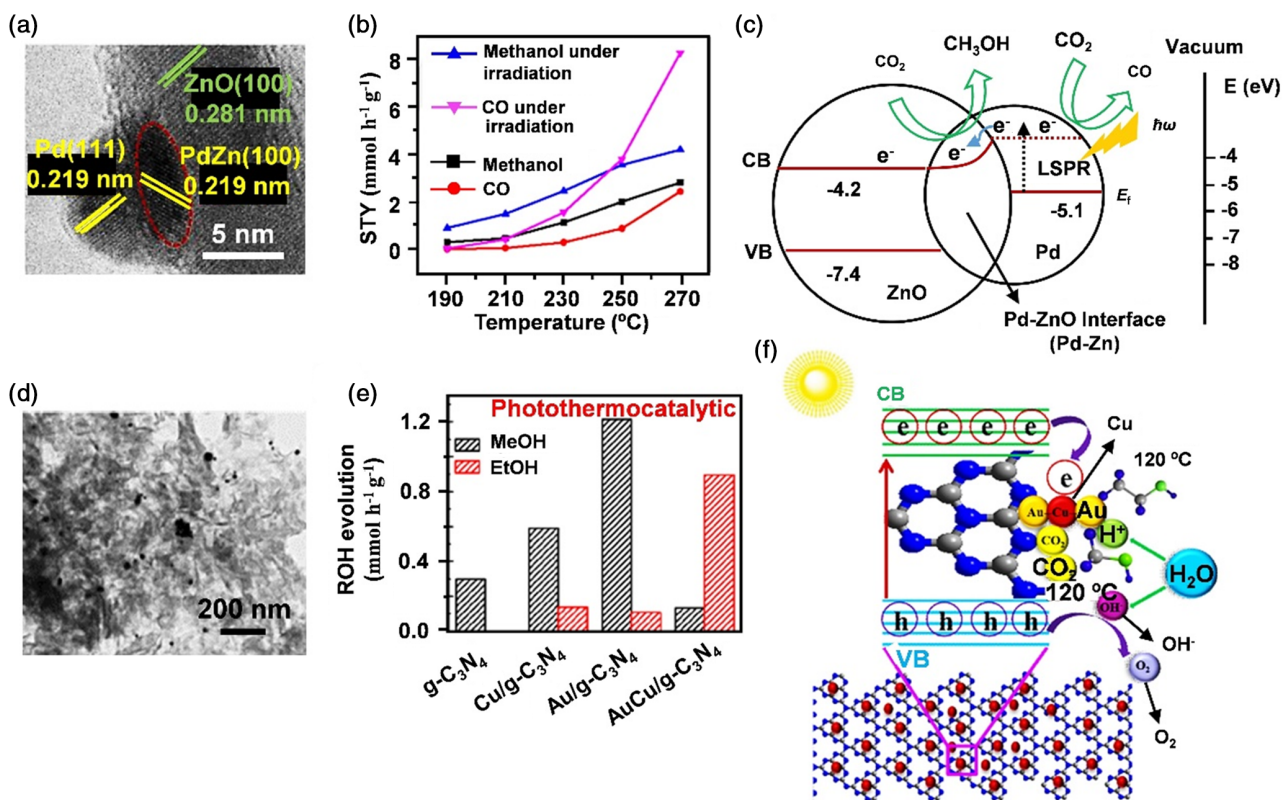
Figure 21. a) HRTEM image of Pd/ZnO catalyst. b) The STY toward different products over Pd/ZnO catalyst in photothermo CO_2 hydrogenation under different reaction temperatures with or without light irradiation. c) The reaction mechanism of Pd/ZnO catalyst in SPR-mediated CO_2-to-MeOH conversion. Reproduced with permission.[199] Copyright 2019, Wiley-VCH GmbH. d) TEM and HRTEM images of AuCu/g-C_3N_4 composites. e) Photothermocatalytic CO_2 reduction over different catalysts under light irradiation at 120 °C. f) Schematic mechanism of AuCu/g-C_3N_4 composites in photothermocatalytic CO_2-to-ethanol conversion. Reproduced with permission.[203] Copyright 2020, Elsevier B.V.

abundant active sites, which benefited the CO_2 activation and reactant absorption. A series of control experiments had been conducted to reveal the mechanism of photothermocatalytic processes in this work. Light illumination is regarded as a driving force to initiate the photo-to-thermal conversion, while photocatalysis played a negligible role in CH_4 production. In other words, the photothermal reaction is quite similar to that in the traditional thermocatalysis, where Ru@FL-LDHs reached a high reaction temperature of ≈350 °C under continuous irradiation to activate H_2 molecules. Moreover, the close intact nature between Ru nanoparticles and FL-LDHs certainly contributed to the highly efficient CO_2 hydrogenation process. Therefore, Ru@FL-LDHs performed an efficient and stable methanation reaction toward CO_2 photothermocatalysis under mild reaction conditions. In addition to Ru, Ni as an abundant and low-cost material has been employed as an active catalyst for photothermocatalytic CO_2 methanation. Accordingly, Li et al. realized satisfying CO_2 methanation performance by developing a new photothermal reactor with the presence of a layer of absorber (Figure 22e).[205] Under solar light illumination (from 0.52 to 0.7 kW m^{-2}), the catalyst that was composed of single Ni atoms, and ultrathin amorphous Y_2O_3 nanosheets (the SA Ni/Y_2O_3 nanosheets) (Figure 22f) showed an optimal CH_4 formation yield up to 7.5 L m^{-2} h^{-1} with a high CO_2 conversion efficiency of 80%

under elevated temperature (Figure 22g,h). The rational design of single-atom Ni coupled with the selective light absorber (here ultrathin amorphous Y_2O_3 nanosheets) could realize a high and stable photothermocatalytic methanation reaction under solar light irradiation at a relatively lower initial reaction temperature using SA Ni/Y_2O_3 composites.

The Co species also exhibits a high photothermo effect in CO_2 methanation as it can absorb the solar light and then convert it to thermal energy via the intra- and interband electron transition. It means that photoexcited electrons could recombine with the holes to generate phonons rather than photons, which increases the local temperature on the surface of Co-based catalysts and thereby performs good activity in photothermocatalytic CO_2 methanation under solar light irradiation. Herein, Jia's group fabricated highly dispersed Co nanoparticles on Al_2O_3 support (**Figure 23**a),[206] which achieved an extraordinary CH_4 formation rate of 6036 µmol g^{-1} h^{-1} with high CH_4 selectivity of 97.7% during continuously catalytic testing (Figure 23b,c). The broad optical response range, the strong adsorption ability toward reactant molecules, and the large density of active sites synergistically contributed to the enhanced photothermocatalytic performance of Co/Al_2O_3. Moreover, the UV−vis light irradiation promoted the formation of oxygen vacancies on the surface of Co/Al_2O_3, which improved the absorption ability of CO_2 molecules,

Table 1. Performance comparisons of the representative catalysts used in photothermocatalytic CO_2 hydrogenation under light irradiation.[183,185–197,199–218]

Catalyst	Light source	Temperature[a]	Production rate	Ref.
RWGS reaction (product: CO)				
In_2O_{3-x}/In_2O_3	100 W LED white lamp	300 °C	1874.62 µmol h^{-1} m^{-2}	[183]
$Al/Al_2O_3/Cu_2O$	White light, 10 W cm^{-2}	175 °C	360 $µmol_{CO}$ cm^{-2} s^{-1}	[185]
$TiN@TiO_2@In_2O_{3-x}(OH)_y$	Xe lamp	150 °C	5.35 µmol cm^{-2} h^{-1}	[186]
$TiN@TiO_2@In_2O_{3-x}(OH)_y$	Xe lamp, 1.6 W cm^{-2}	225 °C	3439.9 µmol g_{In}^{-1} h^{-1}	[187]
2D In_2O_{3-x}	300 W Xe lamp	370 °C	103.2 mmol g_{cat}^{-1} h^{-1}	[188]
Cu hydroxyapatite	40 sun	—[b]	12 $mmol_{CO}$ g_{cat}^{-1} h^{-1}	[189]
4%W-doped TiO_2	UV light	120 °C	0.056 µmol g^{-1} h^{-1}	[190]
1.0 wt% Pd/TiO_2	500 W Mercury light, >254 nm	500 °C	11.05 µmol g^{-1} h^{-1}	[191]
$FeO–CeO_2$	Xe lamp, 2.2 W cm^{-2}	—	19.61 mmol g_{cat}^{-1} h^{-1}	[192]
MoO_{3-x}	UV–vis–IR light	160 °C	10.3 µmol g^{-1} h^{-1}	[193]
$Bi_4TaO_8Cl/W_{18}O_{49}$	Solar light, 180 mW cm^{-2}	120 °C	23.42 µmol g^{-1} h^{-1}	[194]
$1.9\%Bi_2S_3/UiO-66$	Solar light 650 mW cm^{-2}	150 °C	25.60 µmol g^{-1} h^{-1}	[195]
Co@CoN&C	300 W Xe lamp	518 °C	132 mmol g_{cat}^{-1} h^{-1}	[196]
$Ni_{12}P_5$	Xe lamp 2.3 W cm^{-2}	—	≈960 mmol g_{cat}^{-1} h^{-1}	[197]
Alcohol synthesis (products: MeOH and EtOH)				
Pd/ZnO	500 W Mercury light	270 °C	MeOH: ≈4.5 mmol g^{-1} h^{-1}	[199]
Cu^0/Cu_2O	300 W Xe lamp, $\lambda > 400$ nm	110 °C	MeOH: 2.6 µmol g^{-1} h^{-1}	[200]
$CoO/Co/TiO_2$	300 W Xe lamp	120 °C	MeOH: 39.6 µmol g_{cat}^{-1} h^{-1}	[201]
$LaCo_xFe_{1-x}O_3$	300 W Xe lamp, $\lambda > 420$ nm	350 °C	MeOH: 2.3 µmol g^{-1} h^{-1}	[202]
$AuCu/g-C_3N_4$	300 W Xe lamp, $\lambda > 420$ nm	120 °C	EtOH: 895 µmol g^{-1} h^{-1}	[203]
Methanation reaction (product: CH_4)				
Ru@FL-LDHs	300 W Xe lamp, 10 Suns	350 °C	277 mmol g^{-1} h^{-1}	[204]
Single Ni atom/Y_2O_3	Solar irradiation, 1 kW m^{-2}	288 °C	7.5 L m^{-2} h^{-1}	[205]
$21\%Co/Al_2O_3$	UV–vis–IR light, 1300 mW cm^{-2}	292 °C	6036 µmol g^{-1} h^{-1}	[206]
Amorphous boron	300 W Xe lamp	378 °C	2.5 µmol h^{-1}	[207]
TiO_2 PCs	300 W Xe lamp	2 °C	35.0 µmol g^{-1} h^{-1}	[208]
Ru/i–Si–o	300 W Xe lamp, 2470 mW cm^{-2}	150 °C	2.8 mmol g^{-1} h^{-1}	[209]
Ni NPs/$BaTiO_3$	300 W Xe lamp, 293 mW cm^{-2}	≈335 °C	103.7 mmol g^{-1} h^{-1}	[210]
Ni/80Ce-20Ti_SG	300 W Xe lamp	>200 °C	17.0 mmol g_{cat}^{-1} h^{-1}	[211]
TiO_2 NPs/Graphene	300 W Xe lamp, 4.38 kW m^{-2}	116.4 °C	26.7 µmol g^{-1} h^{-1}	[212]
TiO_{2-x}/CoO_x	150 W UV lamp	120 °C	≈10 µmol g^{-1} h^{-1}	[213]
C2 + hydrocarbons synthesis				
Fe-500	300 W Xe lamp, 1.88 W cm^{-2}	252–312 °C	CH_4: 47.1%	[214]
			C_{2+}: 46.6%	
θ-Fe_3C	300 W Xe lamp, 2.05 W cm^{-2}	310 °C	CH_x: 10.9 mmol g^{-1} h^{-1}	[215]
Fe_2O_3/Fe_3O_4	Highly concentrated sunlight (concentrating ratio: 600)	500 °C	CH_4: 1470.7 µmol g_{cat}^{-1} h^{-1}	[216]
			C_2H_4: 736.2 µmol g_{cat}^{-1} h^{-1}	
			C_2H_6: 277.2 µmol g_{cat}^{-1} h^{-1}	
Na/Co@C	1000 W Xe lamp, AM 1.5 filter	235 °C	CH_4: 50.2%	[217]
			C_2: 13.0%	
			C_3: 12.7%	
			C_4: 5.2%	
			C_5: 3.3%	
			C_6: 2.0%	

**ADVANCED
SCIENCE NEWS**

www.advancedsciencenews.com

**ADVANCED
ENERGY & SUSTAINABILITY
RESEARCH**
Open Access

www.advenergysustres.com

Table 1. Continued.

Catalyst	Light source	Temperature[a]	Production rate	Ref.
Ni-doped $BaZr_{0.5}Ce_{0.3}Y_{0.2}O_{3-\delta}$	UV light	350 °C	CH_4: 219.9 µmol g^{-1}	[218]
			C_2H_6: 83.24 µmol g^{-1}	
			C_3H_8: 12.7 µmol g^{-1}	
Co-doped $BaZr_{0.5}Ce_{0.3}Y_{0.2}O_{3-\delta}$	UV light	350 °C	CH_4: 266.8 µmol g^{-1}	
			C_2H_6: 123.2 µmol g^{-1}	
			C_3H_8: 21.27 µmol g^{-1}	

[a]The equilibrium temperature values of the samples under focused light irradiation; [b]"−" indicates not noted.
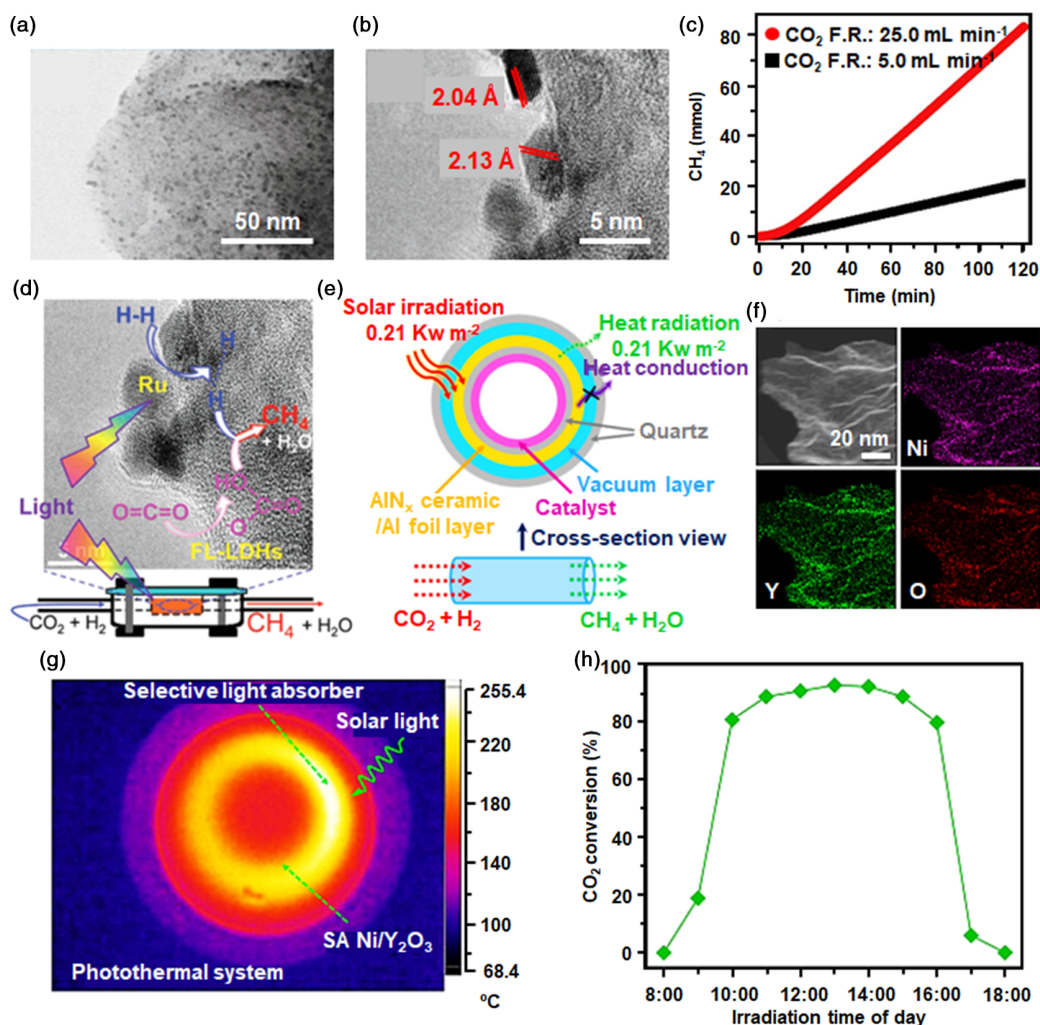

Figure 22. a,b) TEM and HRTEM images of Ru@FL-LDHs catalyst. c) The CH_4 yield over Ru@FL-LDHs catalyst under 300 W Xenon lamp irradiation (light intensity, 10 Suns) at H_2/CO_2 flow rates of 25.0 and 5.0 mL min^{-1}, respectively. d) Schematic illustration of photothermocatalytic CO_2 hydrogenation processes over Ru@FL-LDHs catalyst in a flow reactor. Reproduced with permission.[204] Copyright 2017, Wiley-VCH GmbH. e) Schematic illustration of the newly developed photothermocatalytic reactor system for CO_2 methanation with the selective absorber and the SA Ni/Y_2O_3 nanosheets. f) STEM image and the corresponding EDS mapping images of Ni, Y, and O of the SA Ni/Y_2O_3 nanosheets. g) The spatial temperature mapping of the newly developed photothermocatalytic system under simulated solar light illumination using an infrared camera (intensity: 1.0 kW m^{-2}). h) The performance of the SA Ni/Y_2O_3 nanosheets catalyzed in photothermocatalytic CO_2 hydrogenation. Reproduced with permission.[205] Copyright 2019, Springer Nature.
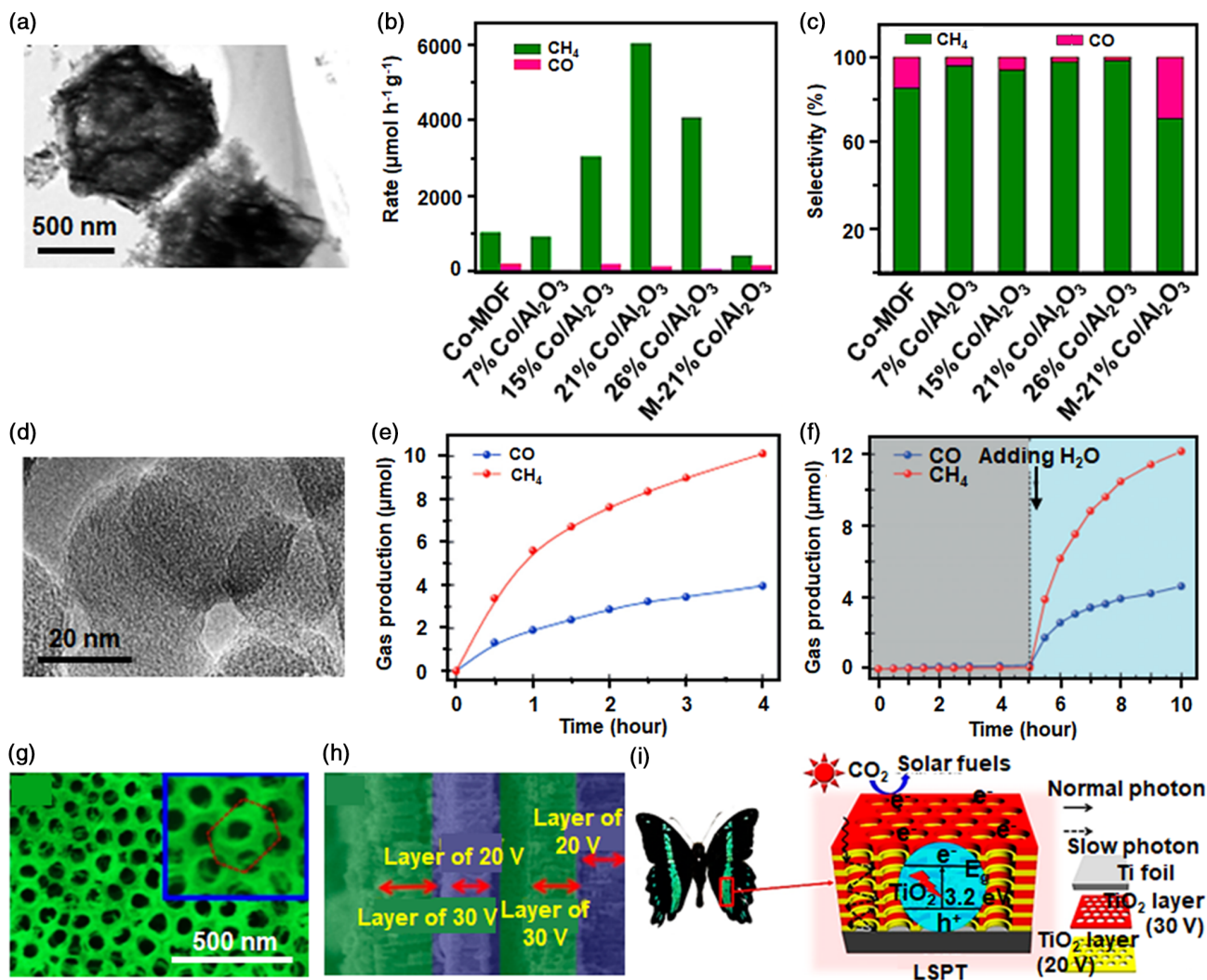
**ADVANCED
SCIENCE NEWS**

www.advancedsciencenews.com

**ADVANCED
ENERGY & SUSTAINABILITY
RESEARCH**
Open Access

www.advenergysustres.com

Figure 23. a) TEM, b) product rate, and c) selectivity over Co/Al$_2$O$_3$ catalyst in photothermal catalytic CO$_2$ conversion (green bars, CH$_4$; pink bars, CO). Reproduced with permission.[206] Copyright 2020, American Chemical Society. d) HRTEM images of the elemental B particles. e) Gas production of CO and CH$_4$ over elemental B particles under full arc irradiation. f) The impact of adding H$_2$O on the gas production of CO and CH$_4$ over elemental B particles in the photothermocatalytic CO$_2$ hydrogenation system. Reproduced with permission.[207] Copyright 2017, Wiley-VCH GmbH. g) Top-view and h) cross-sectional view SEM images of TiO$_2$ PCs. i) Schematic mechanism of TiO$_2$ PCs for the improved photothermocatalytic CO$_2$ hydrogenation performance. Reproduced with permission.[208] Copyright 2018, American Chemical Society.

thus facilitating the CO$_2$ conversion into CH$_4$ product. Furthermore, the Al$_2$O$_3$ support with high surface area and porosity also played an essential role in improving the CH$_4$ production yield, selectivity, and stability. Except for metallic catalysts, other materials like boron, TiO$_2$, and their heterojunctions have also been investigated in photothermocatalytic process. For example, Ye's group reported a fascinating approach to design the elemental B particles for the first time (Figure 23d),[207] which showed high light-response ability and efficient photo-thermo conversion. The photothermal effect of B particles could elevate the local temperature of the catalysts to activate CO$_2$ molecules. Meanwhile, the self-healing ability of the B element under light irradiation could decompose H$_2$ molecules and provide an active proton source as well as electrons for CO$_2$ reduction. In addition, the in situ formation of boron oxides contributed to the enhanced CO$_2$ absorption. In conclusion, elemental B catalyst exhibited a

CH$_4$ production rate of 2.5 μmol h^{-1} in the presence of water without any sacrificial agents or cocatalyst under UV−vis−IR light illumination (Figure 23e,f), which opened up a new era toward highly efficient CO$_2$ conversion and solar light utilization. Yu's group employed a facile strategy to design TiO$_2$ photonic crystals (TiO$_2$ PCs) through an anodization−calcination process (Figure 23g,h),[208] which possessed the satisfying heat radiation capture ability. With the specific PC morphology, the TiO$_2$ PC catalyst showed localized surface photothermo effect (Figure 23i), which not only improved light absorption but also increased the surface temperature to accelerate reaction kinetics and product yield rates, finally contributing to a high CO$_2$ methanation rate of 35.0 μmol g^{-1} h^{-1}, superior to that of commercial TiO$_2$ or TiO$_2$ nanotube arrays. Except for the aforementioned catalyst, some other materials such as Ru/i−Si−o,[209] Ni NPs/BaTiO$_3$,[210] Ni/Ce−Ti,[211] TiO$_2$ NPs/graphene,[212] and

**ADVANCED
SCIENCE NEWS**
www.advancedsciencenews.com

**ADVANCED
ENERGY & SUSTAINABILITY
RESEARCH**
Open Access
www.advenergysustres.com

TiO_{2-x}/CoO_x[213] have been recently reported for enhanced activity and selectivity for photothermocatalytic CO_2 methanation.

4.2.4. CO_2 to C_{2+} Hydrocarbons

The direct hydrogenation of CO_2 into hydrocarbons is a promising route to produce valuable CH_x chemicals. Fe-based catalysts have been regarded as ideal alternatives used in photothermocatalytic CO_2 hydrogenation to produce multicarbon hydrocarbons under solar light illumination at atmospheric conditions. Zhang's group proposed a Fe-500 catalyst composed of Fe and FeO_x nanoparticles on a $MgO-Al_2O_3$ support (**Figure 24**a–c),[214] which showed satisfying performance toward CO_2-to-C_{2+}

hydrocarbon conversion with high CO_2 conversion (50.1%) and C_{2+} selectivity (52.9%) when irradiated by UV−vis light (Figure 24d). Evidenced by the experimental results and DFT calculations, the construction of Fe/FeO_x heterojunctions suppressed the $-CH_2$ and $-CH_3$ hydrogenation to CH_4 on the active Fe^0 species. On the contrary, it facilitated the CO_2 hydrogenation into CO and the subsequent C−C coupling (Figure 24e), thereby improving the selectivity of C_{2+} hydrocarbons production. Meanwhile, the local surface temperature of Fe-500 could rapidly increase up to 252 °C under Xe lamp irradiation, which achieved almost the same activity as that in the thermocatalytic CO_2 conversion. Moreover, the light density is demonstrated to show negligible impact on CO_2 conversion or
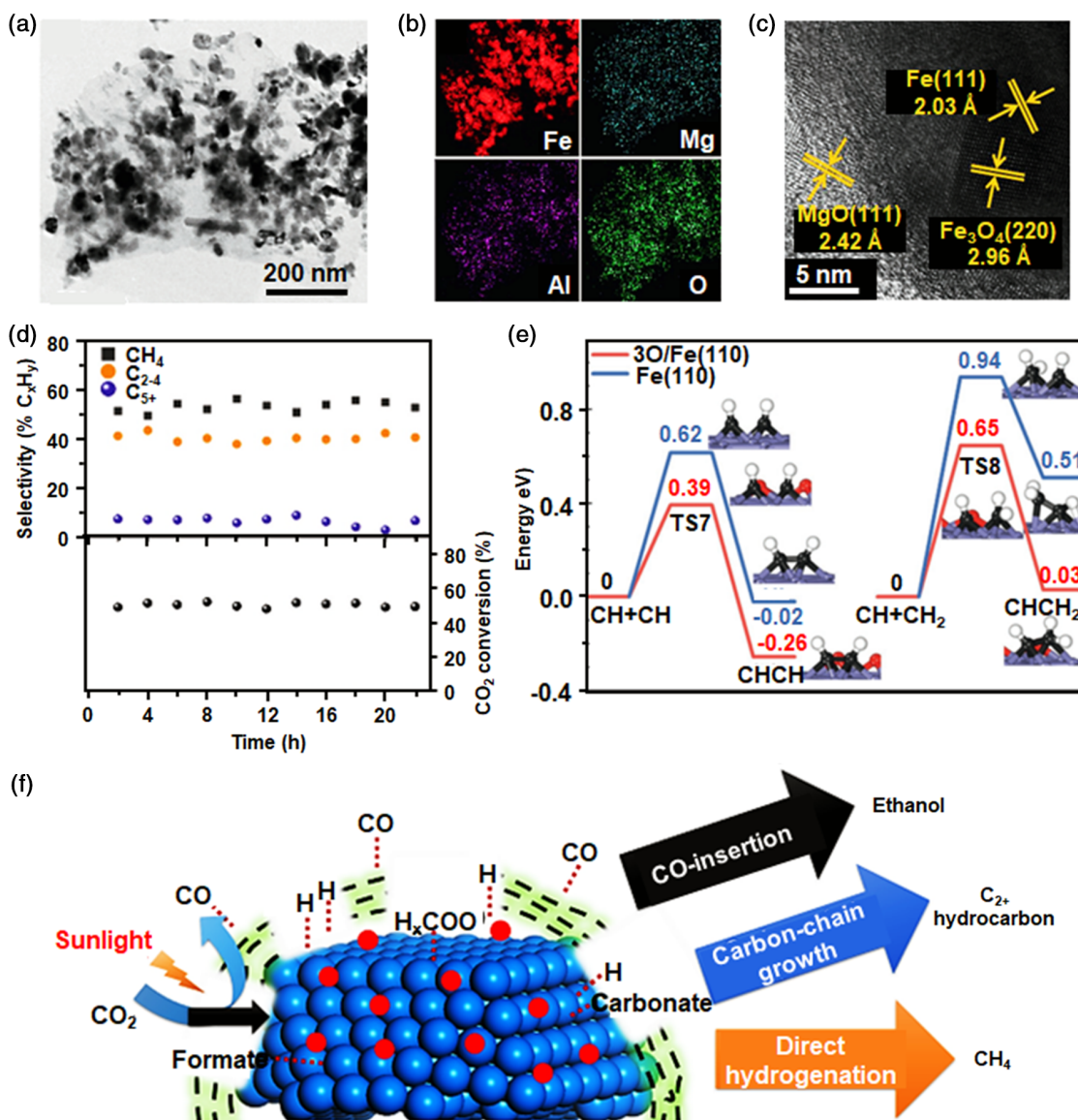

Figure 24. a) TEM image, b) the corresponding EDS elemental mapping of Fe, Mg, Al, and O, and c) HRTEM image of Fe-500 catalyst. d) Product selectivities (i.e., CH_4, C_{2-4}, and C_{5+}) and CO_2 conversion over Fe-500 catalyst under UV−vis illumination under a flow test. e) The energy profiles of the C−C coupling pathways on 3O/Fe(110) and Fe(110). The blue, black, red, and white spheres represent Fe, C, O, and H atoms, respectively. Reproduced with permission.[214] Copyright 2021, Wiley-VCH GmbH. f) Schematic illustration of the photothermocatalytic CO_2 hydrogenation to CH_4, C_{2+} hydrocarbons, and ethanol using Na-Co@C catalyst. Reproduced with permission.[217] Copyright 2018, Elsevier B.V.
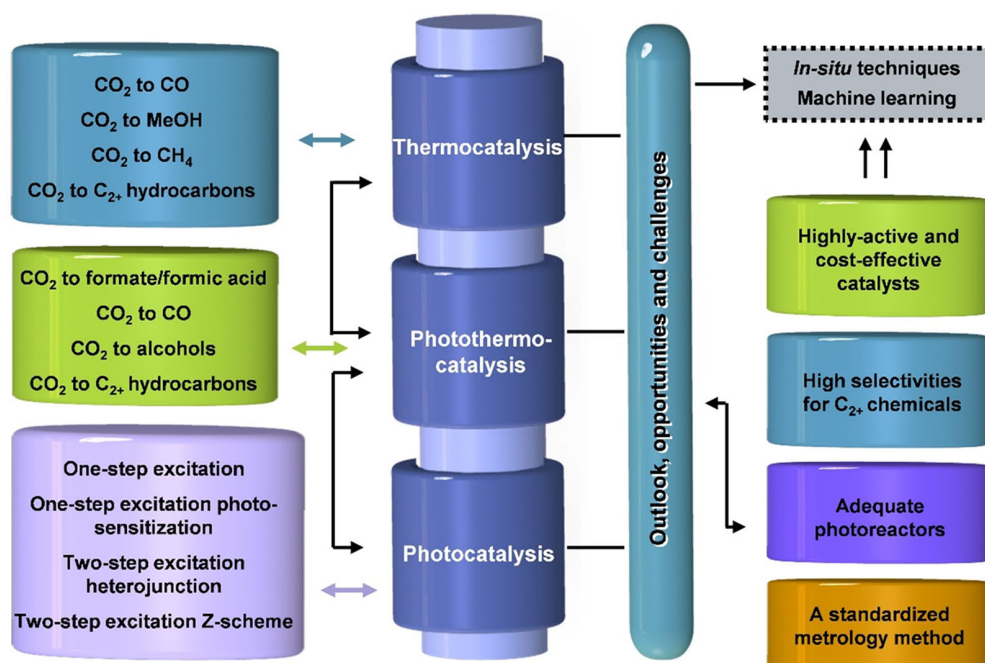
Figure 25. Summary of the plausible pathways, challenges, and prospects of the CO_2 conversion through thermocatalysis, photocatalysis, and photothermocatalysis.

C_{2+} selectivity, which indicated that the CO_2-to-C_{2+} conversion on Fe–500 catalyst followed a photothermocatalytic mechanism instead of photocatalysis. Other Fe-based catalysts (e.g., θ-Fe$_3$C[215] and Fe$_2$O$_3$/Fe$_3$O$_4$[216]) have also been investigated in photothermocatalytic CO_2 hydrogenation, which reached extraordinary selectivity for C_{2+} hydrocarbons formation. Furthermore, metallic Co, and Ni have also been employed in the CO_2 hydrogenation to generate C_{2+} hydrocarbons through the photothermocatalytic processes. For example, Na−Co@C[217] (Figure 24f) and Ni- or Co-doped BaZr$_{0.5}$Ce$_{0.3}$Y$_{0.2}$O$_{3−\delta}$[218] have been employed as efficient materials to enhance the surface temperature, photoexcited electron mobility, CO_2 dissociation, absorption ability of CO, C−C coupling, and the rapid desorption of reaction products onto the surface of catalysts, which synergistically contributed to the highly efficient photothermocatalytic CO_2 hydrogenation to C_{2+} hydrocarbons. These studies could guide the design of efficient catalysts for artificial photosynthesis via photothermocatalytic CO_2 hydrogenation, which can finally produce high-value-added multicarbon chemicals and fuels from CO_2.

5. Conclusion and Perspectives

The efficient utilization and chemical transformation of CO_2 into value-added chemicals and fuels have received increasing attention and been regarded as a promising approach to alleviate global warming, energy, and environmental crises. Notably, solar-driven photocatalysis has presented significantly enhanced activities and selectivities, which cater to the scientific and industrial communities and can be comparable with traditional thermocatalysis. This review primarily outlines the state of the art of

the technologies toward thermocatalytic, photocatalytic, and integrated photothermocatalytic CO_2 conversion into products of CO, CH_4, formate, methanol, ethanol, and C_{2+} hydrocarbons/oxygenates in the past 5 years (**Figure 25**). Special focuses have been paid to the designing strategies for effective heterogeneous catalysts for selective CO_2 conversion. Although the processes of thermocatalytic CO_2 hydrogenation into C1 chemicals (e.g., MeOH, CH_4) have been commercialized, the achievements in CO_2 chemical transformations are still not satisfactory concerning the technical and economic viability and energy efficiency for large-scale employment. Accordingly, extensive investigations have been conducted to develop UV and/or visible light-sensitive semiconductors for photocatalytic and photothermocatalytic CO_2 conversion. Particularly, plasmonic photocatalysis and plasmonic photothermocatalysis not only occupy an important position in practical CO_2-to-fuels conversion with a high utilization efficiency of solar energy but can also reference the selection of catalysts and reaction conditions from the conventional thermocatalysis, which builds a strong bridge between photocatalysis and conventional thermocatalysis. Moreover, the distinct pathways toward different products of these techniques have been comprehensively summarized to reveal the reaction mechanisms and key steps that determine the formation of the intermediates and final products, which can further serve as the guidance for the rational design of catalytic systems. Regardless of the aforementioned achievements, there is still plenty of room to improve the catalytic performance in the community of thermocatalysis and photo(thermo)catalysis.

More challenges should be overcome toward the following aspects. 1) It is highly demanded to develop highly active and cost-effective catalysts for large-scale synthesis, such as layer double hydroxides with tunable band structure and oxides/nitrides

**ADVANCED
SCIENCE NEWS**

www.advancedsciencenews.com

**ADVANCED
ENERGY & SUSTAINABILITY
RESEARCH**
Open Access

www.advenergysustres.com

with optimized geometric effect. 2) The yields and selectivities of C_{2+} hydrocarbons and oxygenates are more desired, although most of the existing catalytic systems produce C_1 chemicals (e.g., CO, formate, CH_4). The synthesis of C_{2+} hydrocarbons and oxygenates needs to overcome the thermodynamic limits and kinetic barriers during the multielectron transfer processes in CO_2RR, which will relieve excessive energy consumption and improve the energy conversion efficiency of the current CO_2 conversion techniques. Importantly, CO_2 adsorption, activation, and *CO intermediate formation significantly determine the yield of C_{2+} products. For example, the *CO dimerization affects the production rates of C_2H_4, ethanol, and n-C_3H_7OH. The *CH_2CHO intermediate generated from the *CO−CO dimerization is the rate-determining step for C_2H_4 and C_2H_5OH formation. Furthermore, n-C_3H_7OH can be produced by inserting CO into the stabilized *CH_3CHO intermediate. Therefore, the selectivities of targeted C_{2+} products have to be well controlled by the rational design of nanostructured catalysts. Intelligent strategies can be employed, such as morphology and structure optimization, alloying/dealloying, surface modification, and support introduction. Meanwhile, the structural integrity of catalysts and long-term durability of the overall catalytic systems still require to be improved for practical application as most durability tests have been conducted for a few hours and deactivation analyses are quite scarce. For example, thermal stability and recyclability of thermocatalysts have been tough problems to be resolved. Meanwhile, to suppress the photocorrosion and enhance the durability of (photo)thermocatalysts in the aqueous solution, coating the surface of the catalysts with protective layers through atomic layer deposition or electron beam evaporation methods may substantially improve the system stability for large-scale application. Accordingly, the structure of the catalysts, reaction conditions, and reactor configurations are required to be carefully designed for the improvement of the long-term catalytic system. 3) In terms of solar-driven photocatalysis, the intensity of the light source used in the lab (e.g., Xe lamp, Hg lamp) is much greater than sunlight. Moreover, the natural day/night cycle and narrow light absorption ability of most photo(thermo)catalysts not only bring challenges for industrial application but also reduce the utilization of solar energy. Accordingly, some ideal catalysts, such as rare-earth upconversion luminescent materials, photothermal semiconductors with a black color, or high density of defects/vacancies, can be designed to directly convert solar light to heat energy and applied in CO_2 hydrogenation, which not only elevates the photochemical contribution but also enhances the charge transfer efficiency and photoinduced carrier lifetimes, thus improving the catalytic activity. 4) Adequate photoreactors are required to effectively absorb and utilize sunlight for photo(thermo)catalysis, and therefore the continuous flow systems can be rationally designed to meet the requirements of industrial applications. 5) A standardized metrology method requires to be created to evaluate the solar-to-chemical conversion efficiency in photocatalytic and photothermocatalytic CO_2 reduction so that the comparison of the results from different research groups is convincing and fairly. Meanwhile, the intrinsic photocatalytic effect and photothermal effect should be identified. The key is to distinguish the thermal and nonthermal effects in photothermocatalysis, which can be measured by a precise instrument like nanoscale thermometers.

6) Computational analysis through DFT is of great significance to complement the experimental characterizations, which contributes to revealing the structure−activity relationship of the system and identifying the active sites, intermediate species, reaction pathways, and the roles of additives and water for CO_2RR.

Generally, as catalysts stand at the center to realize improved activity, selectivity, structure stability, and long-term durability, significant advances in designing effective heterogeneous catalysts are required for practical applications. The demonstrated strategies include structure optimization, crystal facets regulation, and defect engineering, thereby exposing increased density of active sites, high specific surface area, and closely conjoint interfaces to facilitate CO_2 adsorption and the subsequent transformations. Moreover, the reaction conditions and reactor design are always ignored, which need to be optimized to satisfy energy transfer (e.g., heat, light) and simplify equipment demand, aiming at constructing a well-established system for the enhancement of overall CO_2RR performance. Furthermore, in situ/ operando techniques (e.g., XRD, TEM, Extended X-ray absorption fine structure (EXAFS), fourier transform infrared spectroscopy (FTIR), Raman) and computational chemistry (e.g., theoretical calculations, molecular dynamics modeling) are required to be carried out, which can not only assess the precise nature of the active sites and identify the intermediate species to reveal the reaction pathways, but also determine the key parameters of designing efficient catalysts for highly efficient CO_2 conversion. Machine learning is the practice of building models from data, which has attracted intensive attention in catalysis, which has been integrated into the computational and experimental research in recent years. It can analyze the atomistic potentials and predict the catalytic properties of the catalytic systems. For example, DFT has been widely employed as an important tool for potential pathway screening, free energy calculations, the d-band center prediction, and molecular dynamics simulations, thus obtaining effective information about the relevant surface structures and compositions of catalysts under reaction conditions. Accordingly, machine learning provides increased value to advance the catalysis research, which not only helps researchers get more valuable information with existing data but also provides more sophisticated methods to collect new and useful data. Therefore, it can contribute to gain deep insights into the synthetic parameters for efficient catalysts designing and optimal reaction conditions in thermocatalysis, photocatalysis, and photothermocatalysis. In conclusion, comprehensive measures of precise catalyst preparation, in-depth structural characterization, thorough CO_2RR testing, and advanced computational study are indispensable to explore the full potentials of the technologies of thermo-, photo-, and photothermocatalytic CO_2 conversion.

Acknowledgements

Conflict of Interest

The authors declare no conflict of interest.

Keywords

[1] J. Artz, T. E. Müller, K. Thenert, J. Kleinekorte, R. Meys, A. Sternberg, A. Bardow, W. Leitner, *Chem. Rev.* **2017**, *118*, 434.

[2] a) S. De, A. Dokania, A. Ramirez, J. Gascon, *ACS Catal.* **2020**, *10*, 14147; b) N. N. Vu, S. Kaliaguine, T. O. Do, *Adv. Funct. Mater.* **2019**, *29*, 1901825.

[3] D. Mateo, J. L. Cerrillo, S. Durini, J. Gascon, *Chem. Soc. Rev.* **2021**, *50*, 2173.

[4] M. D. Porosoff, B. Yan, J. G. Chen, *Energy Environ. Sci.* **2016**, *9*, 62.

[5] A. Chen, M. Q. Yang, S. Wang, Q. Qian, *Front. Nanotechnol.* **2021**, *3*, 723120.

[6] a) U. Aslam, V. G. Rao, S. Chavez, S. Linic, *Nat. Catal.* **2018**, *1*, 656; b) V. Nair, M. J. Muñoz-Batista, M. Fernández-García, R. Luque, J. C. Colmenares, *ChemSusChem* **2019**, *12*, 2098.

[7] S. Luo, X. Ren, H. Lin, H. Song, J. Ye, *Chem. Sci.* **2021**, *12*, 5701.

[8] S. Wang, A. A. Tountas, W. Pan, J. Zhao, L. He, W. Sun, D. Yang, G. A. Ozin, *Small* **2021**, 2007025.

[9] Z. j. Wang, H. Song, H. Liu, J. Ye, *Angew. Chem., Int. Ed.* **2020**, *59*, 8016.

[10] W. Wang, S. Wang, X. Ma, J. Gong, *Chem. Soc. Rev.* **2011**, *40*, 3703.

[11] M. Konsolakis, M. Lykaki, S. Stefa, S. A. C. Carabineiro, G. Varvoutis, E. Papista, G. E. Marnellos, *Nanomaterials* **2019**, *9*, 1739.

[12] C. Álvarez Galván, J. Schumann, M. Behrens, J. L. G. Fierro, R. Schlögl, E. Frei, *Appl. Catal. B: Environ.* **2016**, *195*, 104.

[13] Y. Zhuang, R. Currie, K. B. McAuley, D. S. A. Simakov, *Appl. Catal. A: Gen.* **2019**, *575*, 74.

[14] X. Zhang, X. Zhu, L. Lin, S. Yao, M. Zhang, X. Liu, X. Wang, Y.-W. Li, C. Shi, D. Ma, *ACS Catal.* **2016**, *7*, 912.

[15] E. L. Fornero, D. L. Chiavassa, A. L. Bonivardi, M. A. Baltanás, *J. CO2 Util.* **2017**, *22*, 289.

[16] H. Jing, Q. Li, J. Wang, D. Liu, K. Wu, *J. Phy. Chem. C* **2018**, *123*, 1235.

[17] N. Nityashree, C. A. H. Price, L. Pastor-Perez, G. V. Manohara, S. Garcia, M. M. Maroto-Valer, T. R. Reina, *Appl. Catal., B* **2020**, *261*, 118241.

[18] Y. Shen, Z. Xiao, J. Liu, Z. Wang, *ChemCatChem* **2019**, *11*, 5439.

[19] C. Liu, S. L. Nauert, M. A. Alsina, D. Wang, A. Grant, K. He, E. Weitz, M. Nolan, K. A. Gray, J. M. Notestein, *Appl. Catal. B: Environ.* **2019**, *255*, 117754.

[20] Y. Yu, R. Jin, J. Easa, W. Lu, M. Yang, X. Liu, Y. Xing, Z. Shi, *Chem. Commun.* **2019**, *55*, 4178.

[21] N. Ishito, K. Hara, K. Nakajima, A. Fukuoka, *J. Energy Chem.* **2016**, *25*, 306.

[22] S. Choi, B.-I. Sang, J. Hong, K. J. Yoon, J.-W. Son, J.-H. Lee, B.-K. Kim, H. Kim, *Sci. Rep.* **2017**, *7*, 41207.

[23] a) F. Wang, M. Wei, D. G. Evans, X. Duan, *J. Mater. Chem. A* **2016**, *4*, 5773; b) B. Anicic, P. Trop, D. Goricanec, *Energy* **2014**, *77*, 279.

[24] P. Chen, G. Zhao, X.-R. Shi, J. Zhu, J. Ding, Y. Lu, *iScience* **2019**, *17*, 315.

[25] Z. Ou, J. Ran, J. Niu, C. Qin, W. He, L. Yang, *Int. J. Hydrogen Energy* **2020**, *45*, 6328.

[26] K. Ahmad, S. Upadhyayula, *Int. J. Hydrogen Energy* **2020**, *45*, 1140.

[27] L. Wang, W. Zhang, X. Zheng, Y. Chen, W. Wu, J. Qiu, X. Zhao, X. Zhao, Y. Dai, J. Zeng, *Nat. Energy* **2017**, *2*, 869.

[28] Y. Chen, H. Li, W. Zhao, W. Zhang, J. Li, W. Li, X. Zheng, W. Yan, W. Zhang, J. Zhu, R. Si, J. Zeng, *Nat. Commun.* **2019**, *10*, 1885.

[29] H. Li, L. Wang, Y. Dai, Z. Pu, Z. Lao, Y. Chen, M. Wang, X. Zheng, J. Zhu, W. Zhang, R. Si, C. Ma, J. Zeng, *Nat. Nanotechnol.* **2018**, *13*, 411.

[30] M. Huš, V. D. B. C. Dasireddy, N. Strah Štefančič, B. Likozar, *Appl. Catal. B: Environ.* **2017**, *207*, 267.

[31] J. Kothandaraman, R. A. Dagle, V. L. Dagle, S. D. Davidson, E. D. Walter, S. D. Burton, D. W. Hoyt, D. J. Heldebrant, *Catal. Sci. Technol.* **2018**, *8*, 5098.

[32] V. D. B. C. Dasireddy, N. S. Štefančič, M. Huš, B. Likozar, *Fuel* **2018**, *233*, 103.

[33] S. Kattel, B. Yan, Y. Yang, J. G. Chen, P. Liu, *J. Am. Chem. Soc.* **2016**, *138*, 12440.

[34] V. Dybbert, S. M. Fehr, F. Klein, A. Schaadt, A. Hoffmann, E. Frei, E. Erdem, T. Ludwig, H. Hillebrecht, I. Korossing, *Angew. Chem., Int. Ed.* **2019**, *58*, 12935.

[35] F. Liao, X.-P. Wu, J. Zheng, M. M.-J. Li, A. Kroner, Z. Zeng, X. Hong, Y. Yuan, X.-Q. Gong, S. C. E. Tsang, *Green Chem.* **2017**, *19*, 270.

[36] J. Díez-Ramírez, J. A. Díaz, F. Dorado, P. Sánchez, *Fuel Pro. Tech.* **2018**, *173*, 173.

[37] M. U. Khan, L. Wang, Z. Liu, Z. Gao, S. Wang, H. Li, W. Zhang, M. Wang, Z. Wang, C. Ma, J. Zeng, *Angew. Chem., Int. Ed.* **2016**, *55*, 9548.

[38] W. Zhang, L. Wang, H. Liu, Y. Hao, H. Li, M. U. Khan, J. Zeng, *Nano Lett.* **2017**, *17*, 788.

[39] E. Baraj, S. Vagaský, T. Hlinčik, K. Ciahotný, V. Tekáč, *Chem. Papers* **2016**, *70*, 395.

[40] R. Mutschler, E. Moioli, W. Luo, N. Gallandat, A. Züttel, *J. Catal.* **2018**, *366*, 139.

[41] A. Vita, C. Italiano, L. Pino, P. Frontera, M. Ferraro, V. Antonucci, *Appl. Catal. B: Environ.* **2018**, *226*, 384.

[42] C. Fukuhara, A. Kamiyama, M. Itoh, N. Hirata, S. Ratchahat, M. Sudoh, R. Watanabe, *Chem. Eng. Sci.* **2020**, *219*, 115589.

[43] D. Rivero-Mendoza, J. Stanley, J. Scott, K.-F. Aguey-Zinsou, *Catalysts* **2016**, *6*, 170.

[44] E. Moioli, A. Züttel, *Sus. Energy Fuels* **2020**, *4*, 1396.

[45] H. Sun, Y. Zhang, S. Guan, J. Huang, C. Wu, *J. CO2 Util.* **2020**, *38*, 262.

[46] S. Navarro-Jaén, J. C. Navarro, L. F. Bobadilla, M. A. Centeno, O. H. Laguna, J. A. Odriozola, *Appl. Surf. Sci.* **2019**, *483*, 750.

[47] J. Cored, A. García-Ortiz, S. Iborra, M. J. Climent, L. Liu, C.-H. Chuang, T.-S. Chan, C. Escudero, P. Concepción, A. Corma, *J. Am. Chem. Soc.* **2019**, *141*, 19304.

[48] L. Falbo, M. Martinelli, C. G. Visconti, L. Lietti, C. Bassano, P. Deiana, *Appl. Catal. B: Environ.* **2018**, *225*, 354.

[49] L. Luo, M. Wang, Y. Cui, Z. Chen, J. Wu, Y. Cao, J. Luo, Y. Dai, W.-X. Li, J. Bao, J. Zeng, *Angew. Chem., Int. Ed.* **2020**, *59*, 14434.

[50] R. E. Owen, D. Mattia, P. Plucinski, M. D. Jones, *ChemPhysChem* **2017**, *18*, 3211.

[51] C. G. Visconti, M. Martinelli, L. Falbo, L. Fratalocchi, L. Lietti, *Catal. Today* **2016**, *277*, 161.

[52] M. Albrecht, U. Rodemerck, M. Schneider, M. Bröring, D. Baabe, E. V. Kondratenko, *Appl. Catal. B: Environ.* **2017**, *204*, 119.

[53] B. Liang, H. Duan, T. Sun, J. Ma, X. Liu, J. Xu, X. Su, Y. Huang, T. Zhang, *ACS Sus. Chem. Eng.* **2018**, *7*, 925.

[54] J. Wei, J. Sun, Z. Wen, C. Fang, Q. Ge, H. Xu, *Catal. Sci. Technol.* **2016**, *6*, 4786.

**ADVANCED
SCIENCE NEWS**

www.advancedsciencenews.com

**ADVANCED
ENERGY & SUSTAINABILITY
RESEARCH**
Open Access

www.advenergysustres.com

[55] A. Ramirez, L. Gevers, A. Bavykina, S. Ould-Chikh, J. Gascon, *ACS Catal.* **2018**, *8*, 9174.

[56] a) M. Amoyal, R. Vidruk-Nehemya, M. V. Landau, M. Herskowitz, *J. Catal.* **2017**, *348*, 29; b) O. Elishav, Y. Shener, V. Beilin, M. V. Landau, M. Herskowitz, G. E. Shter, G. S. Grader, *ACS Appl. Mater. Interfaces* **2020**, *12*, 24855.

[57] a) A. Ramirez, A. Dutta Chowdhury, A. Dokania, P. Cnudde, M. Caglayan, I. Yarulina, E. Abou-Hamad, L. Gevers, S. Ould-Chikh, K. De Wispelaere, V. van Speybroeck, J. Gascon, *ACS Catal.* **2019**, *9*, 6320; b) A. Ramirez, S. Ould-Chikh, L. Gevers, A. D. Chowdhury, E. Abou-Hamad, A. Aguilar-Tapia, J. L. Hazemann, N. Wehbe, A. J. Al Abdulghani, S. M. Kozlov, L. Cavallo, J. Gascon, *ChemCatChem* **2019**, *11*, 2879.

[58] S.-M. Hwang, S. J. Han, J. E. Min, H.-G. Park, K.-W. Jun, S. K. Kim, *J. CO2 Util.* **2019**, *34*, 522.

[59] S. Bai, Q. Shao, P. Wang, Q. Dai, X. Wang, X. Huang, *J. Am. Chem. Soc.* **2017**, *139*, 6827.

[60] D. Xu, M. Ding, X. Hong, G. Liu, S. C. E. Tsang, *ACS Catal.* **2020**, *10*, 5250.

[61] a) J. Jiang, C. Wen, Z. Tian, Y. Wang, Y. Zhai, L. Chen, Y. Li, Q. Liu, C. Wang, L. Ma, *Ind. Eng. Chem. Res.* **2020**, *59*, 2155; b) T. Numpilai, T. Witoon, N. Chanlek, W. Limphirat, G. Bonura, M. Chareonpanich, J. Limtrakul, *Appl. Catal. A: Gen.* **2017**, *547*, 219.

[62] X. Wang, D. Wu, J. Zhang, X. Gao, Q. Ma, S. Fan, T.-S. Zhao, *Appl. Catal. A: Gen.* **2019**, *573*, 32.

[63] Z. Shi, H. Yang, P. Gao, X. Li, L. Zhong, H. Wang, H. Liu, W. Wei, Y. Sun, *Catal. Today* **2018**, *311*, 65.

[64] J. Wei, Q. Ge, R. Yao, Z. Wen, C. Fang, L. Guo, H. Xu, J. Sun, *Nat. Commun.* **2017**, *8*, 15174.

[65] S. Wang, T. Wu, J. Lin, Y. Ji, Y. Yan, Y. Pei, S. Xie, B. Zong, M. Qiao, *ACS Catal.* **2020**, *10*, 6389.

[66] a) S.-M. Hwang, C. Zhang, S. J. Han, H.-G. Park, Y. T. Kim, S. Yang, K.-W. Jun, S. K. Kim, *J. CO2 Util.* **2020**, *37*, 65; b) C. Dai, A. Zhang, M. Liu, J. Li, F. Song, C. Song, X. Guo, *RSC Adv.* **2016**, *6*, 10831.

[67] I. M. Dahl, S. Kolboe, *J. Catal.* **1996**, *161*, 304.

[68] Z. Li, J. Wang, Y. Qu, H. Liu, C. Tang, S. Miao, Z. Feng, H. An, C. Li, *ACS Catal.* **2017**, *7*, 8544.

[69] J. Chen, X. Wang, D. Wu, J. Zhang, Q. Ma, X. Gao, X. Lai, H. Xia, S. Fan, T.-S. Zhao, *Fuel* **2019**, *239*, 44.

[70] J. Gao, C. Jia, B. Liu, *Catal. Sci. Tech.* **2017**, *7*, 5602.

[71] L. Tan, P. Zhang, Y. Cui, Y. Suzuki, H. Li, L. Guo, G. Yang, N. Tsubaki, *Fuel Proc. Technol.* **2019**, *12*, 18.

[72] X. Liu, M. Wang, C. Zhou, W. Zhou, K. Cheng, J. Kang, Q. Zhang, W. Deng, Y. Wang, *Chem. Commun.* **2018**, *54*, 140.

[73] J. Li, T. Yu, D. Miao, X. Pan, X. Bao, *Catal. Commun.* **2019**, *129*, 105711.

[74] M. Bjorgen, S. Svelle, F. Joensen, J. Nerlov, S. Kolboe, F. Bonino, L. Palumbo, S. Bordiga, U. Olsbye, *J. Catal.* **2007**, *249*, 195.

[75] C. Zhou, J. Shi, W. Zhou, K. Cheng, Q. Zhang, J. Kang, Y. Wang, *ACS Catal.* **2019**, *10*, 302.

[76] J. Zhang, M. Zhang, S. Chen, X. Wang, Z. Zhou, Y. Wu, T. Zhang, G. Yang, Y. Han, Y. Tan, *Chem. Commun.* **2019**, *55*, 973.

[77] S. Sorcar, Y. Hwang, J. Lee, H. Kim, K. M. Grimes, C. A. Grimes, J. W. Jung, C. H. Cho, T. Majima, M. R. Hoffmann, S. I. In, *Energy Environ. Sci.* **2019**, *12*, 2685.

[78] J. Wu, H. Lu, X. Zhang, F. Raziq, Y. Qu, L. Jing, *Chem. Commun.* **2016**, *52*, 5027.

[79] M. Akatsuka, Y. Kawaguchi, R. Itoh, A. Ozawa, M. Yamamoto, T. Tanabe, T. Yoshida, *Appl. Catal. B: Environ.* **2020**, *262*, 118247.

[80] J.-T. Ren, Y.-L. Zheng, K. Yuan, L. Zhou, K. Wu, Y.-W. Zhang, *Nanoscale* **2020**, *12*, 755.

[81] N. Sharma, T. Das, S. Kumar, R. Bhosale, M. Kabir, S. Ogale, *ACS Appl. Energy Mater.* **2019**, *2*, 5677.

[82] J. Di, C. Zhu, M. Ji, M. Duan, R. Long, C. Yan, K. Gu, J. Xiong, Y. She, J. Xia, H. Li, Z. Liu, *Angew. Chem., Int. Ed.* **2018**, *57*, 14847.

[83] Z. Wang, M. Jiang, J. Qin, H. Zhou, Z. Ding, *Phys. Chem. Chem. Phys.* **2015**, *17*, 16040.

[84] Y. Xu, J. Mo, Q. Liu, X. Wang, S. Ding, *Catal. Sci. Technol.* **2020**, *10*, 2040.

[85] a) K. Wang, L. Zhang, Y. Su, D. Shao, S. Zeng, W. Wang, *J. Mater. Chem. A* **2018**, *6*, 8366; b) S. F. Ng, M. Y. L. Lau, W. J. Ong, *Solar RRL* **2021**, *5*, 2000535; c) X. Bian, S. Zhang, Y. Zhao, R. Shi, T. Zhang, *InfoMat* **2021**, *3*, 719.

[86] a) Y. Kuang, J. Shang, T. Zhu, *ACS Appl. Mater. Interfaces* **2019**, *12*, 3580; b) W. J. Ong, L. K. Putri, A. R. Mohamed, *Chem. Eur. J.* **2020**, *26*, 9710.

[87] Y. Zhu, Z. Xu, W. Jiang, S. Zhong, L. Zhao, S. Bai, *J. Mater. Chem. A* **2017**, *5*, 2619.

[88] S. Cao, Y. Li, B. Zhu, M. Jaroniec, J. Yu, *J. Catal.* **2017**, *349*, 208.

[89] C. Han, B. Wang, N. Wu, S. Shen, Y. Wang, *Appl. Surf. Sci.* **2020**, *515*, 145952.

[90] H. Wang, L. Zhang, Y. Zhou, S. Qiao, X. Liu, W. Wang, *Appl. Catal. B: Environ.* **2020**, *263*, 118331.

[91] A. Hammad, A. Anzai, X. Zhu, A. Yamamoto, D. Ootsuki, T. Yoshida, A. El-Shazly, M. Elkady, H. Yoshida, *Catal. Lett.* **2019**, *150*, 1081.

[92] F. Li, H. Zhou, J. Fan, Q. Xiang, *J. Coll. Inter. Sci.* **2020**, *570*, 11.

[93] J. Li, P. Yan, K. Li, J. You, H. Wang, W. Cui, Y. Cen, Y. Chu, F. Dong, *J. Mater. Chem. A* **2019**, *7*, 17014.

[94] X. Lin, S. Wang, W. Tu, H. Wang, Y. Hou, W. Dai, R. Xu, *ACS Appl. Energy Mater.* **2019**, *2*, 7670.

[95] D. Li, S. Ouyang, H. Xu, D. Lu, M. Zhao, X. Zhang, J. Ye, *Chem. Commun.* **2016**, *52*, 5989.

[96] B. Fang, Y. Xing, A. Bonakdarpour, S. Zhang, D. P. Wilkinson, *ACS Sustainable Chem. Eng.* **2015**, *3*, 2381.

[97] X. Zhang, Z. Yuan, J. Chen, G. Yang, D. D. Dionysiou, B. Huang, Z. Jiang, *Catal. Today* **2020**, *340*, 204.

[98] M. Ye, X. Wang, E. Liu, J. Ye, D. Wang, *ChemSusChem* **2018**, *11*, 1606.

[99] F. Xu, K. Meng, B. Zhu, H. Liu, J. Xu, J. Yu, *Adv. Funct. Mater.* **2019**, *29*, 1904256.

[100] Z. Wang, W. Zhou, X. Wang, X. Zhang, H. Chen, H. Hu, L. Liu, J. Ye, D. Wang, *Catalysts* **2020**, *10*, 654.

[101] L. Le-Quang, M. Stanbury, S. Chardon-Noblat, J.-M. Mouesca, V. Maurel, J. Chauvin, *Chem. Commun.* **2019**, *55*, 13598.

[102] P. He, S. Yang, W. Hu, S. Lee, J. Huang, *J. Phys. Chem. C* **2020**, *124*, 6215.

[103] S. Zhang, S. Wang, L. Guo, H. Chen, B. Tan, S. Jin, *J. Mater. Chem. C* **2020**, *8*, 192.

[104] L. Tan, S. M. Xu, Z. Wang, Y. Xu, X. Wang, X. Hao, S. Bai, C. Ning, Y. Wang, W. Zhang, Y. K. Jo, S. J. Hwang, X. Cao, X. Zheng, H. Yan, Y. Zhao, H. Duan, Y. F. Song, *Angew. Chem., Int. Ed.* **2019**, *58*, 11860.

[105] Y. Xu, J. Mo, Z.-C. Fu, S. Liu, Z. Yang, W.-F. Fu, *Chem. A Eur. J.* **2018**, *24*, 8596.

[106] Y. Kuramochi, O. Ishitani, *Front. Chem.* **2019**, *7*, 259.

[107] D.-I. Won, J.-S. Lee, Q. Ba, Y.-J. Cho, H.-Y. Cheong, S. Choi, C. H. Kim, H.-J. Son, C. Pac, S. O. Kang, *ACS Catal.* **2018**, *8*, 1018.

[108] Y. Yamazaki, T. Onoda, J. Ishikawa, S. Furukawa, C. Tanaka, T. Utsugi, T. Tsubomura, *Front. Chem.* **2019**, *7*, 288.

[109] B. Ma, G. Chen, C. Fave, L. Chen, R. Kuriki, K. Maeda, O. Ishitani, T. C. Lau, J. Bonin, M. Robert, *J. Am. Chem. Soc.* **2020**, *142*, 6188.

[110] B. Ma, M. Blanco, L. Calvillo, L. Chen, G. Chen, T. C. Lau, G. Drazic, J. Bonin, M. Robert, G. Granozzi, *J. Am. Chem. Soc.* **2021**, *143*, 8414.

[111] H. Rao, J. Bonin, M. Robert, *ChemSusChem* **2017**, *10*, 4447.

[112] Y. Wang, X.-W. Gao, J. Li, D. Chao, *Chem. Commun.* **2020**, *56*, 12170.

**ADVANCED
SCIENCE NEWS**

www.advancedsciencenews.com

**ADVANCED
ENERGY & SUSTAINABILITY
RESEARCH**
Open Access

www.advenergysustres.com

[113] Y. Chen, Y. Zhao, B. Yu, Y. Wu, X. Yu, S. Guo, B. Han, Z. Liu, *ACS Sustainable Chem. Eng.* **2020**, *8*, 9088.

[114] S. Li, K. Ji, M. Zhang, C. He, J. Wang, Z. Li, *Nanoscale* **2020**, *12*, 9533.

[115] D. Parobek, J. R. Meeder, J. Puthenpurayil, M. Nippe, D. H. Son, *J. Mater. Chem. A* **2020**, *8*, 12984.

[116] Q. X. Zhang, Y. Xia, S. Cao, *Chin. J. Catal.* **2021**, *42*, 1667.

[117] C. Cometto, R. Kuriki, L. Chen, K. Maeda, T.-C. Lau, O. Ishitani, M. Robert, *J. Am. Chem. Soc.* **2018**, *140*, 7437.

[118] Z. Chen, Y. Hu, J. Wang, Q. Shen, Y. Zhang, C. Ding, Y. Bai, G. Jiang, Z. Li, N. Gaponik, *Chem. Mater.* **2020**, *32*, 1517.

[119] L. Zhang, W. Wang, H. Wang, X. Ma, Z. Bian, *Chem. Eng. Sci.* **2019**, *207*, 1246.

[120] P. Li, X. Zhang, C. Hou, L. Lin, Y. Chen, T. He, *Phys. Chem. Chem. Phys.* **2018**, *20*, 16985.

[121] P. Li, X. Zhang, C. Hou, Y. Chen, T. He, *Appl. Catal. B: Environ.* **2018**, *238*, 656.

[122] K. Li, B. Peng, T. Peng, *ACS Catal.* **2016**, *6*, 7485.

[123] S. Chen, H. Gao, M. Han, X. Chen, X. Zhang, W. Dong, G. Wang, *ChemCatChem* **2020**, *12*, 3274.

[124] K. Wu, X. Dong, J. Zhu, P. Wu, C. Liu, Y. Wang, J. Wu, J. Hou, Z. Liu, X. Guo, *J. Mater. Sci.* **2018**, *53*, 11595.

[125] Z. Lou, P. Zhang, J. Li, X. Yang, B. Huang, B. Li, *Adv. Funct. Mater.* **2019**, *29*, 1808696.

[126] J. Lin, J. Hu, C. Qiu, H. Huang, L. Chen, Y. Xie, Z. Zhang, H. Lin, X. Wang, *Catal. Sci. Tech.* **2019**, *9*, 336.

[127] A. Raza, H. Shen, A. A. Haidry, M. K. Shahzad, L. Sun, *Appl. Surf. Sci.* **2020**, *529*, 147005.

[128] S. Kang, T. Im, M. Koh, C. S. Lee, *J. CO2 Util.* **2020**, *41*, 101230.

[129] W. J. Ong, K. P. Y. Shak, *Solar RRL* **2020**, *4*, 2000132.

[130] X. Zhu, H. Ji, J. Yi, J. Yang, X. She, P. Ding, L. Li, J. Deng, J. Qian, H. Xu, H. Li, *Ind. Eng. Chem. Res.* **2018**, *57*, 17394.

[131] M. Zhou, S. Wang, P. Yang, C. Huang, X. Wang, *ACS Catal.* **2018**, *8*, 4928.

[132] H. Liu, Z. Zhang, J. Meng, J. Zhang, *Mol. Catal.* **2017**, *430*, 9.

[133] H. Guo, J. Ding, S. Wan, Y. Wang, Q. Zhong, *Appl. Surf. Sci.* **2020**, *528*, 146943.

[134] Y. Xu, Y. You, H. Huang, Y. Guo, Y. Zhang, *J. Hazard Mater.* **2020**, *381*, 121159.

[135] M. Li, L. Zhang, X. Fan, M. Wu, M. Wang, R. Cheng, L. Zhang, H. Yao, J. Shi, *Appl. Catal. B: Environ.* **2017**, *201*, 629.

[136] Y. Wang, Y. Zeng, S. Wan, W. Cai, F. Song, S. Zhang, Q. Zhong, *ChemCatChem* **2018**, *10*, 4578.

[137] S. Tonda, S. Kumar, M. Bhardwaj, P. Yadav, S. Ogale, *ACS Appl. Mater. Interfaces* **2018**, *10*, 2667.

[138] M. Tahir, B. Tahir, *Ind. Eng. Chem. Res.* **2020**, *59*, 9841.

[139] a) X.-Y. Dao, X.-F. Guo, X.-Y. Zhang, Y.-S. Kang, W.-Y. Sun, *ACS Appl. Energy Mater.* **2020**, *3*, 3946; b) Y. Wang, W. Zhen, Y. Zeng, S. Wan, H. Guo, S. Zhang, Q. Zhong, *J. Mater. Chem. A* **2020**, *8*, 6034. c) X. Zhang, D. Xue, S. Jiang, H. Xia, Y. Yang, W. Yan, J. Hu, J. Zhang, *InfoMat* **2021**, https://doi.org/10.1002/inf212257.

[140] X. Yu, S. F. Ng, L. K. Putri, L. L. Tan, A. R. Mohamed, W. J. Ong, *Small* **2021**, 2006851 https://doi.org/10.1002/small.202006851.

[141] A. Ali, W.-C. Oh, *Sci. Rep.* **2017**, *7*, 1867.

[142] Y. Xia, B. Cheng, J. Fan, J. Yu, G. Liu, *Sci. China Mater.* **2020**, *63*, 552.

[143] Q. Mu, W. Zhu, X. Li, C. Zhang, Y. Su, Y. Lian, P. Qi, Z. Deng, D. Zhang, S. Wang, X. Zhu, Y. Peng, *Appl. Catal. B: Environ.* **2020**, *262*, 118144.

[144] J. Zhang, J. Fu, S. Chen, J. Lv, K. Dai, *J. Alloys Compd.* **2018**, *746*, 168.

[145] T. P. Yendrapati Taraka, A. Gautam, S. L. Jain, S. Bojja, U. Pal, *J. CO2 Util.* **2019**, *31*, 207.

[146] M. Iqbal, Y. Wang, H. Hu, M. He, A. H. Shah, P. Li, L. Lin, A. R. Woldu, T. He, *Electrochim. Acta* **2018**, *272*, 203.

[147] B. Su, L. Huang, Z. Xiong, Y. Yang, Y. Hou, Z. Ding, S. Wang, *J. Mater. Chem. A* **2019**, *7*, 26877.

[148] Y. Wang, Y. Zeng, S. Wan, S. Zhang, Q. Zhong, *J. CO2 Util.* **2019**, *29*, 156.

[149] S. Kumari, R. Gusain, A. Kumar, N. Manwar, S. L. Jain, O. P. Khatri, *J. CO2 Util.* **2020**, *42*, 101345.

[150] Z. Zeng, Y. Yan, J. Chen, P. Zan, Q. Tian, P. Chen, *Adv. Funct. Mater.* **2019**, *29*, 1806500.

[151] Z. Jiang, W. Wan, H. Li, S. Yuan, H. Zhao, P. K. Wong, *Adv. Mater.* **2018**, *30*, 1706108.

[152] Z.-F. Huang, J. Song, X. Wang, L. Pan, K. Li, X. Zhang, L. Wang, J.-J. Zou, *Nano Energy* **2017**, *40*, 308.

[153] H. Ma, X. Li, S. Fan, Z. Yin, G. Gan, M. Qin, P. Wang, Y. Li, L. Wang, *ACS Appl. Energy Mater.* **2020**, *3*, 5083.

[154] X. Li, X. Song, C. Ma, Y. Cheng, D. Shen, S. Zhang, W. Liu, P. Huo, H. Wang, *ACS Appl. Nano Mater.* **2020**, *3*, 1298.

[155] H. Qin, R.-T. Guo, X.-Y. Liu, W.-G. Pan, Z.-Y. Wang, X. Shi, J.-Y. Tang, C.-Y. Huang, *Dalton Trans.* **2018**, *47*, 15155.

[156] R.-t. Guo, X.-y. Liu, H. Qin, Z.-y. Wang, X. Shi, W.-g. Pan, Z.-g. Fu, J.-y. Tang, P.-y. Jia, Y.-f. Miao, J.-w. Gu, *Appl. Surf. Sci.* **2020**, *500*, 144059.

[157] T. Di, B. Zhu, B. Cheng, J. Yu, J. Xu, *J. Catal.* **2017**, *352*, 532.

[158] Y. Jia, H. Ma, W. Zhang, G. Zhu, W. Yang, N. Son, M. Kang, C. Liu, *Chem. Eng. J.* **2020**, *383*, 123172.

[159] N. T. Thanh Truc, T.-D. Pham, M. V. Nguyen, D. Van Thuan, D. Q. Trung, P. Thao, H. T. Trang, V. N. Nguyen, D. T. Tran, D. N. Minh, N. T. Hanh, H. M. Ngoc, *J. Alloys Compd.* **2020**, *842*, 155860.

[160] R. Bhosale, S. Jain, C. P. Vinod, S. Kumar, S. Ogale, *ACS Appl. Mater. Interfaces* **2019**, *11*, 6174.

[161] M. Lu, Q. Li, C. Zhang, X. Fan, L. Li, Y. Dong, G. Chen, H. Shi, *Carbon* **2020**, *160*, 342.

[162] N. T. Thanh Truc, N. T. Hanh, M. V. Nguyen, N. T. P. Le Chi, N. Van Noi, D. T. Tran, M. N. Ha, D. Q. Trung, T.-D. Pham, *Appl. Surf. Sci.* **2018**, *457*, 968.

[163] X. Fei, L. Zhang, J. Yu, B. Zhu, *Front. Nanotechnol.* **2021**, *3*, 698351.

[164] S. Mazzanti, S. Cao, K. ten Brummelhuis, A. Völkel, J. Khamrai, D. I. Sharapa, S. Youk, T. Heil, N. V. Tarakina, V. Strauss, I. Ghosh, B. König, M. Oschatz, M. Antonietti, A. Savateev, *Appl. Catal. B. Environ.* **2021**, *285*, 119773.

[165] G. Yang, D. Chen, H. Ding, J. Feng, J. Z. Zhang, Y. Zhu, S. Hamid, D. W. Bahnemann, *Appl. Catal. B: Environ.* **2017**, *219*, 611.

[166] L. Wang, B. Cheng, L. Zhang, J. Yu, *Small* **2021**, *17*, 2103447.

[167] Z. Wang, B. Cheng, L. Zhang, J. Yu, H. Tan, *Solar RRL* **2021**, 2100587.

[168] M. E. Aguirre, R. Zhou, A. J. Eugene, M. I. Guzman, M. A. Grela, *Appl. Catal. B: Environ.* **2017**, *217*, 485.

[169] T. Takayama, K. Sato, T. Fujimura, Y. Kojima, A. Iwase, A. Kudo, *Faraday Discuss.* **2017**, *198*, 397.

[170] Y. Wu, Y. Gong, J. Liu, T. Chen, Q. Liu, Y. Zhu, L. Niu, C. Li, X. Liu, C. Q. Sun, S. Xu, *J. Alloys Compd.* **2020**, *831*, 154723.

[171] C. Kim, K. M. Cho, A. Al-Saggaf, I. Gereige, H.-T. Jung, *ACS Catal.* **2018**, *8*, 4170.

[172] W. Shi, X. Guo, J.-C. Wang, Y. Li, L. Liu, Y. Hou, Y. Li, H. Lou, *J. Alloys Compd.* **2020**, *830*, 154683.

[173] M. Zubair, A. Razzaq, C. A. Grimes, S.-I. In, *J. CO2 Util.* **2017**, *20*, 301.

[174] X. Li, H. Jiang, C. Ma, Z. Zhu, X. Song, H. Wang, P. Huo, X. Li, *Appl. Catal. B: Environ.* **2021**, *283*, 119638.

[175] P. Madhusudan, R. Shi, S. Xiang, M. Jin, B. N. Chandrashekar, J. Wang, W. Wang, O. Peng, A. Amini, C. Cheng, *Appl. Catal. B: Environ.* **2021**, *282*, 119600.

**ADVANCED
SCIENCE NEWS**

www.advancedsciencenews.com

**ADVANCED
ENERGY & SUSTAINABILITY
RESEARCH**

www.advenergysustres.com

[176] M. Liang, T. Borjigin, Y. Zhang, H. Liu, B. Liu, H. Guo, *ACS Appl. Mater. Interfaces* **2018**, *10*, 34123.

[177] M. Tahir, *J. CO2 Util.* **2020**, *37*, 134.

[178] F. Zhang, Y.-H. Li, M.-Y. Qi, Z.-R. Tang, Y.-J. Xu, *Appl. Catal. B: Environ.* **2020**, *268*, 118380.

[179] W. Xiong, W. Dai, X. Hu, L. Yang, T. Wang, Y. Qin, X. Luo, J. Zou, *Mater. Lett.* **2018**, *232*, 36.

[180] Y. Jiang, J.-F. Liao, H.-Y. Chen, H.-H. Zhang, J.-Y. Li, X.-D. Wang, D.-B. Kuang, *Chem* **2020**, *6*, 766.

[181] J. Li, F. Wei, C. Dong, W. Mu, X. Han, *J. Mater. Chem. A* **2020**, *8*, 6524.

[182] W.-K. Jo, S. Kumar, S. Eslava, S. Tonda, *Appl. Catal. B: Environ.* **2018**, *239*, 586.

[183] L. Wang, Y. Dong, T. Yan, Z. Hu, A. A. Jelle, D. M. Meira, P. N. Duchesne, J. Y. Y. Loh, C. Qiu, E. E. Storey, Y. Xu, W. Sun, M. Ghoussoub, N. P. Kherani, A. S. Helmy, G. A. Ozin, *Nat. Commun.* **2020**, *11*, 2432.

[184] M. Cai, Z. Wu, Z. Li, L. Wang, W. Sun, A. A. Tountas, C. Li, S. Wang, K. Feng, A.-B. Xu, S. Tang, A. Tavasoli, M. Peng, W. Liu, A. S. Helmy, L. He, G. A. Ozin, X. Zhang, *Nat. Energy* **2021**, *6*, 807.

[185] H. Robatjazi, H. Zhao, D. F. Swearer, N. J. Hogan, L. Zhou, A. Alabastri, M. J. McClain, P. Nordlander, N. J. Halas, *Nat. Commun.* **2017**, *8*, 27.

[186] N. T. Nguyen, M. Xia, P. N. Duchesne, L. Wang, C. Mao, A. A. Jelle, T. Yan, P. Li, Z.-H. Lu, G. A. Ozin, *Nano Lett.* **2021**, *21*, 1311.

[187] N. T. Nguyen, T. Yan, L. Wang, J. Y. Y. Loh, P. N. Duchesne, C. Mao, P. C. Li, A. A. Jelle, M. Xia, M. Ghoussoub, N. P. Kherani, Z. H. Lu, G. A. Ozin, *Small* **2020**, *16*, 2005754.

[188] Y. Qi, L. Song, S. Ouyang, X. Liang, S. Ning, Q. Zhang, J. Ye, *Adv. Mater.* **2019**, *32*, 1903915.

[189] J. Guo, P. N. Duchesne, L. Wang, R. Song, M. Xia, U. Ulmer, W. Sun, Y. Dong, J. Y. Y. Loh, N. P. Kherani, J. Du, B. Zhu, W. Huang, S. Zhang, G. A. Ozin, *ACS Catal.* **2020**, *10*, 13668.

[190] Y. Li, A. G. Walsh, D. Li, D. Do, H. Ma, C. Wang, P. Zhang, X. Zhang, *Nanoscale* **2020**, *12*, 17245.

[191] C. Xu, W. Huang, Z. Li, B. Deng, Y. Zhang, M. Ni, K. Cen, *ACS Catal.* **2018**, *8*, 6582.

[192] J. Zhao, Q. Yang, R. Shi, G. I. N. Waterhouse, X. Zhang, L.-Z. Wu, C.-H. Tung, T. Zhang, *NPG Asia Mater.* **2020**, *12*, 1.

[193] J. Li, Y. Ye, L. Ye, F. Su, Z. Ma, J. Huang, H. Xie, D. E. Doronkin, A. Zimina, J.-D. Grunwaldt, Y. Zhou, *J. Mater. Chem. A* **2019**, *7*, 2821.

[194] J. Yan, C. Wang, H. Ma, Y. Li, Y. Liu, N. Suzuki, C. Terashima, A. Fujishima, X. Zhang, *Appl. Catal. B: Environ.* **2020**, *268*, 118401.

[195] X. Chen, Q. Li, J. Li, J. Chen, H. Jia, *Appl. Catal. B: Environ.* **2020**, *270*, 118915.

[196] S. Ning, H. Xu, Y. Qi, L. Song, Q. Zhang, S. Ouyang, J. Ye, *ACS Catal.* **2020**, *10*, 4726.

[197] Y.-F. Xu, P. N. Duchesne, L. Wang, A. Tavasoli, A. A. Jelle, M. Xia, J.-F. Liao, D.-B. Kuang, G. A. Ozin, *Nat. Commun.* **2020**, *11*, 5149.

[198] D. Mateo, P. Maity, G. Shterk, O. Mohammed, J. Gascon, *ChemSusChem* **2021**, https://doi.org/10.1002/cssc.202101950.

[199] D. Wu, K. Deng, B. Hu, Q. Lu, G. Liu, X. Hong, *ChemCatChem* **2019**, *11*, 1598.

[200] Y. Zheng, L. Zhang, J. Guan, S. Qian, Z. Zhang, C. K. Ngaw, S. Wan, S. Wang, J. Lin, Y. Wang, *ACS Sus. Chem. Eng.* **2021**, *9*, 1754.

[201] Z.-H. He, C.-S. Jiang, K. Wang, Z.-Y. Wang, N. Li, W.-T. Wang, Z.-T. Liu, *Catal. Today* **2020**, *356*, 579.

[202] L. Xu, M. N. Ha, Q. Guo, L. Wang, Y. Ren, N. Sha, Z. Zhao, *RSC Adv.* **2017**, *7*, 45949.

[203] P. Li, L. Liu, W. An, H. Wang, H. Guo, Y. Liang, W. Cui, *Appl. Catal. B: Environ.* **2020**, *266*, 118618.

[204] J. Ren, S. Ouyang, H. Xu, X. Meng, T. Wang, D. Wang, J. Ye, *Adv. Energy Mater.* **2017**, *7*, 1601657.

[205] Y. Li, J. Hao, H. Song, F. Zhang, X. Bai, X. Meng, H. Zhang, S. Wang, Y. Hu, J. Ye, *Nat. Commun.* **2019**, *10*, 2359.

[206] X. Chen, Q. Li, M. Zhang, J. Li, S. Cai, J. Chen, H. Jia, *ACS Appl. Mater. Interfaces* **2020**, *12*, 39304.

[207] G. Liu, X. Meng, H. Zhang, G. Zhao, H. Pang, T. Wang, P. Li, T. Kako, J. Ye, *Angew. Chem., Int. Ed.* **2017**, *56*, 5570.

[208] J. Low, L. Zhang, B. Zhu, Z. Liu, J. Yu, *ACS Sus. Chem. Eng.* **2018**, *6*, 15653.

[209] P. G. O'Brien, K. K. Ghuman, A. A. Jelle, A. Sandhel, T. E. Wood, J. Y. Y. Loh, J. Jia, D. Perovic, C. V. Singh, N. P. Kherani, C. A. Mims, G. A. Ozin, *Energy Environ. Sci.* **2018**, *11*, 3443.

[210] D. Mateo, N. Morlanes, P. Maity, G. Shterk, O. F. Mohammed, J. Gascon, *Adv. Funct. Mater.* **2020**, *31*, 2008244.

[211] E. T. Kho, S. Jantarang, Z. Zheng, J. Scott, R. Amal, *Engineering* **2017**, *3*, 393.

[212] M. Xu, X. Hu, S. Wang, J. Yu, D. Zhu, J. Wang, *J. Catal.* **2019**, *377*, 652.

[213] Y. Li, C. Wang, M. Song, D. Li, X. Zhang, Y. Liu, *Appl. Catal. B: Environ.* **2019**, *243*, 760.

[214] Z. Li, J. Liu, R. Shi, G. I. N. Waterhouse, X. D. Wen, T. Zhang, *Adv. Energy Mater.* **2021**, *11*, 2002783.

[215] C. Song, X. Liu, M. Xu, D. Masi, Y. Wang, Y. Deng, M. Zhang, X. Qin, K. Feng, J. Yan, J. Leng, Z. Wang, Y. Xu, B. Yan, S. Jin, D. Xiao, D. Ma, *ACS Catal.* **2020**, *10*, 10364.

[216] Z. Zhang, Z. Gao, H. Liu, S. Abanades, H. Lu, *ACS Appl. Energy Mater.* **2019**, *2*, 8376.

[217] L. Liu, A. V. Puga, J. Cored, P. Concepción, V. Pérez-Dieste, H. García, A. Corma, *Appl. Catal. B Environ.* **2018**, *235*, 186.

[218] J. Tian, Y. Ren, L. Liu, Q. Guo, N. Sha, Z. Zhao, *Mater. Res. Exp.* **2020**, *7*, 085504.
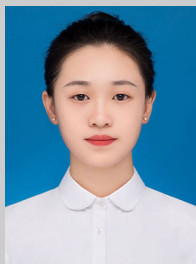
Wenjun Zhang received her Ph.D. under the supervision of Professor Zhong Jin in the School of Chemistry and Chemical Engineering, Nanjing University, P. R. China. Since 2020, she has been working in the College of Chemical Engineering, Nanjing Forestry University. Her main interest is the design and fabrication of nanocatalysts for electrochemical reduction of carbon dioxide and catalytic conversion of biomass.

Ding Ma is a professor at the College of Chemistry and Molecular Engineering, Peking University. He received his Ph.D. from the State Key Laboratory of Catalysis, Dalian Institute of Chemical Physics. His research interests are heterogeneous catalysis, especially that related to energy issues, including C1 chemistry (methane, CO_2, and syngas conversion), new reaction routes for sustainable chemistry, and efficient production and storage of H_2.

Javier Pérez-Ramírez is pursuing the design of heterogeneous catalysts and reactor concepts devoted to sustainable technologies. The latter secures the efficient utilization of natural resources, the transition to renewables, reduced energy consumption and waste, and minimized environmental impact. Topics of current interest include the valorization of carbon dioxide, natural gas, plastics, and renewables, plastics recycling, decentralized ammonia synthesis, the design of low-nuclearity catalysts, the analysis of pore quality in hierarchically organized materials, and the rational understanding of catalyst scale-up. He is also director of the National Centre of Competence in Research, NCCR Catalysis.

Zupeng Chen received his Ph.D. at Max Planck Institute of Colloids and Interfaces (Potsdam, Germany), in December 2015, under the supervision of Professor Markus Antonietti. He then joined the group of Professor Javier Pérez-Ramírez ETH Zurich as a postdoctoral fellow from 2016 to 2019. In 2020, he took up full professorship position in the College of Chemical Engineering, Nanjing Forestry University (China). His research activities embrace the design of efficient and stable heterogeneous catalysts and their applications in photo(electro)catalytic water splitting, CO_2 reduction, biomass valorization, and the industrial relevant transformations such as alkyne selective hydrogenations and Suzuki C–C couplings.